Development of Confocal Optical Holographic Microscopy

by

Robert A. McLeod
B.Sc., University of Victoria, 2001

A Thesis Submitted in Partial Fulfillment
of the Requirements for the Degree of

MASTERS OF APPLIED SCIENCE

in the Mechanical Engineering

Abstract

Optical Confocal Holography is a combination of two well known concepts: confocal microscopy and optical (laser) holography. Confocal microscopy places an aperture at a conjugate focus to the specimen focus. This filters any rays that are not on the focus plane, allowing a 3-dimensional image of the specimen to be built up over a set of planes. Holography is the measurement of both the amplitude and phase characteristics of light. Typically most methods only measure the amplitude of the image. The phenomenon of interference allows the determination of the phase shift for a coherent source as well. The phase information is directly related to the index of refraction of a material, which in turn is a function of the temperature and composition. As a technique, confocal holography holds promise to better characterize many physical processes in materials science, such as combustion and convection. It also may contribute to the biological sciences by imaging low-contrast, weak-phase objects. Thanks to the ongoing, continued improvement in computer processing speed, it has recently become practical to interpret data from confocal holography microscopy with a computer. The objective of the microscope is to non-invasively measure the three-dimensional, internal temperatures and compositions (e.g. solute/solvent gradient) of a specimen.

My contributions over the course of two years to the project were: generation and optimization of an optical design with a software package known as Zemax; sourcing and purchasing all components; formation of a CAD model of the microscope; experiments to characterize building vibrations and air currents; and the development of software in Visual Basic to simulate holograms and execute reconstruction algorithms for the specific application of confocal holography.

Supervisor: Associate Professor Rodney A. Herring, Mechanical Engineering

Table of Contents

List of Tables

List of Figures

List of Equations

Acknowledgments

First I would like to acknowledge my supervisor, Professor Rodney Herring. Rodney is the originator of the concept of confocal holography. Without his assistance and support this research would not have been possible.

I would like to thank Denis Laurin of the Hertzberg Institute of Astrophysics (now at the Canadian Space Agency). Denis provided valuable assistance for the optical design as well as some original lens designs. I would also like to thank my research compatriots, Peter Jacquemin and Songcan Lai for their valuable input to the project and discussions.

Funding to support this research was provided by the University of Victoria, NSERC, the Canadian Foundation for Innovation, and the British Columbia Knowledge Development Fund. Some equipment was provided on loan from the Canadian Space Agency.

1.0 Introduction to Holography

1.1 Background

The word holography comes from the Greek roots holos (whole) and graphe (writing). A holographic image is known as a hologram. Holography is an imaging method that collects all the information about an object: both the intensity and phase. It does this by exploiting the ability of wave-particles to interfere. With a coherent source interference phenomena will form well defined fringes from which the phase can be determined [Cathey, 1974 & Vest, 1979].

Holography was invented in 1948 by Dennis Gabor, a Hungarian-born physicist who was awarded the Nobel Prize in physics for his efforts in 1971 [Gabor, 1949 & 1951]. Gabor originally proposed the concept for electron microscopy but sources of sufficient coherence were not available at the time. It was not until the invention of the laser in the 1960s that holography became practical in the optical regime. In 1964, Leith and Upatnieks presented the first off-axis hologram of a toy brass locomotive at the Optical Society of America conference [Leith, 1964]. With the introduction of the off-axis technique it became possible to separate the virtual and conjugate images. Since then, holography has been performed with not just photons, but also electrons [Cowley, 1992], acoustical waves (phonons) [Bendon, 1975], and thermal neutrons [Sur, 2001]. Technically any coherence wave can be made to interfere.

There are a number of practical applications for holography outside of imaging. When holography is used as a metrology tool it is often termed *holographic interferometry* [Harihanan, 1992 &Vest, 1979]. The most common commercial use is the white-light "reflected-rainbow" holograms used as security features in currency as well as identity and credit cards [Saxby, 1998]. In the rainbow hologram the emulsion is located on top of a reflective metallic backing. Ambient light reflects off the backing and through the hologram which reconstructs the hologram so that it may be seen with the eye. This technique is considered difficult to replicate by counterfeiters.

Holographic memory storage is another application under development. Current optical storage technology such as the Digital Video Disk (DVD) is diffraction limited but holographic techniques can increase capacity by using the bulk volume rather than

surface for storage. Holographic mass data storage has been commercialized with the capacity for storing much more information than conventional magnetic disks (3.9 TByte) and higher access rates (1 Gbit/s) [Coufal, 1999 & Wikipedia - Holographic Versatile Disk (www), 2005].

Recently, the introduction of diode pumped solid state (DPSS) lasers has provided a new light source for holography applications [Huber, 1999]. The coherence length of diode pumped solid state lasers are typically an order of magnitude greater than standard gas lasers [Melles Griot, 1999] and power outputs can be two orders of magnitude greater than the largest HeNe lasers [Coherent (www), 2005]. Diode-pumped lasers are available in a wide selection of wavelengths from the near infrared to ultraviolet [Crystalaser (www), 2005].

1.2 Interference Phenomena

Interference is a phenomenon that can occur for any wave that obeys the *superposition principle.* Only the interference of light wavelets – photons – will be discussed in this paper. Maxwell's equations for free space that describe an optical wave are second-order homogenous linear partial differential equations [Hecht, 1998]:

$$\nabla^2 \mathbf{E} = \varepsilon_o \mu_0 \frac{\partial^2 \mathbf{E}}{\partial t^2}, \qquad \mathbf{1}$$

$$\nabla^2 \mathbf{B} = \varepsilon_o \mu_0 \frac{\partial^2 \mathbf{B}}{\partial t^2}. \qquad \mathbf{2}$$

The electric field **E** and magnetic field **B** at any point in space is the vector sum of any and all waves at that point. The difference in mathematics between the scalar sum and vector sum is the critical factor in the emergence of interference phenomenon. Hecht defines interference as:

> Optical interference corresponds to the interaction of two or more lightwaves yielding a resultant irradiance that deviates from the sum of the component irradiances.

In our case, we will only consider interference of only two waves. This is the simplest case and it is used in almost all holographic methods.

For the confocal laser holographic microscope a laser with a wavelength of 457.5 nm was chosen. This corresponds to an electric field oscillation frequency $6.56 \cdot 10^{14}$ Hz.

Directly measuring the variations in the electric field is impractical due to the very high rate of oscillation. Instead optical sensors such as charged coupled devices (CCDs) or our eyes measure the irradiance, **I**. The irradiance can be defined as the time average square of the electric field,

$$I = \varepsilon v \left\langle \mathbf{E} \bullet \mathbf{E} \right\rangle_T \qquad 3$$

with ε being the permittivity and υ is the frequency of oscillation [Hecht, 1998]. For the remainder of the analysis the constants ε and υ will be neglected because we are only concerned with the relative irradiance. This is valid if both disturbances are in the same medium. The time average is generally

$$\left\langle f(t) \right\rangle_T = \frac{1}{T} \int_t^{t+T} f(\tau) d\tau \,. \qquad 4$$

Note that *t*, *T*, and τ are dummy variables [Hecht, 1998]. Since interference is dependant on spatial position, this condition is satisfied.

For the case of a linearly polarized laser beam split into two parts we can define two optical waves,

$$\mathbf{E}_1(\mathbf{r}, t) = \mathbf{A}_1 \cos(\mathbf{k_1} \bullet \mathbf{r} - \omega t + \phi_1) \qquad 5$$

$$\mathbf{E}_2(\mathbf{r}, t) = \mathbf{A}_2 \cos(\mathbf{k}_2 \bullet \mathbf{r} - \omega t + \phi_2) \qquad 6$$

where **r** is position, *t* is time, **A** is the amplitude vector, **k** is the wavenumber, ω is the frequency, and ϕ is some additional phase shift varying from -π to π [Hecht, 1998]. The two waves must share the same frequency for temporal coherence to be satisfied. $\mathbf{E}_1$ is defined as the *object* or *specimen* wave and $\mathbf{E}_2$ is defined as the *reference* wave. In this case we can calculate the irradiance of the two waves by applying the dot product,

$$\mathbf{E} \bullet \mathbf{E} = \mathbf{E}_1^2 + \mathbf{E}_2^2 + 2\mathbf{E}_1 \bullet \mathbf{E}_2 \,. \qquad 7$$

The time average of both sides gives the result

$$I = I_1 + I_2 + I_{12} \qquad 8$$

[Hecht, 1998]. We can see that the superposition of the object and reference waves results in the addition of the term I_{12} which deviates from the scalar sum $I_1 + I_2$. I_{12} is the called the interference term. It results from the vector sum, where

$$I_{12} = 2\langle \mathbf{E}_1 \bullet \mathbf{E}_2 \rangle_T \qquad 9$$

[Hecht, 1998]. To evaluate the interference term, we need to compute the dot product of the two waves,

$$\mathbf{E}_1 \bullet \mathbf{E}_2 = \mathbf{A}_1 \bullet \mathbf{A}_2 \cos(\mathbf{k}_1 \bullet \mathbf{r} - \omega t + \phi_1) \times \cos(\mathbf{k}_2 \bullet \mathbf{r} - \omega t + \phi_2) \qquad 10$$

If the time integral $\langle \mathbf{E}_1 \bullet \mathbf{E}_2 \rangle_T$ is evaluated we find

$$\langle \mathbf{E}_1 \bullet \mathbf{E}_2 \rangle_T = \tfrac{1}{2} \mathbf{A}_1 \mathbf{A}_2 \cos(\mathbf{k}_1 \bullet \mathbf{r} + \phi_1 - \mathbf{k}_2 \bullet \mathbf{r} - \phi_2) \qquad 11$$

[Hecht, 1998]. This can be simplified by letting $\delta = \mathbf{k}_1 \bullet \mathbf{r} + \phi_1 - \mathbf{k}_2 \bullet \mathbf{r} - \phi_2$, where δ is the phase difference from the combination of difference between path length and the phase shift. The object phase shift ϕ_1 can be the phase shift resulting from the beam passing through a specimen. Notice that if $\mathbf{A}_1$ and $\mathbf{A}_2$ are perpendicular vectors, $I_{12} = 0$ and no interference will result. This implies that the polarization of the two waves must be the same, i.e. *p*-polarized and *s*-polarized light cannot interfere with each other. This is another requirement for interference, along with coherence.

The total irradiance can now be written as

$$I = \frac{A_1^2}{2} + \frac{A_2^2}{2} + A_1 A_2 \cos\delta \,. \qquad 12$$

Hence we can see that the irradiance will be at a maximum when $\delta = 0, \pm 2\pi, \pm 4\pi, \ldots$ [Hecht, 1998] This is known as *total constructive interference* and it occurs when two peaks or two valleys overlap. At the same time we can see that irradiance will be at a minimum when $\delta = \pm\pi, \pm 3\pi, \pm 5\pi, \ldots$ This is known as *total destructive interference* and it occurs when a peak and valley overlap. If δ varies linearly with space, the irradiance will follow a sinusoidal profile between the extrema.

For the special case where the amplitude of the object and reference beams are equal the irradiance can be simplified to

$$I = 2A(1 + \cos\delta) = 4A\cos^2 \delta/2 \,. \qquad 13$$

The minima is then $I_{\min} = 0$ and the maxima $I_{\max} = 4A$ [Hetcht, 1998]. Most holography methods will try to achieve this condition because it maximizes the contrast between the light and dark regions. This in turn maximizes the irradiance resolution of a detector.

A common convention is to describe the irradiance in complex vector form given by Euler's equation such that

$$\mathbf{I} = Ae^{j\phi} = A\left(\cos\phi + j\sin\phi\right). \qquad 14$$

I is called either the *complex irradiance* or sometimes the *complex amplitude*. A is known as the *amplitude*, *magnitude,* or *intensity* of the complex irradiance. ϕ is known as the *phase*.

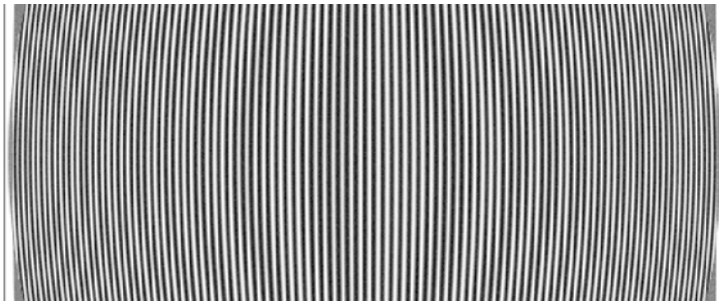

Figure 1: A simulated interference fringe pattern (hologram) with visible spherical curvature induced by lenses.

The sinusoidal periodic variation in irradiance between constructive and destructive interference zones produces an irradiance pattern known as *interference fringes* [Figure 1]. The peak-to-peak distance between two fringe maxima is equal to one wavelength of path difference between the interfering waves.

$$\Delta r = m\lambda \qquad 15$$

For two plane waves of wavelength λ, the angle of incidence of the two beams, θ, can be used to determine the spatial frequency of the fringes [Figure 2]. To find the carrier frequency f_c we must find the rate at which $R' - R = \lambda$.

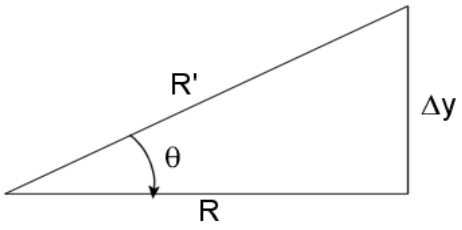

Figure 2: R' and R are plane waves converging at an angle θ.

Using basic trigonometry

$$R = \frac{\Delta y}{\sin\theta}; R' = \frac{\Delta y}{\tan\theta}. \quad 16$$

Therefore by substitution

$$\lambda = \Delta y\left(\frac{1}{\sin\theta} - \frac{1}{\tan\theta}\right). \quad 17$$

Through simplifying and noting that $f_c = 1/\Delta y$ then

$$f_c = \frac{1-\cos\theta}{\lambda\sin\theta}. \quad 18$$

The spatial frequency of the fringes is generally known as the *carrier frequency*. Since it is a constant for interfering plane waves, it is possible to filter it out.

1.2.1 Coherence Condition

In order to produce steady interference between two optical waves, they must be coherent in time and space. Ideally, the sources of the waves will be monochromatic point sources. Practically, all sources show some variation in frequency with respect to time. As a result, most interference methods split the wave from a single coherent source, such as a laser, and then later recombine them to create an interferogram (or hologram). There are two primarily modes for generating interference from a single coherent source: amplitude splitting and wavefront splitting. These two methods will be examined in detail later.

The coherence of a photon beam can be separated into temporal coherence (longitudinal) and spatial coherence (transversal) [Tonomura, 1993].

Temporal coherence is a measure of the monochromatic-ness of a source. The temporal coherence of a source is defined by its *coherence length*. The coherence length, l_c, is the length of an individual wavetrain emitted by a source that resembles a sinusoidal wave. A perfectly monochromatic source would have an infinite coherence length. Coherence length Δl_c can be calculated from the wavelength spread $\Delta\lambda$ of a source with average wavelength λ.

$$\Delta l_c = c\Delta t \sim \frac{c}{\Delta \nu} = \frac{\left(\overline{\lambda}\right)^2}{\Delta\lambda} \qquad 19$$

assuming that $\Delta\lambda << \lambda$ [Born, 1975]. It can alternatively be represented in terms of the time Δt a signal remains coherent or the frequency spread $\Delta\upsilon$. Coherence length is commonly measured with a Michelson-Morley interferometer. Effectively, the coherence length determines the maximum path length difference that may exist between the reference and object beams. A typical coherence length for a Helium-Neon gas laser is 0.3 m. Diode-pumped solid-state lasers are usually superior with coherence lengths on the order of 5 m. In comparison the coherence of an electron beam is typically on the order of a micrometer.

Spatial coherence is a measure of the effective size of a source. A perfect point source would exhibit complete spatial coherence. Spatial coherence can best be seen from Young's classic double slit experiment [Figure 3]. In this case, the width of the slits determines the spatial coherence of the source and hence the spatial extent of the fringe pattern.

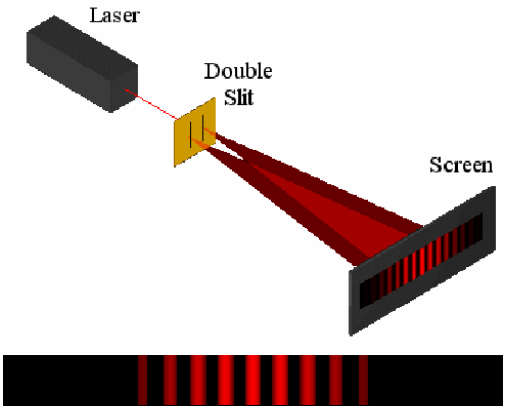

Figure 3: Young's double slit experiment demonstrating interference.

The spatial coherence of a laser beam can be determined from the far-field divergence. That is the actual angle of the beam with respect to a perfectly collimated beam. The divergence for a laser is on the order of one milliradian. Since lasers emit nearly-collimated, nearly-Gaussian waves spatial coherence is typically taken for granted. Diffraction plays a larger role in determining the width over which interference can occur.

Coherence may be quantified by measuring the maximum and minimum irradiance of a fringe pattern. Assuming that the two waves have equal intensity and are linearly polarized, the *fringe visibility* is a measure of the coherence of the two beams.

$$V = \frac{I_{\max} - I_{\min}}{I_{\max} + I_{\min}} \qquad 20$$

If the two beams have perfect coherence I_{min} is zero and the fringe visibility is unity. If they are totally incoherent, $I_{max} = I_{min}$, and the fringe visibility is zero [Hecht, 1998].

1.3 Optical versus Digital Reconstruction

There are two methods to record a hologram: either with an emulsion deposited on film or glass plate or digitally with a solid-state digital camera. This leads directly to two different methods of reconstructing the hologram to measure the intensity and phase information.

With optical reconstruction the interference pattern essentially creates a diffraction grating in the emulsion, i.e. a hologram. The hologram is reconstructed by illumination by plane waves on the diffraction grating that produces a main band and several sidebands of increasing order [Figure 4]. An aperture is introduced that admits one of the first order sidebands. The filtered sideband forms an image of the complex irradiance. The emulsion can be illuminated at different angles in order to build up a set of amplitude-phase images.

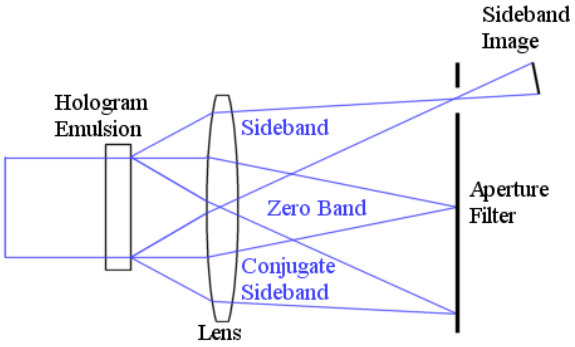

Figure 4: Optical hologram reconstruction with emulsion through illumination by a laser.

With digital reconstruction the hologram is stored in computer memory. A variety of algorithms have been developed to analyze holograms and extract the phase. The most common method is to take a Fourier transform of the hologram which transforms the data into frequency space. The phase information will be contained in one of the sidebands

produced by the Fourier transform. The sideband is typically window filtered and then shifted to the origin so that an inverse Fourier transform may be applied. The result is complex and reflects the original amplitude and phase of the signal that is embedded in the hologram. This method will be described in detail in section 4.3. Alternative algorithms have been developed that use iterative methods [Fujita, 2005] or the Fresnel-Kirchoff integral [Schnars, 2002].

Mathematically the two approaches are very similar with the exception that optically the system operates in continuous space while the digital system is discrete.

Historically the performance of emulsions was superior to that of electronic sensors. The film had superior spatial resolution and responsitivity. However, many of the advantages of film have eroded since the introduction of the Charged Coupled Device (CCD) camera. The ease of use for an electronic camera compared to film development along with the improved performance of CCD cameras has led to a significant shift towards digital reconstruction. The CCD has a quantum efficiency of capturing photons of approximately 70 % as compared to 2 % for film. The particular advantage of the solid-state sensor is its high linearity response to irradiance. Emulsions tend to be non-linear at the extremes of high and low irradiance.

Table 1: Comparison of Emulsion versus CCD Performance [Slavich OAO 2005, Eastman Kodak 2000]

Technology	Emulsion	CCD
Manufacturer	Slavich	Kodak
Model	VRP-M	LKI-8811
Spatial Resolution	40 nm grain size	7 μm
Dynamic Range	~100 dB	70 dB
Exposure Responsitivity	60-80 $\mu J/cm^2$	12 $V/\mu J/cm^2$

Response Linearity	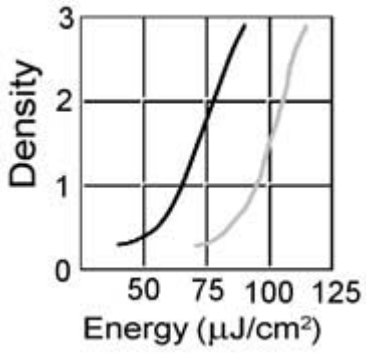	5 % pk-pk
Data Rate	-	120 MHz

Research on optical reconstruction has not stopped in spite of the superiority of the CCD camera in most areas. This is primarily due to the ability of optical reconstruction to be done in real-time. This has potential for applications in optical computing and data storage [Karim, 1992].

1.4 Wavefront versus Amplitude Splitting

There are two means of splitting a coherent source into an object and reference beam [Figure 5]. Wavefront splitting geometrically separates the beam by means of a Fresnel biprism. A Gaussian beam will be split into two D-shaped half-Gaussian wavefronts. Amplitude splitting is normally accomplished by means of a partially silvered mirror or diffracting crystal. Diffraction gratings can also perform amplitude splitting. Amplitude splitting affects only the irradiance of the beam profile and not the shape.

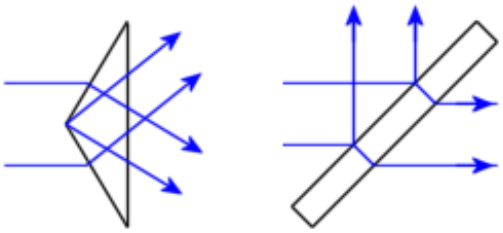

Figure 5: Fresnel biprism and plate beam splitter for wavefront and amplitude splitting respectively

With wavefront split holography the object and reference beam propagate side-by-side through the optical system. Because of this symmetry the wavefront distortion introduced by the optics will be equal for the two beams. Surface irregularities and the specimen will be the only source of phase shift between the two beams. As a result when

the beams are overlaid to interfere they are effectively plane waves. Two interfering plane waves will produce evenly spaced parallel fringes. Evenly spaced parallel fringes have a constant carrier frequency and are simple to filter and retrieve the pure phase measurement. The symmetric path length is also valuable for high-speed holography using pulsed lasers. In wavefront split holography the beams are offset from the optical axis (off-axis propagation). As a result all lenses in the system will generate coma aberration. This presents a special challenge in optimizing the spherical and coma aberration of the system.

Amplitude split holography preserves the shape of the beam profile at the expense of having the object and reference beams travel along separate optical paths. It tends to be simpler with fewer components. With wavefront split holography the outside edges of the D-shaped beams tend to suffer excessive coma aberration and are lost. Optical performance in amplitude split holography is superior because the coma is much reduced which allows the spherical aberration to be better optimized. Also the diameter of the beam can be much larger because there is no longer the need to fit both beams inside the clear aperture of the optics. On the negative side amplitude split systems are more sensitive to the vibration of optical components. Components on different parts of the table are likely to vibrate out of phase with each other exacerbating any vibration issues and destabilizing the fringe pattern.

In summary, wavefront split holography has the following advantages:

1. Object and reference beam have symmetric path length.
2. Easy implementation of off-axis filtered interference.
3. Less sensitive to vibration.

Amplitude split holography has the following advantages:

1. Gaussian beam profile maintained.
2. Beam diameter larger for given clear aperture.
3. No coma allows for improved optical performance.
4. Lower number of optical components.

2.0 Confocal Holography

2.1 Significance of Phase

The irradiance equation for light can be defined quite simply as a periodic waveform by

$$I = I_o e^{-i\phi} \qquad 21$$

where I_o is the intensity and ϕ is the phase. The majority of sensors are only capable of detecting intensity, because the variation in phase is such a high frequency measurement.

When light passes through a material other than a vacuum its velocity is reduced. The wavelength shrinks but the frequency of oscillation remains unchanged [Figure 6]. This reduction in velocity is quantified by *n* the *index of refraction* of a material denoted as,

$$n = \frac{c}{v}. \qquad 22$$

This variation in the speed of light in a material is quite important for physical phenomena such as Snell's Law of Refraction.

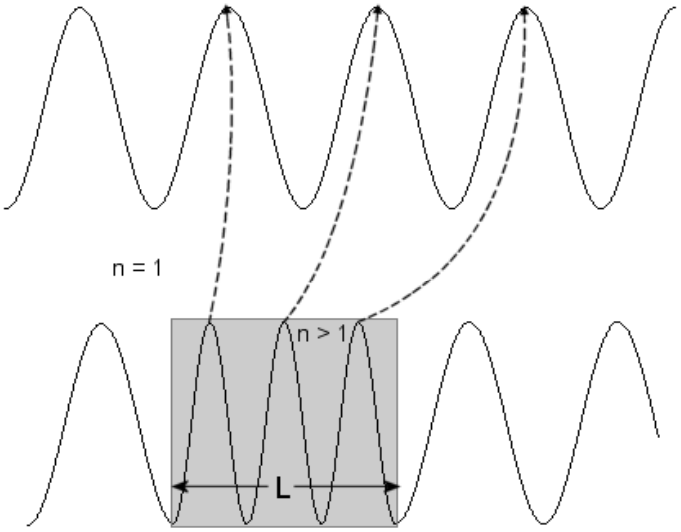

Figure 6: The effect of index of refraction on wavelength: the wavelength shift in the region of higher index of refraction (grey) retards the phase of bottom wave relative to top.

A shift in phase $\Delta\phi$ caused by a variation Δn in index of refraction is related to the distance the light travels through the material *L*,

$$\Delta\phi = L\Delta n\,. \qquad 23$$

The phase shift for an individual wavelet is determined by the variation of index of refraction integrated over its path. The key is that variation in the index of refraction is driven by variation in the local temperature and composition. The change in index of refraction can be decomposed into

$$\Delta n_{T+C} = \left(\frac{\partial n}{\partial T}\right)_C \Delta T + \left(\frac{\partial n}{\partial C}\right)_T \Delta C \qquad 24$$

where T is temperature and C composition [Abe, 1999]. An example of composition would be solute/solvent concentration.

If it is possible to determine the variation in index of refraction in three-dimensions then it is also possible to determine the temperature or composition in three-dimensions. This is accomplished with nothing more invasive than a laser beam. If both the temperature and composition are independent variables it is theoretically possible to solve the above equation simultaneously by sampling with two widely separated wavelengths [Abe, 1999]. Index of refraction is a function of wavelength, and the variation in index with respect to wavelength is known as the *dispersion* of a material.

2.2 Utility of a Convergent Beam

The majority of holography methods illuminate a specimen with a collimated (or integrated) beam. A collimated beam is one where all rays that define it are traveling parallel to each other. Confocal holography illuminates a specimen with a beam that converges to a focus by means of convex lenses. Confocal is defined as an optical arrangement of two identical lenses placed twice their focus length apart, back to back [Figure 7]. Ignoring any optical aberrations, a collimated beam that enters a confocal lens set will focus to an infinitesimal point half-way between the two lenses. Ideally the beam that emerges from the second lens will remain collimated. In practice spherical aberration will make the exiting beam not perfectly collimated.

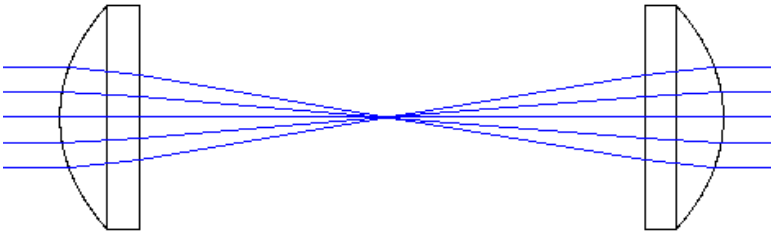

Figure 7: Ray trace of confocal plano-convex lenses.

With a convergent beam, the path length of the chief (centre) ray is shorter than that of the marginal (outer) rays. In a collimated beam, the path length of all rays across the beam is identical. This forms the basis of the ability of a convergent beam to localize an object along the optical axis through triangulation, i.e. provide three-dimensional imaging.

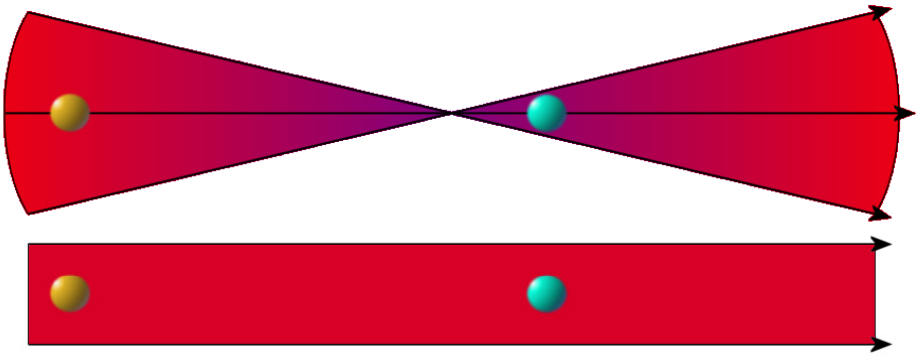

Figure 8: Comparison of convergent versus collimated beam shows how irradiance increases near focus for convergent beam so the blue object has more Influence on image than the old object

It can be seen from [Figure 8] that as the beam is rastered about the specimen the influence the specimen has on the beam changes in the convergent beam. For example, as the beam rasters along the optical axis from the gold specimen to the blue specimen there will be no change in the phase profile of the collimated beam whereas in the convergent beam, the phase profile will change significantly as more rays pass through the blue specimen the closer it approaches the focus position.

The basis for 3-dimensional phase is slightly different for that of traditional confocal intensity microscopy. Confocal microscopy places an aperture at a conjugate focus to the specimen focus. This filters any rays that are not on the focus plane, allowing a 3-dimensional image of the specimen to be built up over a set of planes. Phase is an

integrated measurement of the index of refraction along the ray path. In order to find the phase shift generated by a localized volume element (voxel) it is necessary to use triangulation. For 3-dimensional phase measurement, the aperture is not strictly required but it still acts as a stray-light filter to improve fringe resolution.

2.3 Confocal Holograph Example

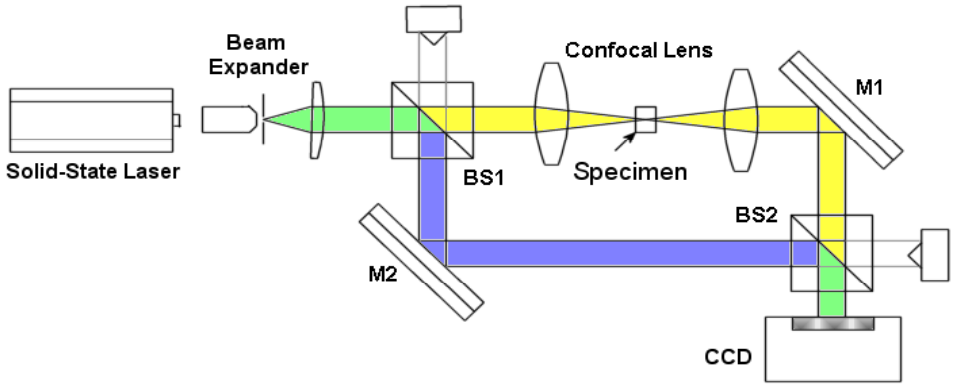

Figure 9: Schematic of Mach-Zehnder confocal holograph (yellow object beam, blue interference beam).

The simplest example of a confocal holograph is the Mach-Zehnder interferometer [Figure 9] with a pair of confocal lenses inserted into one of the beam paths. This system operates on the basis of amplitude splitting. The first beam splitter (BS1) separates the laser beam (green) into a reference (blue) and object (yellow) beam. The object beam is then focused onto a specimen, and then re-collimated by a pair of confocal lenses. A pair of mirrors (M1,M2) are used to reflect the beams onto the second beam splitter (BS2). BS2 will transmit some energy onto a beam trap and the remainder onto a detector such as a CCD camera. This system will generate a circular interference pattern on the detector [Figure 10].

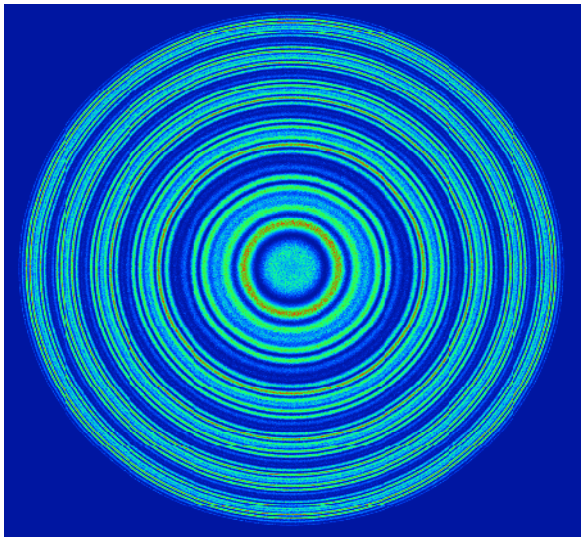

Figure 10: Simulated in-line hologram from Mach-Zehnder confocal holograph.

The Mach-Zehnder based confocal holograph is not ideal for a number of reasons.

1. The circular fringe pattern does not have a constant spatial frequency of the fringes and as a result it is not possible to separate the conjugate image from the virtual image. Methods where the interfering beams are incident along different axes (off-axis holography) can have a constant frequency fringe pattern and the conjugate frequency is well separated in Fourier space.
2. Rastering must be accomplished by moving the sample, potentially disturbing it. It is desirable to scan the beam through the specimen instead.
3. The full width of the CCD sensor is not utilized. A projector lens should be introduced.
4. The system tends to be extremely sensitive to vibrations in the mirrors. This is especially so if the mirrors are vibrating out of phase as this will shift the path length of the reference beam relative to the object beam.

An appropriate microscope design would resolve these difficulties and optimize the various parameters in confocal holography.

2.4 Confocal Holography Prior Art

Any attempt at a literature search for prior art in the field of confocal holography is complicated by the fact that the method presented in this chapter is novel but there is no president for it to have exclusive use of the keywords. A search with the keywords *confocal* and *holography*, as well as varies combinations, will yield a handful of papers

but with limited relevance towards the stated goal of determining the internal index of refraction.

Literature searches for confocal techniques that use interference is often complicated by the presence of Optical Coherence Tomography (OCT) papers. Optical coherence tomography relies on using a low coherence source that will only interfere with reference light that has a very close path length along the reference arm. The system is typically used in reflection mode for biological applications [Steiner, 2003]. In many cases a single-isotope chemical lamp is the best source for this sort of measurement. This system is not similar to the confocal holography system under development at the University of Victoria

Occasionally systems designed for surface profilometry are also found in the literature [Hamilton, 1985][Rea, 1995]. In this case the system is generally examining opaque conductors. In this case the electric field cannot propagate inside the specimen so the proportion of the signal that is not absorbed is reflected and can be compared to a reference to determine the surface profile. The concept of using optical coherence (or incoherence) holography has also been applied for surface profilometry [Chmelik, 2003]. Similarly [Yang, 2000] uses a low coherence confocal interference technique to produce volume reflection interferograms.

[Palacios, 2005] presents a Mach-Zender style confocal holograph that claims to demonstrate three-dimensional phase imaging. However the algorithm presented in the paper claims that it is valid to take a number of phase image planes in the traditional manner of confocal microscopy and phase unwrap them to produce a three-dimensional phase image. This disregards the integrated nature of the phase measurement and as such is not representative of the true phase and could not be used to retrieve the index of refraction. The method may still be valid for measuring the scattering in the specimen, which is the application the paper describes.

2.5 Comparison to Tomographic Holography

The most notable and successful analytical method that can be used to determine the internal index of refraction of specimens is holographic tomography (or tomographic holography). Optical (laser) tomographic holography is a relatively recently developed technique with the first references appearing in the 1990s [Philipp, 1992]. Tomographic

holography has been used to measure internal temperature in a fluid [Mewes 1990 & Wang, 2001], density in transonic turbulent flows [Timmerman, 1999], and gas density in nuclear reactors [Feng, 2002].

Tomographic holography enjoys a number of advantages over confocal holography but also serious drawbacks. The most difficult problem for the application of tomography techniques to fluid dynamics is a lack of projection angles. The traditional reconstruction method used in medical imaging tomography is algebraic reconstruction technique (ART) [Kak, 2001]. Algebraic reconstruction requires a large number of projections over a large angular spread with a fine and continuous angular step between projections. For fluid dynamics experiments the apparatus often precludes the use of many different and widely separated angular projections. In contrast confocal holography only requires a single entrance and exit window into the specimen chamber. In this case other techniques, such as iterative methods, are more commonly used. Typically a minimum of six projections is necessary for a simple gradient and a minimum of twelve for more complicated distributions [Feng, 2002].

Tomography also requires either rotation of the specimen or the apparatus to achieve projections over many angles. Rotation of a fluid specimen will disturb it while rotation of the holographic tomograph apparatus itself is an extremely complicated and daunting prospect.

In addition to holographic tomography, at least one reference details the use of a Hartmann-style wavefront sensor to measure the three-dimensional phase via tomography [Roggemann, 1995]. The wavefront sensor is capable of operating at a sampling rate in excess of 1 kHz (in 1995) that was far faster than CCD cameras available at that time. However the wavefront sensor would have inferior spatial and phase resolution compared to digital holography. Since each sensor element in a wavefront sensor is a lenslet focused onto a quad-cell it cannot achieve the same spatial resolution as a CCD camera.

3.0 System Design

3.1 Basis of Operation

The design chosen for the confocal scanning laser holographic microscope is based on a design concept for confocal microscopy developed by Dixon, Damaskinos, and Atkinson [Dixon, 1993]. The Dixon microscope introduces an optical loop and two galvanometer scanning mirrors in order to achieve beam scanning. Because the laser beam travels through the scanning mirrors in a forward direction and then in reverse the beam remains stationary outside the optical loop and hence is stationary on the conjugate focus aperture. A schematic of the holographic version of the microscope is shown in [Figure 11].

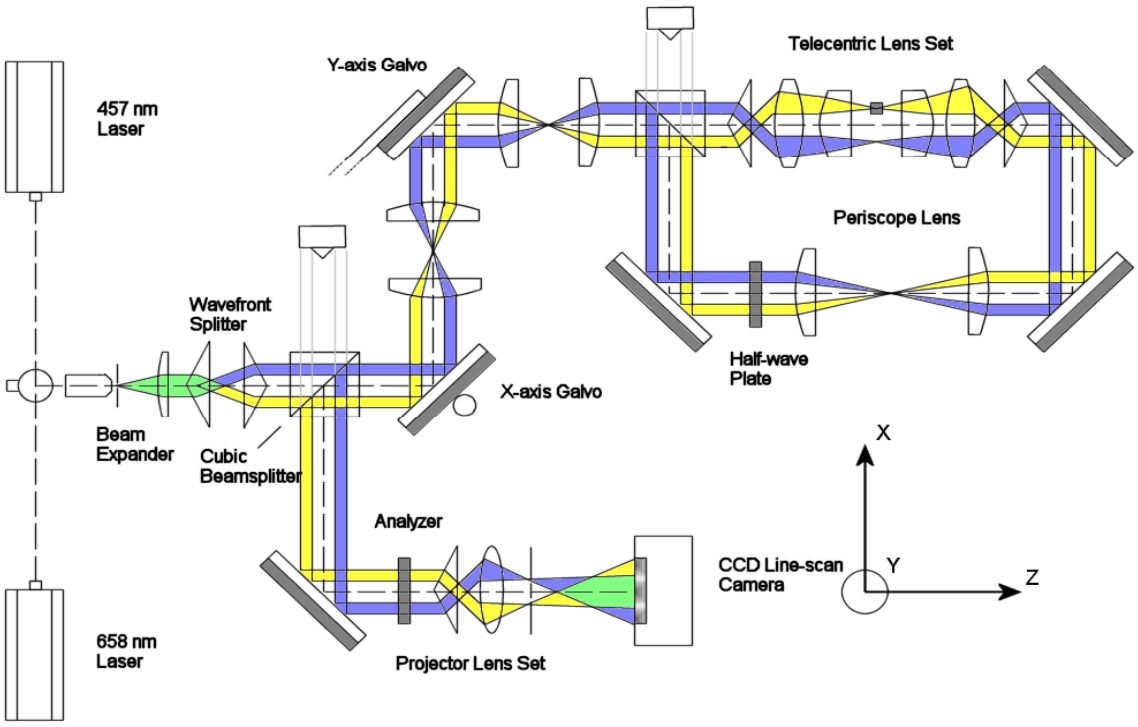

Figure 11: Schematic of wavefront-split confocal scanning laser holographic microscope is based on Dixon confocal microscope.

The coordinate system is defined as follows: the z-axis is the optical axis, meaning it is always parallel to the laser path. The x and y-axes are both perpendicular to the optical

axis. The x-axis is parallel with the surface of the optical table (horizontal) while the y-axis is perpendicular to the surface (vertical).

The illuminating source for the design is a diode-pumped solid-state (DPSS) laser operating at a wavelength of 457.5 nm, which is blue in colour. The beam is projected from the laser aperture onto a beam steerer. The beam steerer is a set of two mirrors that can be adjusted to set the height and orientation of the outgoing beam. Alternatively, the beam steerer can be rotated to accept light from a laser operating at a different wavelength – a red 658 nm laser in this case.

The beam then progresses through a beam conditioning apparatus consisting of a spatial filter and a Kepler-type beam expander. The spatial filter is an aperture that cuts the edges of the incoming Gaussian beam off. This produces a beam with steeper edges and a flatter top often called a *top hat* distribution. The pinhole filter acts to remove incoming waves that are not plane parallel with the surface of the aperture. The beam expander is a multi-component lens that enlarges the diameter of the collimated beam by a fixed amount, e.g. 30 x.

The collimated beam is then wavefront split by two Fresnel biprisms. They act to split the beam into two half-Gaussians, and then restore its parallelism to the optical axis. The beams from this point are separated into an object beam (yellow) and a reference beam (blue) as shown in [Figure 10].

The beam then progresses to a cubic beam splitter. As an approximation half of the incident beam is reflected and lost to the beam trap. The other half transmits through into the optical loop.

The dual beam proceeds to the galvanometer scanning mirrors which axially scan the beam through the x and y-axes. In-between the galvanometers and inside the optical loop are three pairs of periscope lenses explained in detail in Section 3.4.4. The periscope lenses act to flip the beam. This has the effect of reducing the walk of the beams as the scan mirrors reach greater excursions. Without the periscope lenses the laser beam would walk off the clear aperture of the optical components in the loop at very small angles of excursion for the galvanometers. They also zero the integrated beam walk through the loop so that the beams exit the loop at the same position and angle with which they

entered it. This is necessary for the dual beam to remain stationary on the conjugate aperture.

The object and reference beams are then incident on a second cubic beam splitter that forms the start of an optical loop. The optical loop is composed of the three mirrors and the aforementioned beam splitter. The incoming light travels around the loop in both directions, being reflected first to the first mirror or transmitted to the telecentric lens. When the light returns, it either is reflected/transmitted onto the beam trap, or it exits the optical loop through the scanning mirrors and travels back towards the camera.

In the optical loop is the telecentric confocal lens set as explained in Section 3.4.3. This set includes two Fresnel biprisms and at least four lenses. The biprisms act to bend the dual beams so that their angle of incidence to the lenses is roughly square to increase the field angle. The lenses themselves are telecentric in image-space. The specimen for the microscope is placed at the focus of the object beam. Since the set is symmetric the light is collimated on exiting the apparatus.

Also in the loop is a half-wave plate which rotates the polarization of the light by $\pi/2$ – the lasers are linearly polarized. It can be observed that reflected light from the sample travels through the half-wave plate twice or not at all, while transmitted light travels through once. This makes it possible to use a polarizing analyzer to filter out either the transmitted or reflected components.

Once the light exits the loop it returns to the mirrors and is restored to its original displacement and angle with respect to the optical axis. The object and reference beams then partially reflect from the first beam splitter and proceed down the signal path. First the analyzer is used to filter out either the reflected or transmitted signal component. The wavefront is then focused by an identical telecentric lens to that used for the specimen onto a dual pinhole aperture. The pinhole acts as if it is a virtual aperture at the confocal point, filtering out stray light from the two beams.

The two beams then expand and interfere with each other, forming a hologram. The introduction of a projector lens after the apertures ensures that the object and reference beam completely overlap and use the entire width of the CCD sensor. The line-scan camera detects the interference fringes and transmits them to the computer. The

holograms can be stored in memory and processed to reconstruct and display the amplitude and phase information of the specimen.

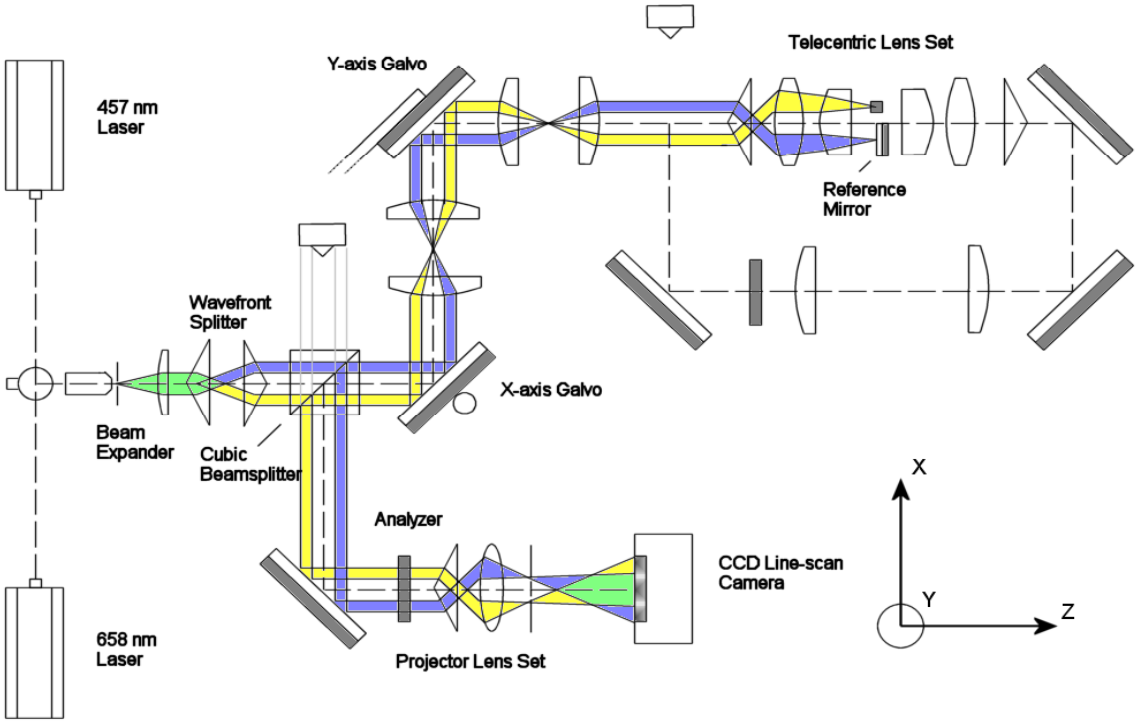

Figure 12: Schematic of reflection-mode configuration of beam-Scan confocal holographic microscope introduces a reference mirror.

The system can be adapted to function in reflection mode fairly easily [Figure 12]. A reference mirror must be introduced at the focus of the reference beam. Also, the polarizing analyzer must be rotated 90^{o} to admit the reflected p-polarized rather than the transmitted s-polarized light created by the half-wave plate. For throughput purposes the beam splitter that creates the optical loop was removed but this is not functionally necessary.

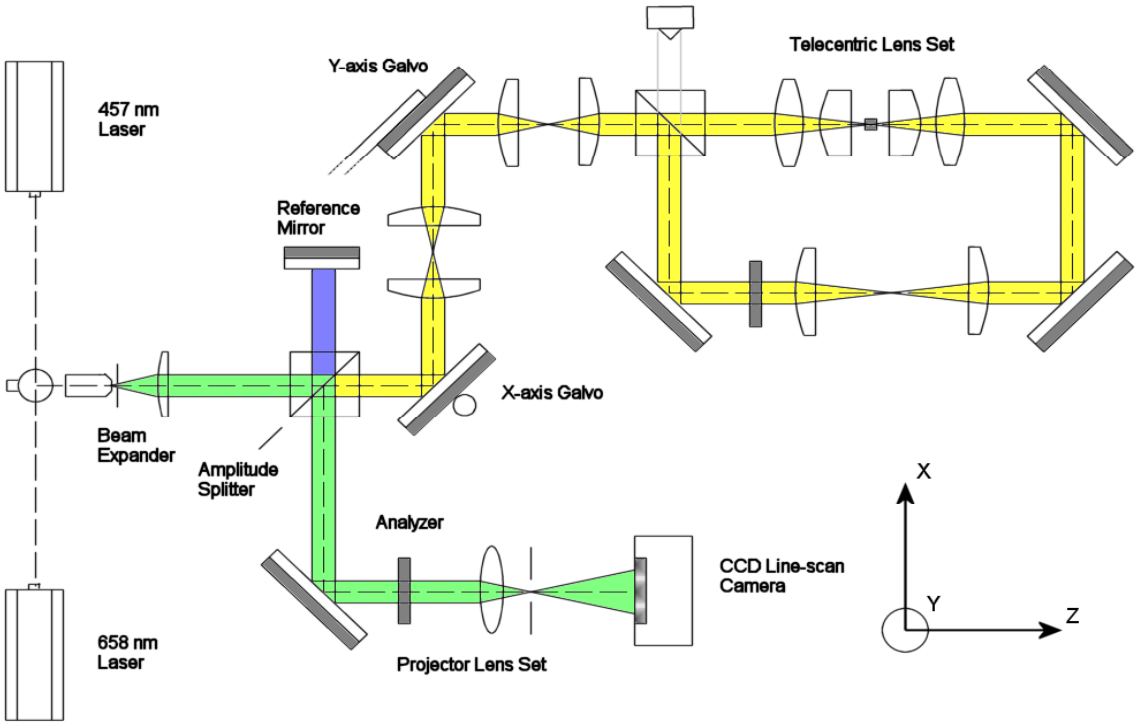

Figure 13: Schematic of amplitude-split variant of beam-scan confocal scanning holographic microscope.

An amplitude-split version of the Dixon microscope is a simple variation [Figure 13]. It introduces a reference mirror in the place of the first beam trap. In this case, the reference beam does not travel around the optical loop, so the path length of the two beams is significantly different. The source lasers must have a suitably long coherence length to still have interference since the path length difference is over a meter. This is an on-axis holography system. It would be extremely sensitive to vibration.

3.2 Parameters for Optimization

The confocal laser scanning holographic microscope is a complex system and as such it has many parameters that need to be accounted for during optimization. Most factors are not mutually exclusive with the exception of several optical parameters. For the optical parameters, a commercial optical design software package called *Zemax* was used for optimization.

3.2.1 Maximize Spatial Resolution

The greater the spatial resolution the smaller the resolved volume elements will be, increasing the level of detail the system can observe. It should be explicitly stated that this is the resolution of the system on the axes perpendicular to the optical axis, i.e. the 2-dimensional resolution. Resolution can be determined by the following factors:

1. Specimen focus spot size.
2. Pinhole aperture diameter.
3. Beam scanning resolution.
4. Diffraction limit

In terms of scanning resolution, actuators with resolution an order of magnitude smaller than the operating wavelength are available so the scanning apparatus should not influence the system's resolution.

The resolution is therefore determined by the smaller of the confocal spot or the pinhole aperture. The diameter of the confocal spot is largely determined by the optics and their aberrations. Traditional, spherical optics have a great deal of spherical aberration, which limits their ability to focus down to a tiny point. There are various tricks of optical design to correct for spherical aberration, including: doublets and triplets that combine convex and concave surfaces, aspheric lenses, and gradient index glass lenses. In the case of wavefront splitting and beam scanning, coma aberration also becomes a severe problem.

The diffraction limit is determined by

$$x = \frac{1.22\lambda}{d} f \qquad 25$$

where x is the resolution, λ is the wavelength, f is the focal length of the lens and d is the clear aperture (diameter) of the optics [Born, 1975]. For an operating wavelength of 457.5 nm, a typical focal length of 100 mm and a minimum aperture in the beam-scan microscope of 50 mm the diffraction limit is approximately 1.1 μm. Since the root mean-square spot size of the telecentric optics is minimally 60 μm the diffraction limit is not a factor.

3.2.2 Minimize System Vibration

As the holographic microscope operates on the basis of the difference in path length between the object and reference beams it is extremely sensitive to vibration in the table. Lower frequencies are of greater concern than higher frequency vibrations. This is due to the fact that for harmonic waves the power is related to the square of both the frequency and amplitude. Hence, for the same energy level, low frequency vibrations will have higher amplitude. Practically it is more difficult to filter out low frequency vibrations. Also, high frequency vibrations can be dealt with more easily through time integration of the signal, at the expense of some motion blur, without impacting scanning speed.

Vibration can be controlled through a number of factors:

1. Locate the holograph in a quiet vibration area or on an isolation pad.
2. Reduce the transmission from the floor to the table, through active and passive isolation systems.
3. Minimize and increase the frequency of the structural resonances of the table and opto-mechanics.
4. Reduce the vibration caused by optical scanning of the beams.

Vibration in a building is generally caused by external sources such as atmospheric wind pressure. It can be further exacerbated by the operation of machines in the building. In the case of the engineering building, this includes the HVAC system, milling machines, etc.

Isolation systems attempt to reduce the vibration energy by damping it. There are two basic types, passive and active vibration isolation. Passive isolation systems always resonate at some frequency where they amplify rather than damp the vibration.

Pneumatic air springs and elastomer dampers are representative of passive isolation system. Active systems record the displacement and use a servo-motor of some sort to move anti-synchronous to the detected vibration. Active systems typically use piezo-electric actuators coupled to an accelerometer. The accelerometer records the vibration signal and then contracts the actuators to cancel it.

The structural resonance and resonant frequency can be altered by the geometry and stiffness of the various components. For example, a tripod support structure resonates much less at low and high frequencies than a four-post system. Increasing the stiffness to weight ratio of the components will push resonances to higher frequencies where they can be more easily dealt with.

The various motors and actuators used to scan the sample beam through the target can all produce vibration. If they are allowed to settle for each hologram taken, then the vibrations will be transient.

3.2.3 Minimize Air Current and Acoustical Coupling

A corollary to mechanical vibration is the ability of air currents and acoustical noise to disturb the apparatus. Air currents result from pressure variations inside a building, and are almost always created by air conditioning and heating systems. If a system is actively or passively isolated from floor vibrations, air currents will provide the majority of energy to induce oscillations in the optical components. In addition to physically disturbing the apparatus air currents can deposit dust and other contaminants on the optics.

Air currents and acoustical coupling can be dealt with through a variety of means:

1. Closing all air conditioning vents in the room to prevent flow.
2. Installing a curtain around the apparatus.
3. Installing a solid enclosure over of the apparatus, optionally with a positive pressure applied.

Closing air vents can reduce the flow in a room substantially but will not eliminate it. A heavy curtain is most useful for containing dust. It also stagnates flow by damping it. An enclosure is the most expensive solution, and involves installing solid plastic panels over of the optical table. A small positive pressure from a filtered central air source can be supplied so that no dust can enter the enclosure. If the enclosure is installed on the

surface of the optical table it will act as a sail for any air currents in the room. As such it should not make physical contact with the isolated tabletop.

3.2.4 Maximize Convergence Angle

The convergence angle of the confocal probe largely determines the resolution of the holograph: the greater the convergence angle, the faster the change in irradiance as a function of distance along the optical axis from the confocal point. As a result, the contribution from volume elements (voxels) further from the confocal point is reduced with greater convergence. This has the effect of increasing the influence of the probe (focus position) on the signal.

The convergence angle allows an upper bound for the z-axis resolution to be established. If a convergent beam with a half-cone angle α is used to sample an object with radius a [Figure 14] then the z-axis resolution is at least

$$z_{res} \leq \frac{a}{\tan\alpha}. \qquad 26$$

Interpolation may allow superior resolution, but fundamentally the resolution is determined by the outer extent of the marginal rays. This also means that the z-axis resolution of an object's position is dependant on its physical size in x and y-axes.

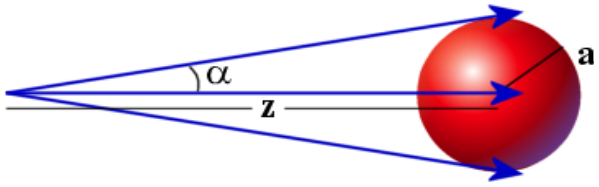

Figure 14: Z-axis resolution is a function of convergence angle based on the simple trigonometry of chief and marginal rays.

The convergence angle is determined by the laser beam radius and the focal length (not the f/# per say) of the telecentric lens set. As spherical lenses with a short focal length must have a larger radius of curvature they are geometrically larger and reduce the potential space available for a specimen. Similarly the larger the laser beam radius the larger the clear aperture of the optics is needed to pass the beams without vignetting. Hence increasing the confocal angle will decrease the sample size. Aberrations also increase with decreasing focal length so the probe size will increase. A realistic

maximum for cone half-angle is about 15^{o}, which limits z-axis resolution to about one forth that of x and y-axis resolution.

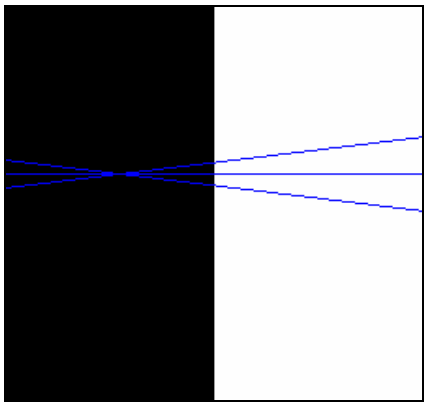

Figure 15: An ill-conditioned specimen with only variation along optical axis is not resolvable with confocal holography mechanism (assuming no refraction).

It follows that if a specimen has infinite extent on the perpendicular axes that a convergent beam cannot locate any variation along the optical axis. Consider the case of two pieces of glass cemented together [Figure 15]. In order to retrieve the three-dimensional index of refraction from the phase it is necessary to assume that the light rays travel in straight lines. For tomography, it is generally considered that $\Delta n/n$ cannot be greater than 2 % for this to be a reasonable assumption [Kak, 2001]. Regardless of the position of the focus probe the marginal and chief rays will always have the same integrated phase shift and the interface cannot be located if we assume that Snell's Law does not apply.

If one imagines the case where the sections of glass become infinitesimally thin and a great many sections are stacked together then a linear gradient of index of refraction results. In this case it would be similarly impossible to determine anything other than the mean index of refraction using the method of confocal holography.

3.2.5 Maximize Specimen Size

Specimen size is determined by two factors:

1. The geometrical space between the confocal lenses.
2. The maximum distance the laser beams can be translated before they either vignette or cross the mid-point of the biprisms.

The space available along the optical axis for the specimen is approximately half the distance between the inner lenses. Any further translation will result in a specimen-lens collision. The x and y-axis space is determined by the clear aperture of the optics and the separation of the beams. The specimen size determines the scale of experiments that the holograph is capable of examining.

3.2.6 Maximize Scanning Speed

For monitoring a changing process the faster the scanning system can raster the beam through the sample the better. At the same time, the amount of vibration produced by the movement of the scanning system needs to be minimized. There is also the issue of absorption of laser energy by the sample. In particular samples with a high coefficient of absorption at the operating wavelength are in danger of excessive thermal loading. This can limit the non-invasive nature of the device when used for temperature measurement and potentially damage the specimen.

An estimate of the irradiance at the beam focus in the specimen is

$$I = \frac{T_o T_b P}{2\pi r_{rms}^2} \qquad 27$$

where T_o is the estimated transmittance through the optics (~ 0.75), T_b is the transmittance through the beam splitters (~ 0.85 for polarizing), P is the power of the laser (0.1 W), and r_{rms} is the root mean square spot size the optics can focus to. Simulations have shown that for wavefront split systems r_{rms} varies from approximately 7.5 μm to 80 μm, depending on the system parameters. Thus the energy flux could vary from 10^6 to 10^8 W/cm^2. This contrasts an oxyacetylene flame with an energy flux of approximately 10^3 W/cm^2. It is evident that the system will damage materials that have a high coefficient of absorption at the laser wavelength. For biological specimens in particular it will probably be necessary to reduce the beam power. The primary blue laser has the capacity to reduce its power output or optically a polarizing filter could act as an attenuator.

3.2.7 Maximize Camera Irradiance

The higher the intensity of the individual fringes, the faster the CCD (which is an integrating device) can sample images with high contrast. This has a number of

advantages. Principally, the impact of system noise in the camera electronics is reduced with high signal strength. Also, if the scanning mirrors raster the beam without settling at each sample the motion blur is reduced.

The irradiance on the camera is determined by the power of the laser, the transmittance of the optics (most notably the beam splitters), and the aperture diameter of the double pinhole.

$$DN = 2T_o \cdot T_b \cdot T_p \cdot B \cdot \frac{P}{A \cdot S} \qquad 28$$

where DN is the digital value observed (out of 256 for 8-bit sampling), the T_o is transmittance through the optics (~ 0.56), T_b is the transmittance through the beam splitters (~ 0.71), T_p is the transmittance through a 10 μm pinhole (~ 0.1), A is the projection area at the CCD detector (~ 17.5 cm^2 for 8k pixel Piranha2), B is the responsitivity of the camera to the wavelength (~ 10.5 DN/nJ/cm^2 at 658 nm, 6 DN/nJ/cm^2 at 457 nm), P is the power of the laser, and S is the sample rate of the camera. The factor of two is present because interference fringes have a peak constructive irradiance twice that of the original beam.

For a 100 mW blue laser the camera is capable of sampling at 10.6 kHz while maintaining the full 8-bit range of the camera output. Since the maximum speed of the camera is 9 kHz this will allow for some beam attenuation by the specimen.

3.2.8 Optimize Fringe Spatial Resolution

As an approximation, the dual pinhole apertures can be considered point sources in order to determine the carrier frequency of the hologram. From the Young double slit model it can be shown that two point sources produce fringes with a separation Δy of approximately

$$\Delta y = \lambda \frac{L}{a} \qquad 29$$

where λ is the wavelength, L is the distance to the sensor from the aperture, and a is the separation between the apertures [Hecht, 1998]. Given a pixel dimension of d_p then the carrier frequency is approximately

$$f_c = \frac{d_p}{\Delta y} = \frac{d_p a}{\lambda L}. \qquad 30$$

If the carrier frequency is too small – very thick fringes – the zero band and sidebands may alias (overlap) in frequency space. If the carrier frequency is too large quantization error will be introduced from the pixel sampling. The Nyquist frequency in this case is ½ pixel^{-1}. The optimal carrier frequency lies somewhere in the middle. In order to select a suitable carrier frequency it is desirable to:

1. Completely overlap the object and reference beam over the width of the camera. Thus neither the edges of the beam or sensor are wasted.
2. Vary L – the distance from the aperture to the camera – in order to select f_c because the other three parameters are fixed.

Accomplishing these two goals will require the development of a projector lens.

3.2.9 Minimize Component Changes (for Different Wavelengths)

The use of two distinct wavelengths in the holograph imposes a number of problems in the design. Lenses must be designed to be dichromatic for the expected wavelengths. This is not a realistic requirement for a first generation device but it could be a consideration for the future when greater funding is available for the purchase of dichromate lenses.

It is desirable to be able to switch from one frequency to the other quickly, so that the holograph can analyze an ongoing process with both wavelengths. Ideally, the system could be switched from one wavelength to the other without disturbing the system by touching the table. Potentially all the changes could be done with computer controlled actuators. The analyzer, half-wave plate and beam steerer are components that have to be adjusted when the operating laser is changed.

3.3 Opto-mechanical Design

The opto-mechanical design of the system involves the accurate positioning and calibration of optical components. This is accomplished by a series of optical mounts, posts, and stages.

The standard for positional accuracy is very high. The optical path length of the beam-scanning system is approximately 2.5 m. Thus a small angular deviation of 1 mrad at the

source would result in a beam translation of 2500 μm at the pinhole aperture. Considering that the root mean square spot size of the telecentric lenses is about 80 μm at a wavelength of 475.5 nm it is evident that small errors in positioning can produce huge errors in beam position. Similarly collimation of the beam must be maintained over the entire length.

There are a number of critical issues involved in opto-mechanical design. They include:

1. Setting the optical height of the system. All of the various positioning stages and mounts add some degree of elevation to their component. For simplicity, it is easiest if all components are at the same height. It is also desirable to minimize the overall beam height because the taller the components, the less stable they are. This effects the mechanical vibration of each optical component.
2. Providing the necessary axes of freedom for the various optical components. There are six axes of freedom: x, y, z, pitch, yaw, and roll. Typically a mount will fix some axes, while in other axes components may be symmetrical. For example lenses are symmetric in roll. A biprisms only requires rough positioning accuracy in the y (vertical) axis due to its symmetry.
3. Ensure that the positioning stages have sufficient range of motion. The mounting pattern on the optical table (1.5 x 2.4 m) consists of M6 holes on 25 mm centres. However, some stages may only have +/- 10 mm of motion, so they do not provide complete coverage. In this case additional positioning equipment such as rails may be necessary.
4. Ensure that the opto-mechanics chosen physical fit together, both in terms of dimension and mountings with screw patterns.

The actual calibration of positions is done in two stages. First, the components are positioned with the aid of digital callipers and height gauges. This can gauge their position to within approximately 10 μm. The fine adjustment is then done optically with the aid of a shear plate collimator and area-scan CCD camera. Most stages have differential micrometers with a resolution less than 1 μm. Some components are driven by motorized stages that have a position accuracy of 100 nm.

3.3.1 Computer Assisted Design Model

The basic procedure for creating CAD descriptions of the various components starts with generating the individual parts from their catalogue drawings. Since catalogue drawings are not always extremely detailed, the part must be dimensioned to its maximum geometric limits. This is the most time consuming portion of the opto-mechanical design process; it would be very helpful if more manufacturers could provide CAD drawings of their components from their websites.

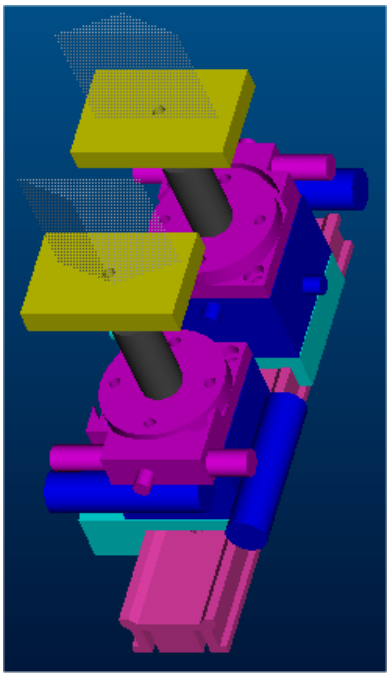

Figure 16: CAD assembly example: the wavefront splitter assembly.

Once a basic catalogue of stages and mounts has been assembled it is a relatively simple process to create subassemblies [Figure 16], and then arrange all the subassemblies onto the optical table [Figure 17].

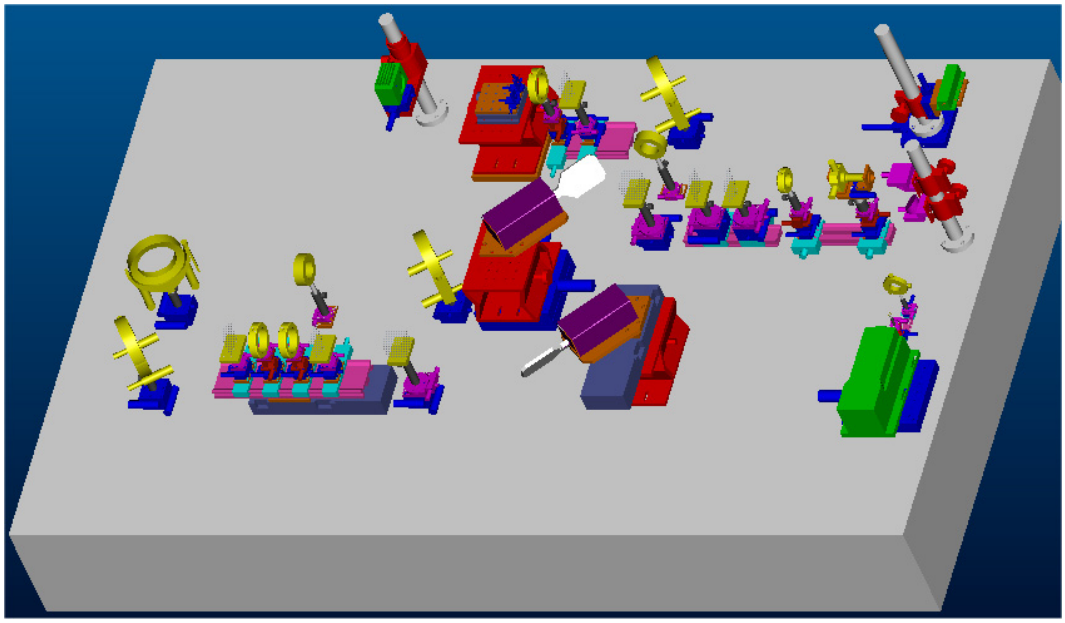

Figure 17: CAD visualization of beam-scan confocal holographic microscope (deprecated).

3.4 Optical Design

Zemax is a popular optical design software package published by Zemax Development Corporation of Bellevue, Washington. The software is not especially user friendly but it is capable of modeling most optical phenomena and has very powerful optimization and analysis features.

Zemax has two basic modes of operation. In sequential mode rays may only propagate from one surface to the next by the laws of geometric optics. This has the advantage that it is possible to construct and optimize equations representing the optical layout. For example, the system can be optimized to minimize the wavefront error and spherical aberration by setting surfaces and positions to be variables. Typically the more degrees of freedom the system is given the better the optimization performance. For an optical system degrees of freedom are represented by the type of glass used with its associated index of refraction and dispersion, the radius of curvature of the lenses, the thickness of the lenses, and the separation between the various lenses. Optical performance is limited by the various aberrations that may be present in a system. There are six main lower-order aberrations [Hecht, 1998]:

1. Chromatic aberration: is caused by the fact that index of refraction is a function of wavelength. Thus for refractive optics their specifications depend on

wavelength. Mirrors do not suffer chromatic aberration. Similarly for a monochromatic source for a laser chromatic aberration can be eliminated.

2. Spherical aberration: is caused by the fact that a lens with a spherical surface cannot focus all rays to the same point. The marginal rays will always have a shorter focal length than the rays closer to the middle of the lens. Spherical aberration can be reduced using a greater number of surfaces each of lesser power or by using an ideal aspherical surface – typically described by a conic profile – that is designed to focus all the rays to the same point. .
3. Comatic aberration: occurs when the incoming rays to a lens are offset from the optical axis by some angle. It is also known as coma. For a wavefront split holograph coma is a very serious source of aberration because of the need to maintain separation between the object and reference beams forces them to travel through all lenses separated some distance from the optical axis. The name coma is derived from the comet-like flare present in images effected by comatic aberration.
4. Astigmatism: is a point source of light being spread out into a line when it enters a system at a different angle from the optical axis.
5. Field curvature: is a representation of the phase shift across the wavefront. For a convex lens the marginal rays will have a shorter path through the high index glass, and vice versa for a concave lens. Field curvature can be reduced by mixing convex and concave surfaces.
6. Distortion: is caused by differing magnification between the on and off-axis rays. As a result the image will be stretched or compressed from the corners.

Non-sequential mode operates more like a Monte Carlo simulation. It is capable of physical optics such as splitting and scattering rays. All holographs require either wavefront or amplitude splitting so only non-sequential mode can simulate an entire holographic system. Non-sequential mode is also capable of simulating interference phenomenon which makes it invaluable for hologram simulation.

3.4.1 Sample-Scan Prototype Model

The sample scan design is intended to be used for initial characterization of the behaviour of the confocal holograph [Figure 18]. It is a wavefront split system. With the

exception of the biprisms all of the components are standard commercial models and hence inexpensive and quick to buy. The biprisms are a legacy asset from the Canadian Space Agency. The sample-scan prototype was simulated in Zemax [Figure 19].

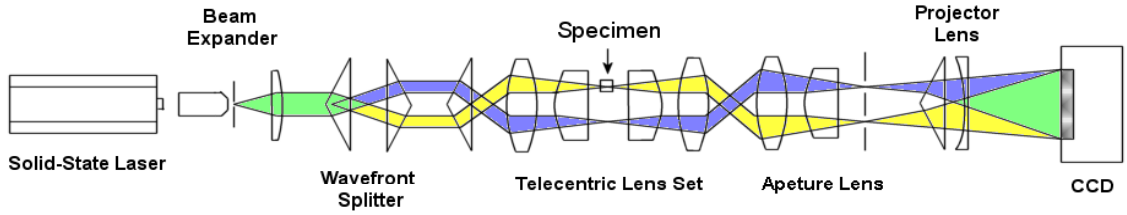

Figure 18: schematic of prototype sample scan confocal holograph (yellow object beam, blue reference beam, green overlapped beams).

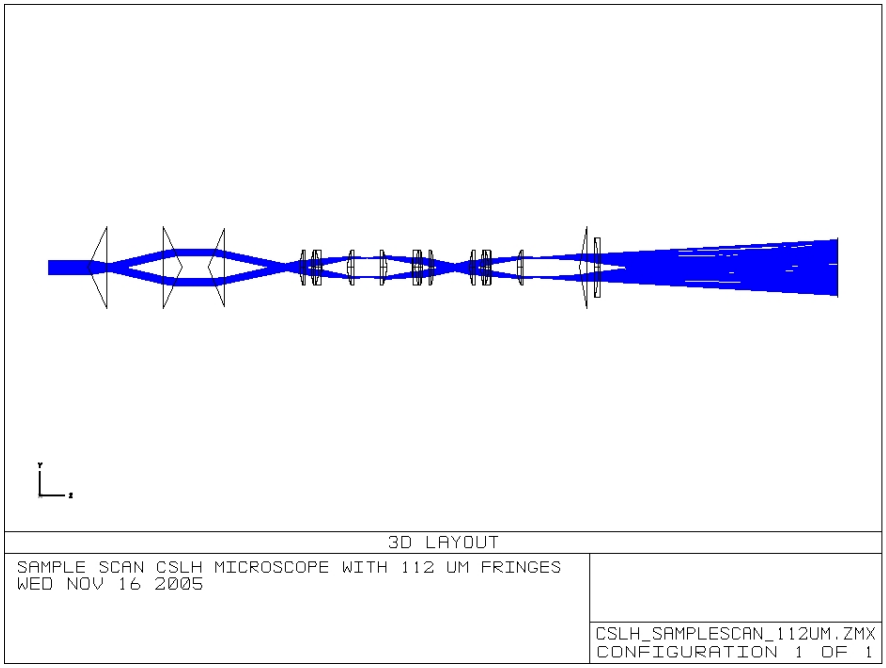

Figure 19: Sample scan CSLH microscope layout by Zemax modeling package

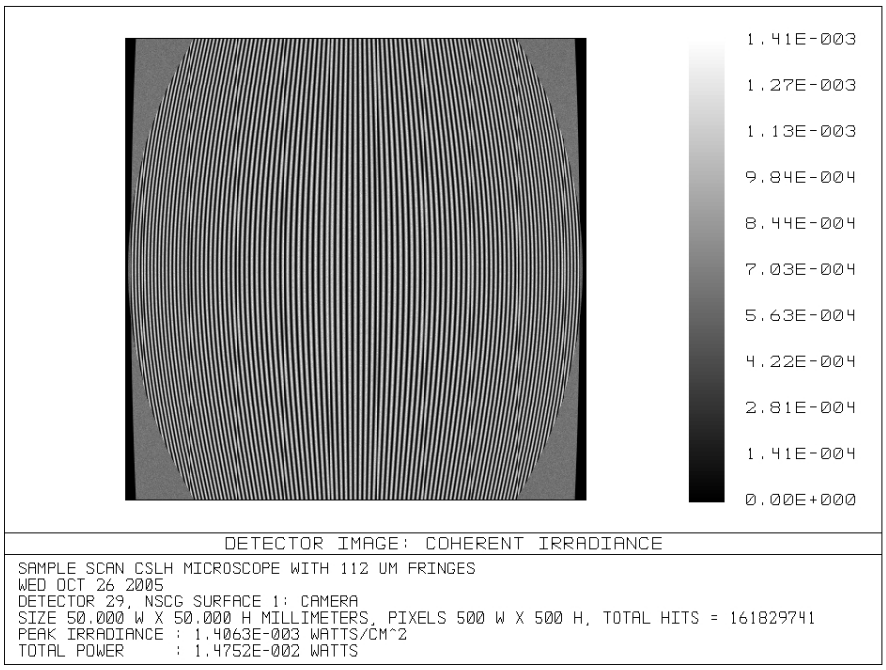

Figure 20: Sample scan CSLH hologram simulated by Zemax demonstrates expected fringe carrier frequency of 0.014 λ/pixel (circular and vertical features are artifacts due to low screen resolution).

The simulated hologram [Figure 20] has 99 fringes across 49.3 mm yielding a carrier frequency of 0.5 mm^{-1}. Given 7 μm pixels then the discrete carrier frequency is 0.014 fringes / pixel.

3.4.2 Beam-Scan Model

The beam scan model is considerably more complicated to simulate due to the introduction of cubic beam splitters [Figure 21]. The critical factor determined by the simulation is the maximum excursion of the galvanometer scanning mirrors before the beam walks off the clear aperture of the optics. In particular there are two limitations: the relatively small size of commercial beam splitters (51.2 mm) and the knife-edge of the Fresnel biprisms. The maximum angular scan of the system is approximately 0.7° which the telecentric lens transforms into a rectangular scan of ±1.4 mm. This is considerably less than the desired ±5.0 mm. Since the cost of larger custom beam splitters was prohibitive this limitation will have to be accepted.

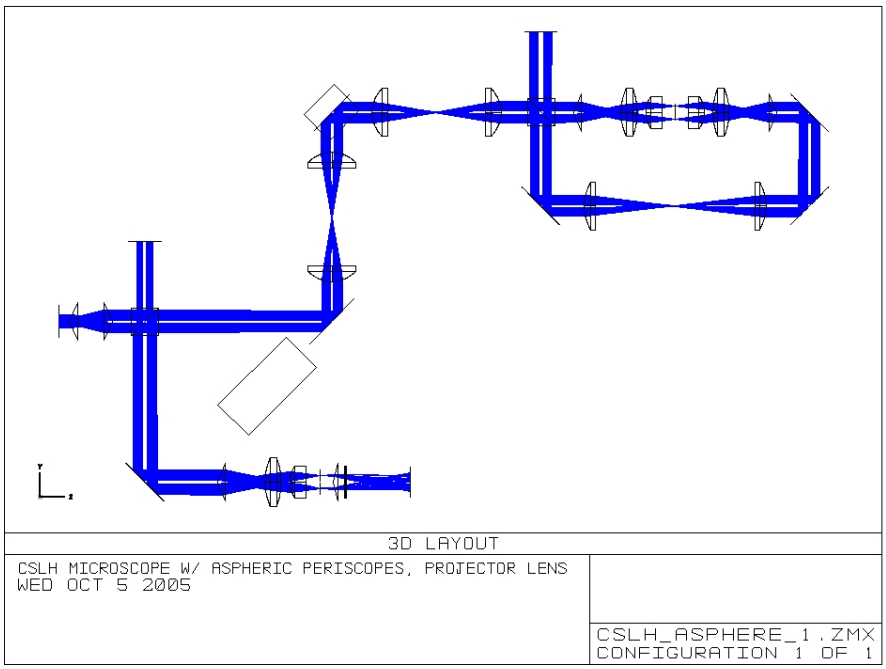

Figure 21: Beam scan CSLH microscope simulation by Zemax non-sequential mode.

A simulated hologram is not shown because Zemax does not have the capacity to probably model polarizing cubic beam splitters operating in multiple directions. As a result the dual beams are allowed to propagate in both directions around the optical loop in the simulation. Due to optical aberrations the two paths are not identical and as a result there are two object and two reference waves. The resulting interference pattern shows the presence of beats that will not be present in the physical system.

The beam walk on the confocal aperture is also not negligible. The introduction of the biprisms to the telecentric set makes it impossible to completely zero the beam walk through the optical loop as explained in Section 3.4.4. This will necessitate the use of 0.25 mm diameter pinhole apertures to avoid occluding the beam at its maximum excursion angle.

Table 2: Beam Walk at Confocal Focus Probes

Scan Probe	Beam Walk
Specimen	2 mm/°
Aperture	0.16 mm/°

3.4.3 Telecentric Lens

A lens is called telecentric if it collimates all chief rays at either the image or object. Telecentric lenses are commonly used in machine vision because they eliminate parallax error [Michalski, 2005]. Practically speaking an image-telecentric multiple-element lens can be used in the confocal holograph to transform a x-y axial angular scan from a galvanometer mirror into a rectangular coordinate x-y scan.

In all cases biprisms are used in conjunction with the telecentric lenses. The biprism increases the field angle of the object and reference beam incident on the lens system. In turn the separation between the two beams at the focus is increased. This is necessary in order to have sufficient physical space for the specimen.

Two sets of telecentric lenses were developed. The first set for the prototype sample scan configuration was developed chronologically later [Figure 22]. It was designed using only commercial lenses to reduce both cost and lead time. It is impractical to use commercial lenses for the beam scan system because they do not offer enough degrees of freedom to achieve acceptable optical performance.

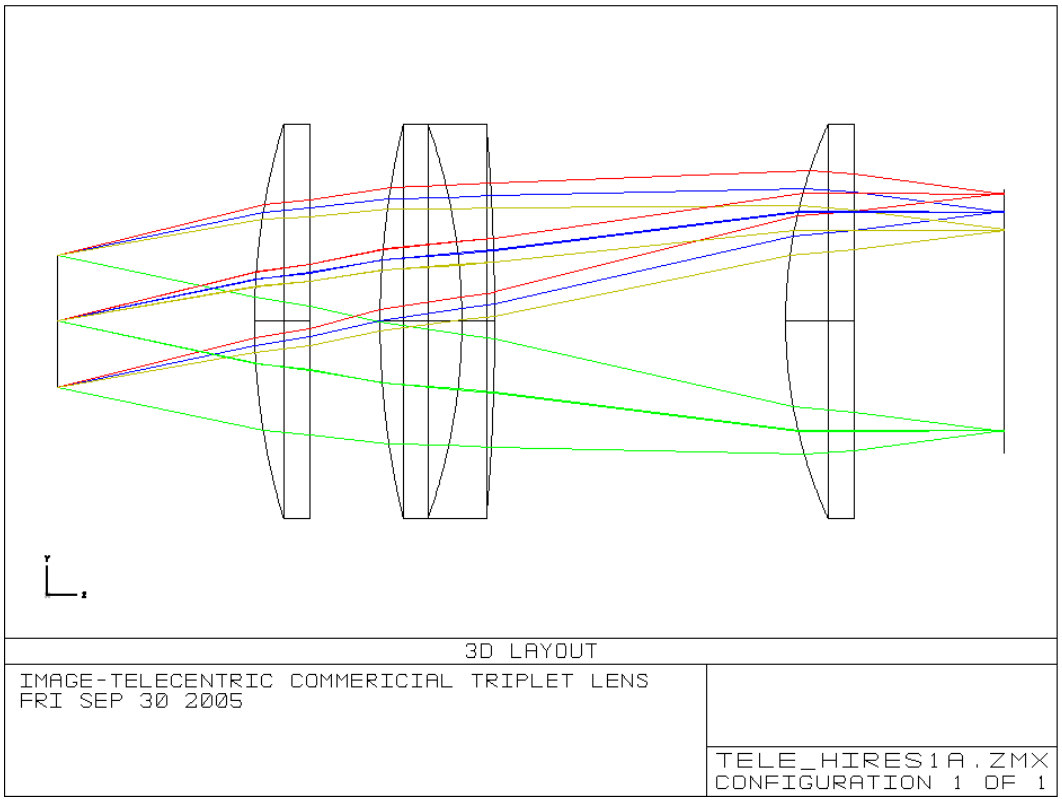

Figure 22: Ray trace of lens for sample scan that is telecentric in image space using commercial lenses showing field angles of 10° (brown), 12° (blue), 14° (red) and -12° (green).

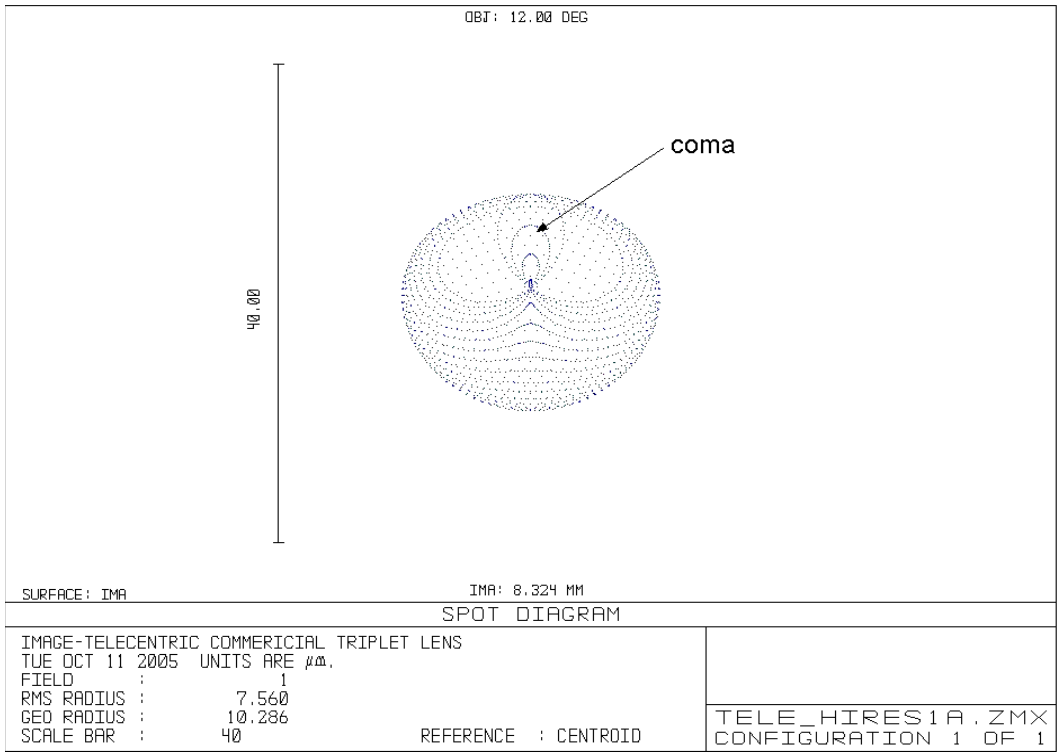

Figure 23: Spot size for field angle 12° shows significant coma present in 7.5 RMS μm spot at focus position.

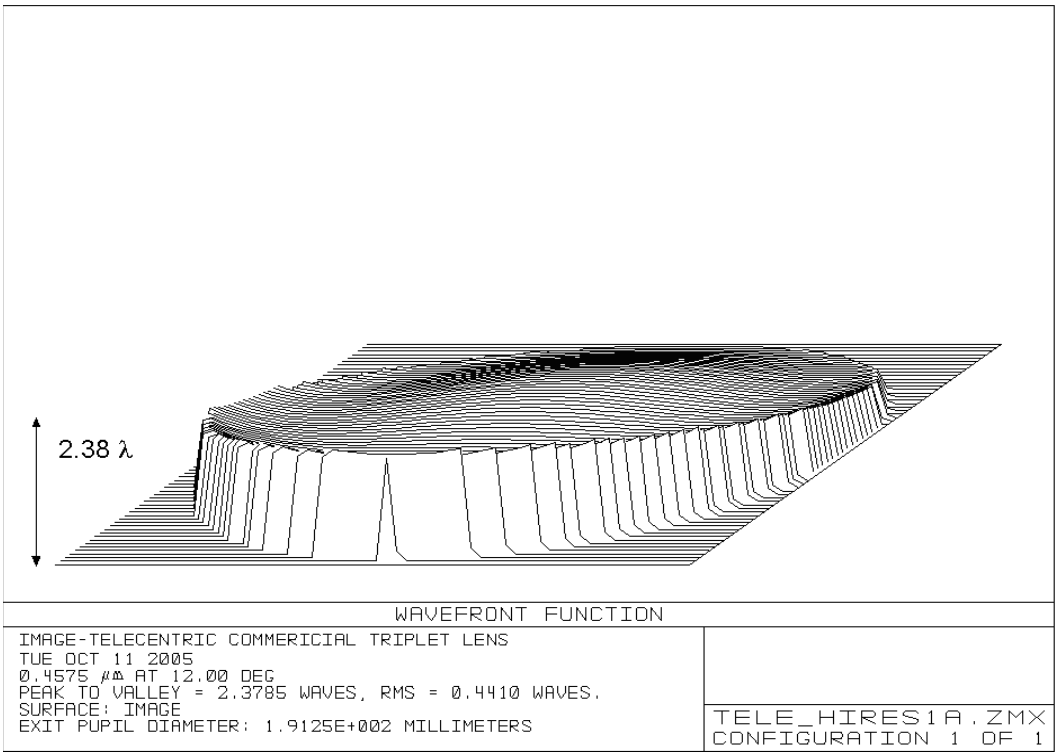

Figure 24: Wavefront error for sample scan telecentric lens system has maximum error of 2.38 λ and RMS error of 0.44 λ.

The requirements for generating a telecentric lens for the prototype sample scan system are not very strict. Because the beam does not actually change its orientation the system only need be optimized for a fixed beam field angle determined by the biprisms. This allows for much better optimization of the optical aberrations with fewer degrees of freedom [Figure 23, 24].

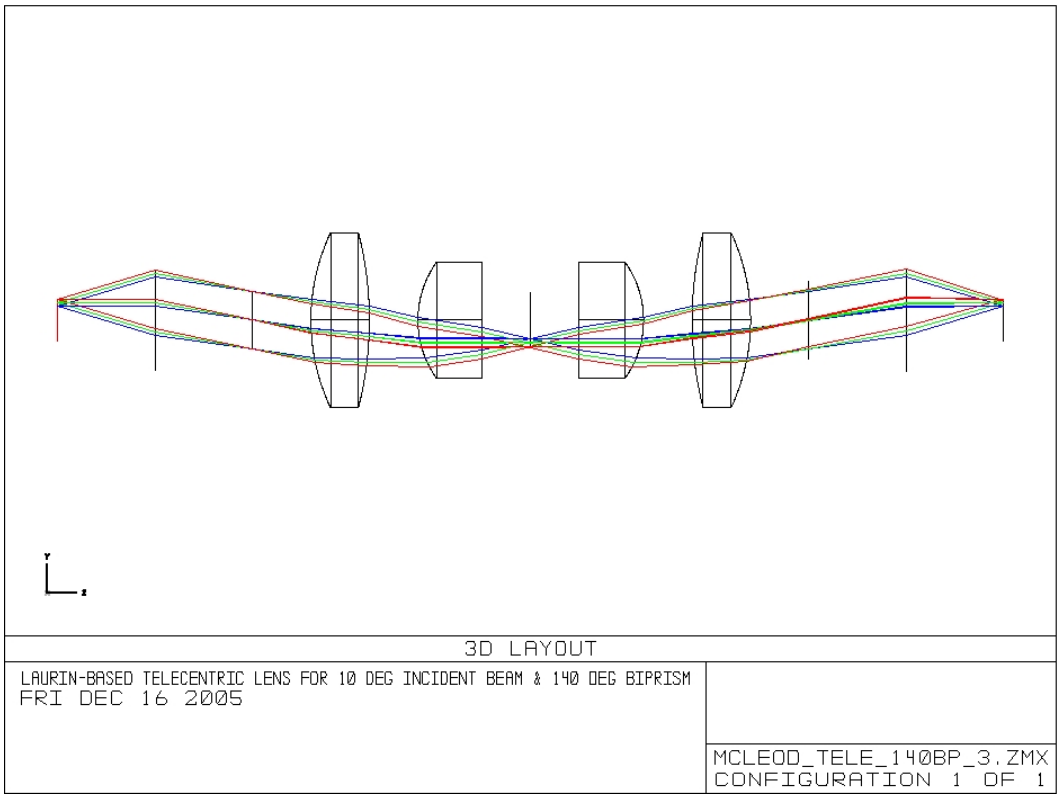

Figure 25: Ray-trace image-telecentric lens for beam scan microscope showing field angles 7.03° (red), 8.82° (green), 10.63° (blue).

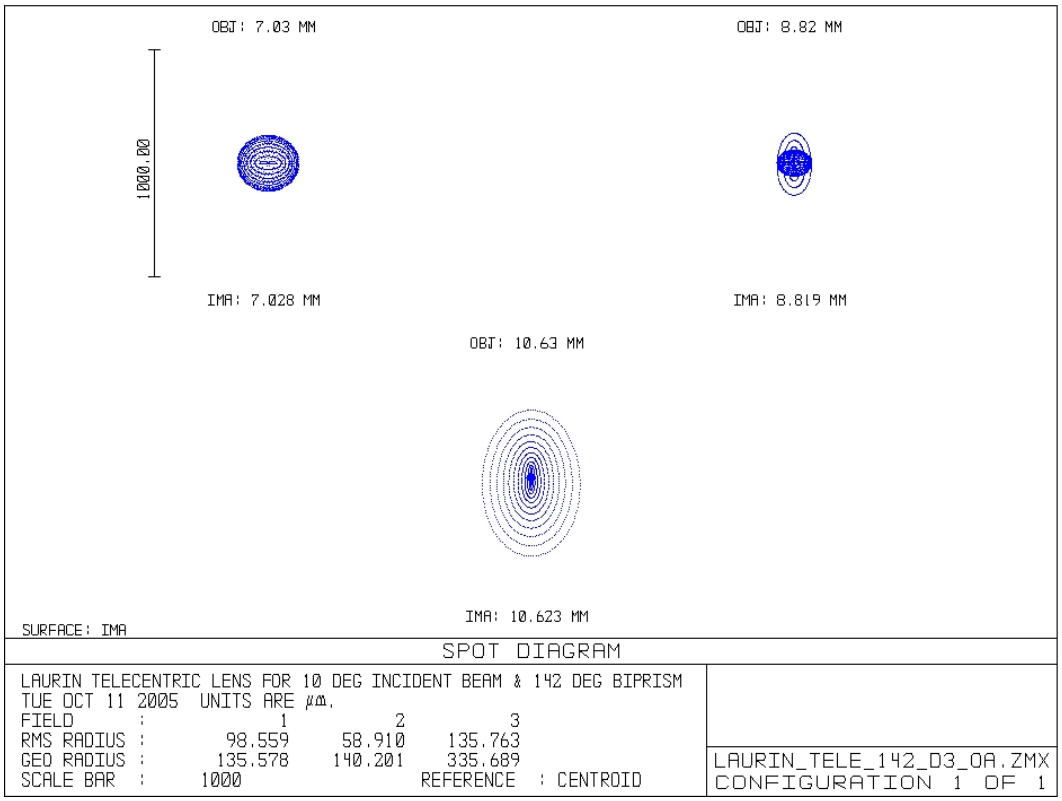

Figure 26: Spot size for field angles of 7.03°, 8.82°, 10.63° shows 98.6, 58.9, and 135.7 μm RMS spot size respectively.

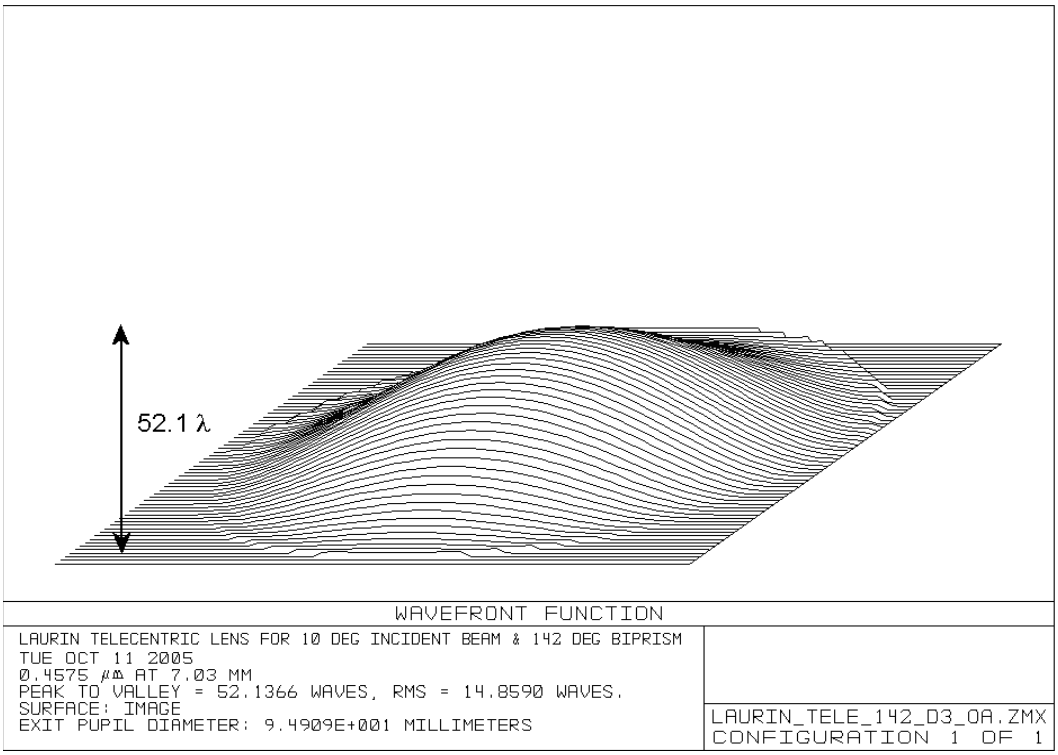

Figure 27: Wavefront error for beam scan telecentric lens system with maximum error of 52.1 λ and RMS error of 14.9 λ.

The telecentric set for the beam scan system was originally developed by Denis Laurin and later modified to operate at different field angles and wavelength [Figure 25][Laurin, 2005]. The optical performance of the system is inferior by an order of magnitude to the prototype lenses [Figure 26, 27]. This is due to the need to optimize the beam scan telecentric lenses over a variety of field angles while balancing the contribution of spherical and coma aberration.

Table 3: Summary of Telecentric Optical Performance

Lens Design	Field Angle	Spot Size (μm rms)	Wavefront Error (λ rms)
Commercial Telecentric	12°	7.5	0.44
Laurin Telecentric	7.03°	98.6	14.86
	8.82°	58.9	
	10.63°	135.8	

3.4.4 Periscope Lenses

The periscope lenses act as an optical control system for the beam scanning system. First they invert the image an even number of times. This insures that the beam exits the

galvanometers along the optical axis. If the image was inverted an odd number of times it would exit at twice the excursion angle of the galvanometers.

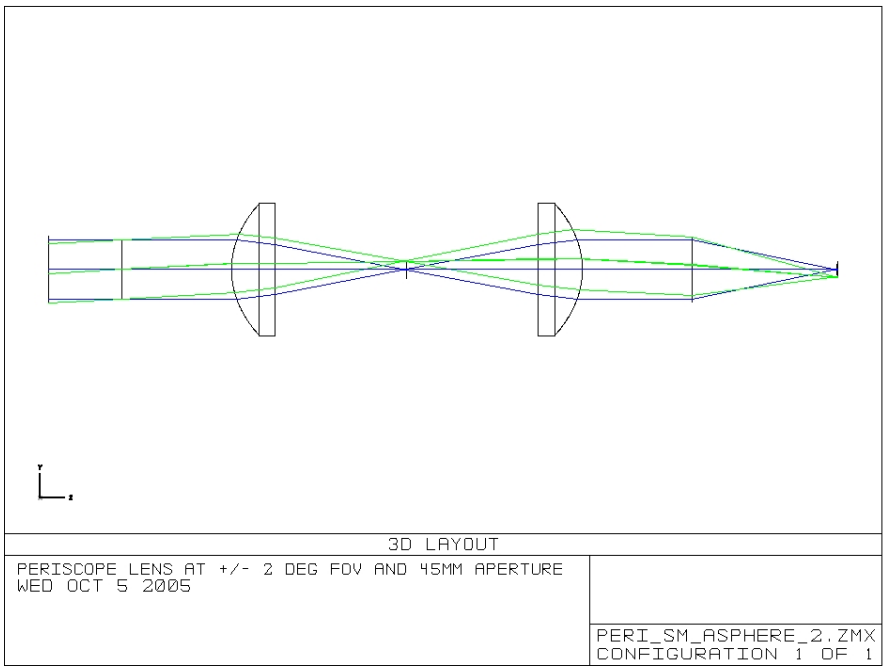

Figure 28: Ray-Trace of periscope lens for galvanometer scan mirrors at field angles of 0° (blue) and 2° (green).

Second the periscope lenses reduce the beam walk so that as the galvanometers scan they do not translate the beam off the clear aperture of the optics. Each time the beam is inverted the beam walk is halved. If the pupils of each set of periscopes are exactly overlaid (along with the telecentric lens set) the beam walk throughout the system will be zeroed. Practically the presence of the biprisms in the telecentric set prevents this: the pupils of the telecentric set are located in between the lenses and biprisms. This will result in a small beam walk at the pinhole aperture. If the pinhole is smaller in diameter than the induced beam walk the signal will be completely occluded.

There are two types of periscope lenses in the microscope. The galvanometers each have an identical pair of lenses [Figure 28] while the optical loop has a pair with a longer focus length. For ultimate performance the periscope lenses have aspherical surfaces. This maximizes the performance of the singlets in the short working space available.

Table 4: Periscope Lens Optical Parameters

	Spot Size **(μm rms)**	Wavefront Error

	0.0°	0.5°	1.0°	1.5°	2.0°	3.0°	(λ rms)
Optical Loop	24.1	22.7	19.5	18.9	27.5	68.4	0.93
Scan Mirror	54.2	50.8	41.3	29.7	33.2	104.7	2.63

3.4.5 Polarization Filter

Standard beam splitters use a partially reflecting metal mirror to reflect part of an incident light beam while transmitting the rest. They are considered non-polarizing. Absorption is reduced by the addition of a dielectric layer that reduces the amount of light absorption. These are known as hybrid beam splitters. These systems do lead to a large amount of beam attenuation in the Dixon-microscope system. The beam must pass through beam splitters an effective total of three times. At a transmittance of 0.46, the beam will be attenuated to $0.46^3 = 0.09$ of its initial value from the beam splitters alone. Greater throughput is desirable.

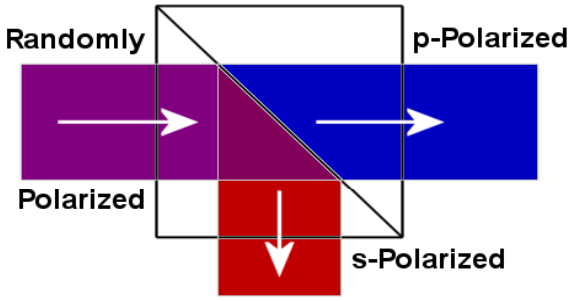

Figure 29: Polarizing cubic beam splitter passes p-polarized light and reflects s-polarized light.

An alternate technology uses only a dielectric layer to conduct beam splitting. These are polarizing; typically they pass p-polarized light and reflect s-polarized light [Figure 29]. Since the lasers used are linearly polarized it is possible to take advantage of polarizing beam splitters to increase beam throughput.

Table 5: Transmittance for Melles Griot Beam Splitters [Melles Griot, 1999]

Type	Wavelength (nm)	p-Transmittance	s-Transmittance
Hybrid	457.5	0.46	0.40
Hybrid	658.0	0.45	0.42
Polarizing	457.5	0.92	0.08
Polarizing	658.0	0.95	0.05

The table shows transmittance and reflectance for a Melles Griot brand cubic polarizing beam splitter. If the light is initially p-polarized, it will almost entirely

transmit through the first beam splitter and not onto the beam trap, and similarly for the second beam splitter.

The introduction of the half-wave plate is critical. The laser beam travels through the half-wave plate after passing through the specimen. It is then rotated into s-polarization. The s-polarized light will then reflect off the two beam splitters into the signal path and onto the camera. As a result, the transmittance increases up to $0.92^4 = 0.71$. The transmittance with the polarizing beam splitters generates an increase in throughput of a factor of eight from the hybrid beam splitters.

The use of polarizing beam splitters also removes a unique feature of the optical loop. Where previously the laser beam traveled in both directions around the loop now it only travels in a clockwise direction. Propagation in only one direction is advantageous because aberrations from the optics force the loop to be not perfectly symmetric, only nearly so. As a result without polarizing beam splitters there would be two distinct object beams and two distinct reference beams. The small variation in the wavefront for each beam would create beats in the hologram on the camera. The presence of beats would result in more than one carrier frequency being present and reducing fringe visibility.

A third advantage comes from the use of a polarizing analyzer on the signal path. By introducing a polarizer, any remaining p-polarized light in transmission mode or s-polarized light in reflection mode can be filtered out. As previously discussed in the introduction to interference phenomena, light can only interfere with similarly polarized light. Any perpendicularly polarized light would not interfere and simply act as background noise.

3.4.6 Projector Lens

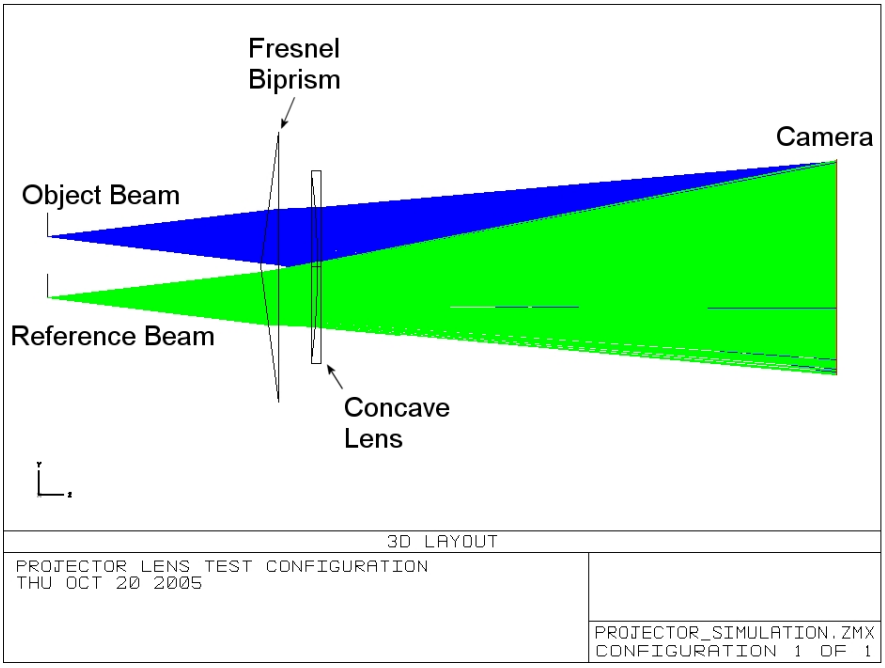

Figure 30: Projector lens configuration illustrates capacity to completely overlap object and reference beam on camera at desired carrier frequency.

In order to completely overlap the object and reference beam and generate a complete fringe pattern a projector lens is necessary. This consists of a shallow angle biprism and a thin concave lens [Figure 30]. The biprism causes the two beams to overlap. The lens is used to magnify the image and fit it onto the camera sensor. Through the combination it is possible to completely overlap both beams and achieve full fill of the camera while maintaining a desired fringe carrier frequency.

The use of a concave lens will introduce wavefront distortion in the form of a concave spherical wavefront to the ideal plane wave interference. However in the physical case, all other lenses in the system are convex which will generate significant convex spherical wavefront distortion as the beam transits the system. The concave lens has a minor corrective effect on the overall wavefront distortion.

3.4.7 Reference Compensator

The introduction of a thick specimen into the focus of the telecentric lens set creates the problem of distortion. If the specimen has a higher index of refraction than the surrounding air then it will decrease the convergence angle of the beam within the specimen. The focal length of the telecentric lens set will lengthen as a result. If the

positions of the lenses in the telecentric set are not adjusted the beam will not be collimated when it exits [Figure 31]. Furthermore the object beam will be heavily phase shifted with respect to the reference beam. An object chief ray traveling through 5 mm of water (n = 1.333) would be phase shifted by 3640λ relative to the reference chief ray.

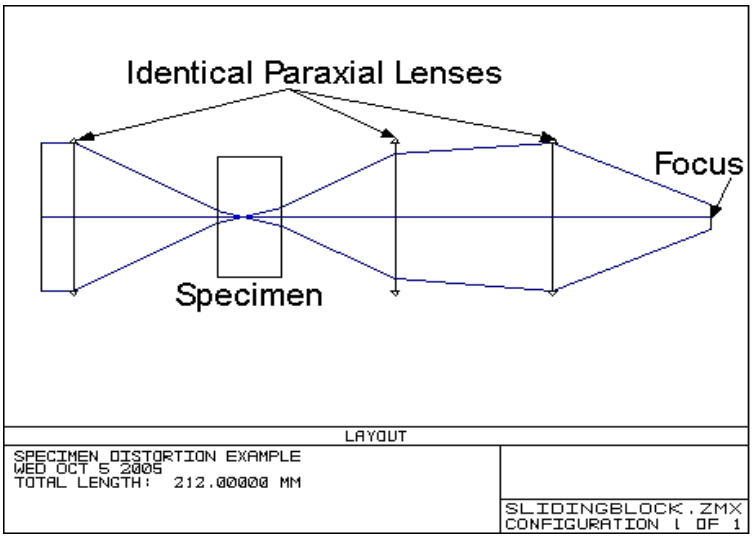

Figure 31: The specimen creates beam distortion in perfect paraxial lens system resulting in a shift in focus point which must be corrected by a compensator.

If the lenses are moved further apart the reference beam will have the opposite problem. The solution is to introduce a *compensator* in the reference beam. The compensator should have the same external dimensions as the specimen and a similar mean index of refraction. For example, if the specimen is a small sample of water with a solution gradient then the compensator would be a sample of water with the same mean molar concentration but fully diffused. In this way the phase shift between the object and reference beam will be much lower and ideally less than 2π.

4.0 Computer Simulation and Analysis

4.1 Overview

By choosing to use a CCD camera to collect holograms it becomes necessary to perform the process of phase and index of refraction reconstruction on a computer. This is accomplished through three steps [Figure 32] performed by three separate program modules:

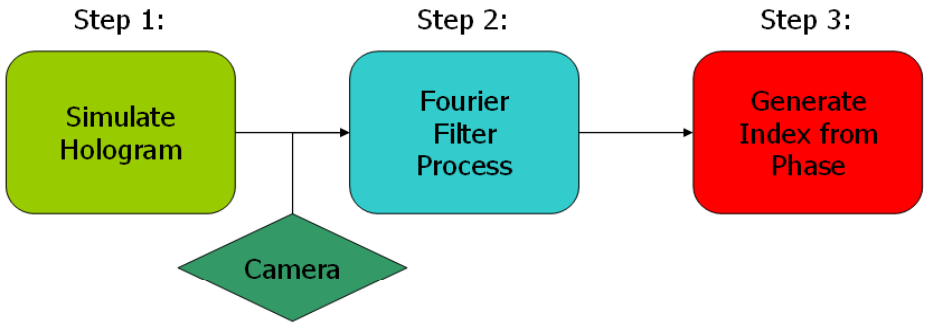

Figure 32: Three step procedure for simulation.

1. Acquisition of a hologram. This can either be done from the camera itself, or a program can simulate a hologram [Figure 33].

Figure 33: Example of 256 Pixel simulated hologram with a carrier frequency of 1/16 fringes per pixel.

2. Fourier filter process. This process strips the carrier frequency off the hologram so that the intensity and phase information can be retrieved.
3. Reconstruction index of refraction from phase information. The phase is an integrated measurement and it must be broken down into local spatial variations in index of refraction.

Ideally all three modules will operate independently of each other. Each module should act as a black box to the other modules. Then the internal methods of one module can be freely changed without affecting the other modules.

4.2 Hologram Simulation

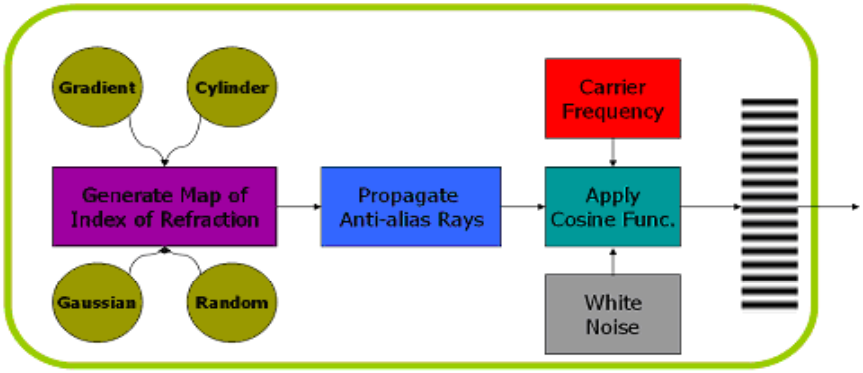

Figure 34: Step 1, simulation of hologram from an arbitrary index of refraction map

Simulation of a hologram is a very computationally intensive process but also very valuable in terms of simulating particular specimens. When using the camera experimentally the exact nature of the specimen is unknown. Thus experimentally characterizing the behaviour of the hologram processing is not practical. With simulation it becomes possible to characterize the error inherent in the algorithms used to process the holograms into localized index of refraction data [Figure 34].

4.2.1 Generate Index Map

In order to simulate a fringe pattern for a given beam profile in a specimen, index of refraction data must be generated. In order to do this, an array of *volume elements* (voxels) is created. Each voxel represents discrete index of refraction value for a given position. The array of voxels is called an *index map* as it is a mapping of the index of refraction. The typical process is to initiate the index of refraction of every voxel to a mean value such as 1.5 – typical for optical glass – and then apply a distribution to create variation in the index map. This distribution can be arbitrary.

The variation in index of refraction caused by the distribution compared to that of the mean must be small – approximately 2-3 % – in order to neglect refraction occurring inside the specimen due to Snell's Law [Kak, 2003].

Some examples are shown in [Figure 35]. This orientation is looking down at the specimen, such that the optical z-axis is from left to right and the perpendicular x-axis is from top to bottom. The origin is taken as the top-left corner.

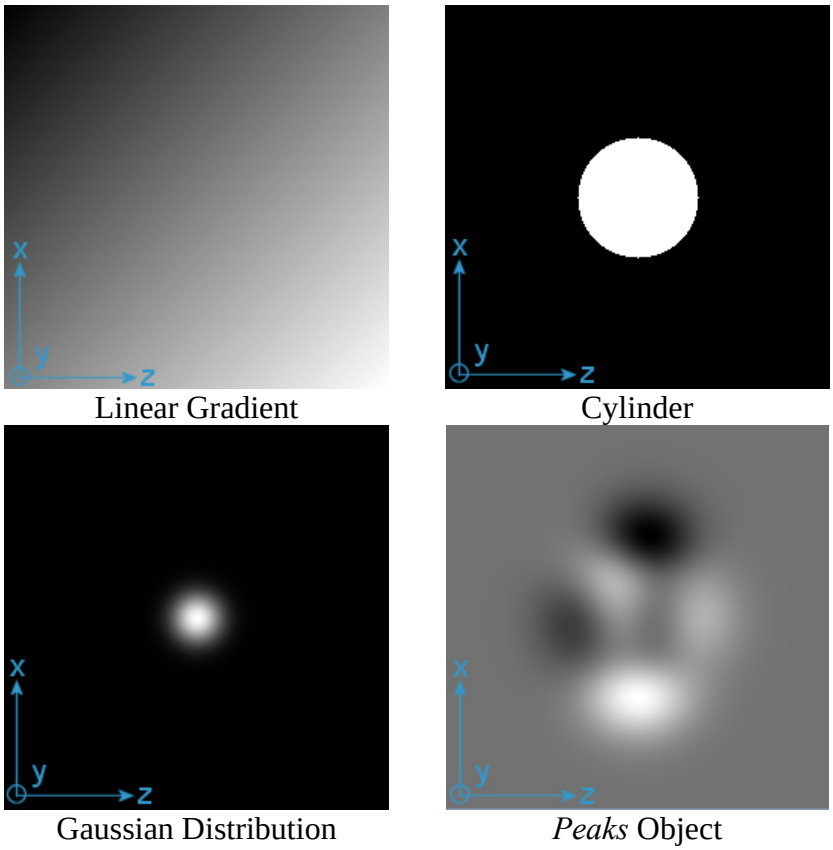

Linear Gradient | Cylinder

Gaussian Distribution | *Peaks* Object

Figure 35: View of two-dimensional top-down index of refraction map examples.

A linear gradient has the form

$$\Delta n(x,z) = Ax + Bz \tag{31}$$

where A and B are some arbitrary constants.

A cylindrical distribution has the form

$$\Delta n(x,z) = \begin{matrix} A, \sqrt{(x-x_o)^2 + (z-z_o)^2} \le r \\ 0, \sqrt{(x-x_o)^2 + (z-z_o)^2} > r \end{matrix} \tag{32}$$

where A is some arbitrary constant and r is the radius of the cylinder.

A normal distribution has the form

$$\Delta n(x,z) = Ae^{-\alpha(x-x_o)^2 - \gamma(z-z_o)^2} \tag{33}$$

where A, α, and γ are arbitrary constants.

The *Peaks* object is collection of normal distributions given by the formula

$$\Delta n(x,z) = 3(1-x)^2 e^{-x^2-(z+1)^2} - 10\left(\frac{x}{5} - x^3 - z^5\right)e^{-x^2-z^2} - \frac{1}{3}e^{-(x+1)^2-z^2}. \quad 34$$

Peaks is suitable for input when a complicated index map is desired to test the algorithms in the software.

4.2.2 Ray Propagation

In order to simulate the phase shift created by the index map a sequence of N rays must be fired through the index map. If the half cone angle of the beam is calculated to be Θ degrees then the software will have to propagate N rays each at an angle

$$\alpha(n) = \Theta - nd\alpha = \Theta\left(1 - \frac{2n}{N}\right) \quad 35$$

to the optical z-axis where n is an integer from one to N. α varies from Θ to -Θ. Then the path length L for a ray at angle α is

$$L = M \cdot d\cos\alpha \quad 36$$

where M is the number of voxels along the z-axis and d is the width of an individual voxel. Since the index of refraction for each voxel differs from the mean by some Δn it is necessary to incrementally propagate each ray from column to column and determine the integrated phase shift.

Since the rays propagate at highly acute angles through discrete voxels alias error is introduced. This alias error is caused by discontinuous jumps from one row to another as the ray is propagated [Figure 36]. This in turn creates step discontinuities in the phase profile in the hologram.

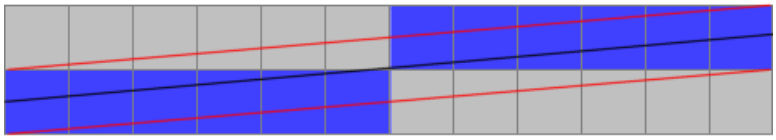

Figure 36: An aliased ray would propagate instep-wise fashion through the dark blue voxels while using an anti-aliasing method calculates contribution of phase from both sets of voxels.

This error can be reduced by introducing an anti-aliasing method. The basis for the method is the same used to draw anti-aliased lines in computer graphics. Instead of

assuming that the ray is infinitesimally narrow, it is given an arbitrary width. A simplifying assumption is to make the width of a ray equal to the width of a voxel. As can be seen from [Figure 36] the narrow black line travels only through the blue voxels. However if a wider beam – taken as the area between the two red lines – is used the voxels located above and below the axis of the ray can contribute to the phase shift. This has a smoothing effect on the phase output.

Because the angles are small it is possible to make the approximation that the area the ray occupies in each row-adjacent voxel is rectangular rather than trapezoidal. This significantly simplifies the math and reduces the computational time. Given a ray with angle α, focused to a point (c_z, c_x) in the sample, the x-axis position of the ray can be defined as

$$x_i = (c_x + c_z \tan\alpha) - i \tan\alpha \qquad 37$$

for the i^{th} voxel column. Define then for the j^{th} row

$$j = \text{floor}(x_i), \qquad 38$$

$$dx_i = x_i - j \qquad 39$$

and the sum phase difference for the ray can be calculated as

$$\phi(\alpha, c_z, c_x) = \frac{L}{M} \sum_{i=0}^{M-1} (1 - dx_i)\Delta n_{i,j} + dx_i \Delta n_{i,j+1}. \qquad 40$$

The process of propagating a very large number of rays through the index map is very time consuming. As such simulations are not capable of producing holograms of the same size of those produced by a camera in a reasonable time frame. The ray propagation step has computational time $O(n^4)$ and generally takes orders of magnitude longer than the entire remainder of the program modules.

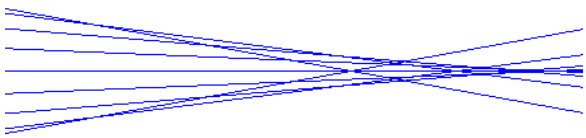

Figure 37: Spherical aberration causes marginal rays to be focused in front of the effective focus position.

Aberrations in the beam are not modeled at this time. Instead the system is assumed to be perfectly focused (i.e. paraxial). Doing so would add considerable complexity to the

software. The effect of beam aberrations is not expected to be deleterious. Spherical aberration will cause the marginal rays to be focused to a point in front of the rest of the ray bundle [Figure 37]. If the defined voxel size is smaller than the beam aberration some of the marginal rays will focus at a voxel in front of the remainder of the beam.

Scattering and absorption are also not modeled at this time. As a result the intensity measurement will not contain any information. By including a coefficient of scattering, coefficient of absorption, and anisotropic scattering factor for each voxel it would be possible to simulate intensity variation.

4.2.3 Phase Profile

The sequence of phase shifts over successive small angles incrementally separated by $d\alpha$ for a convergent beam is called the *phase profile*. If the angle $d\alpha$ becomes infinitesimally small we can consider the profile a continuous function $\phi(\alpha)$. Functionally, every scan position (c_z, c_x) has an associated phase profile [Figure 38]. Because a line-scan camera is used each pixel x on the camera is associated with a given angle α.

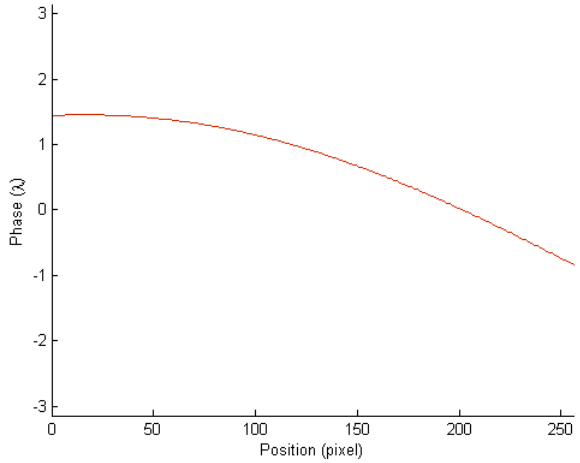

Figure 38: Example of phase profile from *Peaks* object

The curvature of the phase profile may contain useful information to determine the shape or morphology of the index map being sampled. For example when the beam is passing through the centre of a Gaussian perturbation in the index map it tends to peak in the centre and drop off to either side. Most of the morphology information is contained

in the derivative of the phase profile. The derivative of the profile is the rate of change of phase shift over successive angles.

The profile may be projected onto a flat surface such as a camera sensor in which case it becomes a function of pixel position *n*. As a convention in the software the phase profile is presented as a discrete array $\phi(n)$ where *n* is the number of pixels of the camera.

4.2.4 Fringe Generation

The fringes generated by the simulation should have the same format as the camera output. This allows the filter program module(s) to accept data from either the simulation or the camera without the need to specify the source. Hence the output should have the same number of pixels and pixel depth as the camera. This necessitates that the irradiance take discrete values, i.e. digital numbers. The digital irradiance as a function of pixel position can be defined as

$$I_D(n) = \cos^2\left(2\pi n f_c(n) + \phi(n)\right) + N_{white}(r) \qquad 41$$

where I_D is the discrete irradiance (0-255 for 8-bit pixel depth), f_c is the carrier frequency, *n* is the pixel position, ϕ is the calculated phase shift from [Equation 37], *N* is the noise function, and *r* is the maximum electronic noise observed on the camera. If the carrier frequency f_c is constant then the resulting interference pattern will be plane parallel fringes. The carrier frequency can vary as a function of pixel position if the reference and object beams have different path lengths.

The camera purchased for the microscope is a Dalsa Piranha 2. It is line-scan camera with 8192 pixels and can output in either 8-bit or 10-bit mode. At nominal gain the noise is specified as four digital numbers by the manufacturer. For computational speed most simulated fringe patterns are only calculated with 256 pixels.

4.3 Fourier Hologram Filtration

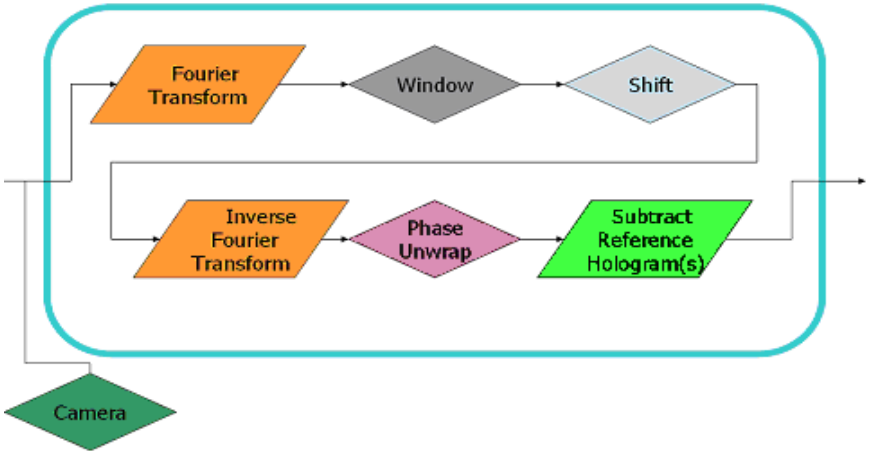

Figure 39: Step 2, the Fourier filter analysis to retrieve phase measurement from hologram.

The most common way to retrieve the complex irradiance signal from a hologram is by means of applying a Fourier transform and then filtering the signal in frequency space [Volkl, 1999 and Lehmann, 2002]. This technique allows the carrier frequency of the fringe pattern to be removed. In order to retrieve the phase it is further necessary to check if the phase has wrapped (shifted over 2π) and subtract the contribution to the signal induced by the optics. This process is accomplished over a number of sequential steps [Figure 39].

4.3.1 Discrete Fourier Transform

Given data sampled in time or space, we can construct a finite data sequence $x(n)$ of length N. In most literature the Fourier transform is used on temporal-sampled data from an analog electronic signal. For holography data is spatial-sampled from a hologram recorded by a CCD camera. By taking advantage of the periodicity of the imaginary exponential function e^{iz} we can create a function known as the Fourier transform. Given the irradiance vector $\mathbf{I}(n)$ the discrete Fourier transform

$$\mathbf{I}(k) = \sum_{n=0}^{N-1} \mathbf{I}(n) e^{-jnk(2\pi/N)} \qquad 42$$

generates a corresponding sequence of data **I***(k)* in frequency-space. The Fourier transform is extremely useful because the sequence **I***(k)* represents the periodicities in the input data and the relative contributions of any one frequency *k*.

Similarly, there exists an inverse discrete Fourier transform,

$$\mathbf{I}(n) = \frac{1}{N}\sum_{k=0}^{N-1}\mathbf{I}(k)e^{jnk(2\pi/N)} \qquad 43$$

that allows us to transform from frequency back to space (or time).

Computationally it is inefficient to apply the Fourier transform as given above. A much faster method known as the *fast Fourier transform*, commonly abbreviated FFT, was developed in the 1950s [Press, 1992]. The FFT algorithm operates fastest on data sets that are of size 2^N, N = 1,2,3,…

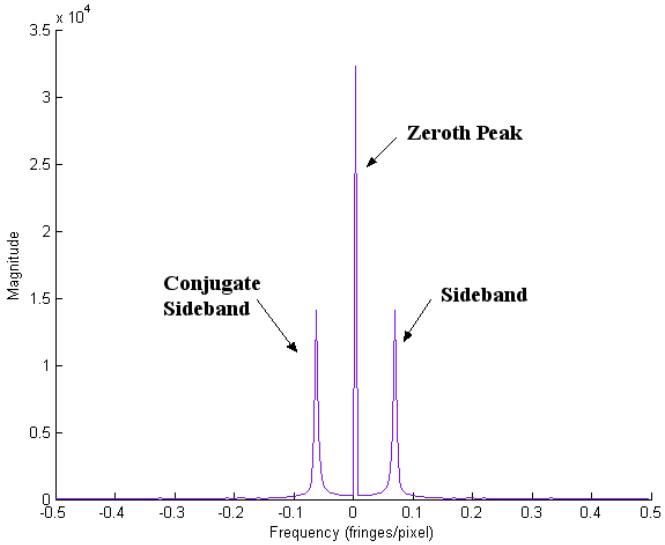

Figure 40: The hologram magnitude in Fourier space shows zeroth peak along with two sidebands in real and conjugate frequency space.

The result of the Fourier transform is symmetric in frequency space and conjugate frequency space [Figure 40]. The units of the magnitude of the complex irradiance in frequency space are not meaningful but the square of the magnitude is the power. The zeroth peak is found at zero frequency and corresponds with the equivalent of the direct current component of the signal. The sidebands contain the information of the hologram. They are located at the carrier frequency of the interference fringes. There may be

additional sidebands at other frequencies but they are usually very small in magnitude and hence neglected.

4.3.2 Apodization Function

An apodization function (also called a tapering function) is used to separate the 1st sideband in frequency-space from the zeroth peak [Weisstein, 2005a]. An ideal apodization function will smoothly filter the edges of a window down to zero, as well as the 1st and 2nd derivatives. There are a variety of apodization functions available such as the Bartlett window, Blackman window, Hamming window, and Hanning window. The Hanning window is the function,

$$\mathrm{H_A}(k) = \cos^2\left(\frac{\pi(k-k_o)}{2a}\right) \qquad 44$$

where a is the half-width of the Hanning window and k_o the center position. The Hanning window has the best performance of the known apodization functions without biasing the amplitude of the output.

The Hanning window is applied by multiplying it by the complex irradiance in frequency space,

$$\mathbf{I}_{win}(k) = \mathbf{I}(k)\cdot \mathrm{H_A}(k). \qquad 45$$

If the width and centre point of the Hanning window are properly chosen the sideband should be separated from the zero[th] peak. All positions outside the Hanning window (including the conjugate sideband) are forced to zero. In conjunction with a shift of the sideband, the carrier frequency of the interference fringes can be filtered out, leaving only the complex irradiance and the desired phase shift. The centre point of the sideband k_o and width of the apodization function a can be expressed as:

$$k_o = Mf_c, \qquad 46$$

$$a = wMf_c \qquad 47$$

where M is the data sequence length and f_c is the carrier frequency. The variable w is an arbitrary constant between zero and one. Empirically a value of $w = 2/3$ has been found to work well. Smaller values for w lead to greater instrumentation error from the apodization function while increasing w towards one begins to incorporate spurious

information from the zeroth peak inside the filtering window. If f_c is overly small the zeroth peak and sidebands may overlap and alias.

The Fourier transform of the Hanning function is known as its instrumentation function, $H_I(k)$. The instrumentation function can be expressed analytically as

$$H_I(n) = \frac{a\,\mathrm{sinc}(2\pi an)}{1-4a^2n^2} \qquad 48$$

where sinc(x) is the *cardinal sine* described by the function sin(x)/ x and unity when x = 0. The instrumentation function generates a form of alias error with the signal. In order to avoid confusion this form of aliasing will be termed the *instrumentation error*. This instrumentation error corrupts the beam complex irradiance profile that results from the hologram through the Fourier-filtration process.

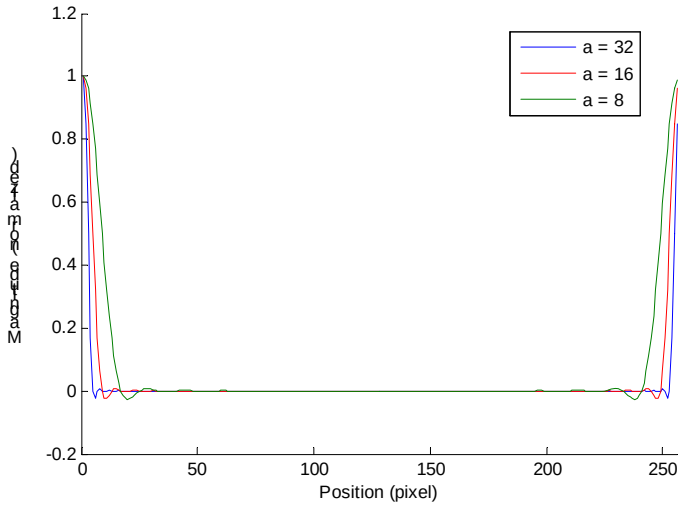

Figure 41: The Hanning instrumentation function for various window widths Demonstrates decreases width of instrument function with increased width *a* of Hanning function.

The width of the instrument error depends on the width of the window [Figure 41]. The Hanning instrument function goes to zero at approximately M/a = 5/4. Hence for a window sixteen pixels wide, the instrument error will be approximately twenty pixels wide from both edges of the phase profile [Figure 42].

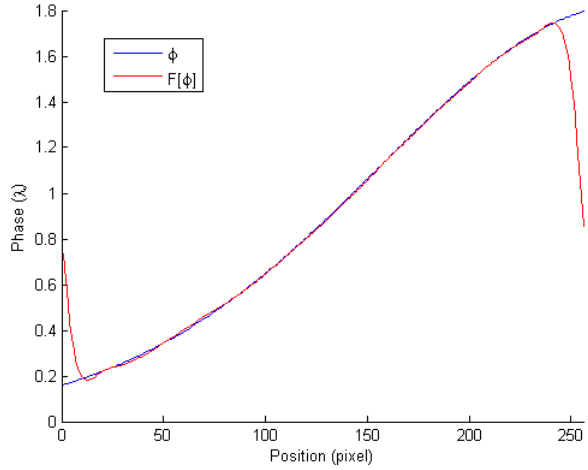

Figure 42: A comparison of the simulated phase profile (blue) versus the Fourier-filtered phase profile (red) shows the effect of instrument error on the edges of the phase profile.

Analytically the instrument error is caused by the fact that the Hanning instrument function and the inverse Fourier transformed vector irradiance are convolved as

$$\Im^{-1}\{\mathrm{H}_A(k)\cdot\mathbf{I}(k)\}=\mathrm{H}_\mathrm{I}(x)\otimes\Im^{-1}\{\mathbf{I}(k)\}. \qquad 49$$

Since the instrumentation function H_I is known it may be possible to deconvolve the two functions. The most common method known for deconvolution is the *Weiner filter* [Weiner, 1964]. The presence of noise from the electronics may make known deconvolution methods ill-posed.

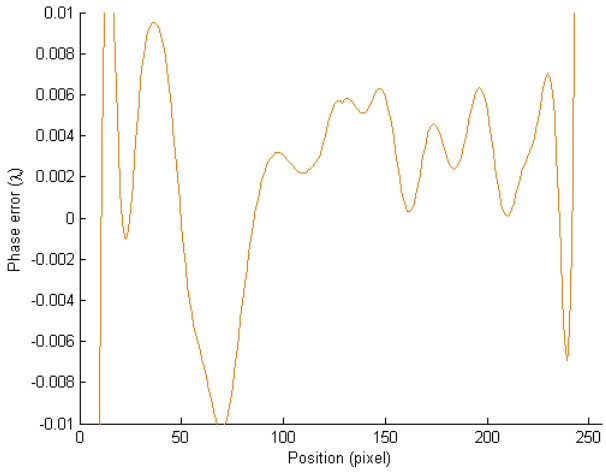

Figure 43: The phase error outside instrument aliased regions is small (< 0.01 λ) comes from simulated electronic noise.

It can be seen from [Figure 43] that the error between the input phase shift and the Fourier filtered phase shift is less than 0.01λ away from the regions contaminated by instrumentation error. Almost all of the phase error outside of the instrumentation error regions is caused by the simulated white noise of the camera. By discarding the data contaminated by the instrument error highly accurate complex irradiance can be resolved from the original hologram. Unfortunately the data lost represent the most marginal rays in the convergence beam. This effectively reduces the half-cone angle of the beam and with it the optical axis resolution.

4.3.3 Sideband Shift

In order to recover the complex irradiance from the sideband it is necessary to shift it to the zero frequency position. This places the signal components in both the frequency and conjugate frequency domain. As a result upon applying the inverse Fourier transform the result will be the complex irradiance rather than the original purely real irradiance of the hologram. While conceptually treated as separate, computationally the sideband is shifted simultaneously with the application of the Hanning window.

If the fringe spatial wavelength ($1/f_c$) is an integer then the shift is simply a matter of interchanging array positions. Unfortunately this is generally not the case. Instead it is necessary to rotate the coordinate frame in complex space by an angle πf_c using a rotational matrix:

$$\begin{bmatrix} \mathrm{Re}(I') \\ \mathrm{Im}(I') \end{bmatrix} = \begin{bmatrix} \cos(\pi f_c) & \sin(\pi f_c) \\ -\sin(\pi f_c) & \cos(\pi f_c) \end{bmatrix} \begin{bmatrix} \mathrm{Re}(I) \\ \mathrm{Im}(I) \end{bmatrix}. \qquad 50$$

In practice one shifts the array elements of the complex irradiance by the integer floor of the spatial wavelength and then applies a small rotation over the remainder to correct the result.

The carrier frequency can be found by counting the number of fringes (maxima and minima) over the width of the camera.

$$f_c = \frac{(n_{\max} + n_{\min})/2}{M} \qquad 51$$

where n_{max} is the number of maxima, n_{min} is the number of minima, and M is the width in pixels of the camera. The statistical error for this method is quite small. For example, for

a real spatial frequency f_c = 1/17.5 fringes/pixel and M = 8192 pixels the maximum error for f_c is only 0.15 %.

4.3.4 Phase Unwrapping

One unique aspect of the phase measurement is that it is relative to a reference and cyclic. This is because the phase is derived from the arctangent of the complex irradiance **I**, such that

$$\phi = \arg(\mathbf{I}) = \tan^{-1}\left(\frac{\mathrm{Im}(\mathbf{I})}{\mathrm{Re}(\mathbf{I})}\right). \qquad 52$$

The arctangent normally has bounds (-π/2,π/2], but the computer function *atan2* actually varies from (-π,π]. It does this by taking the real and imaginary components of the complex amplitude as separate input arguments. As a result, it can determine the quadrant of the result based on the sign of each of the arguments.

However, even with doubling the range through the use of *atan2,* it is still possible that the phase shift from one side to the other of the beam profile will be greater than 2π. In this case, there will be an unwanted discontinuity in the data [Figure 44]. The discontinuity can be removed by an iterative process known as phase unwrapping.

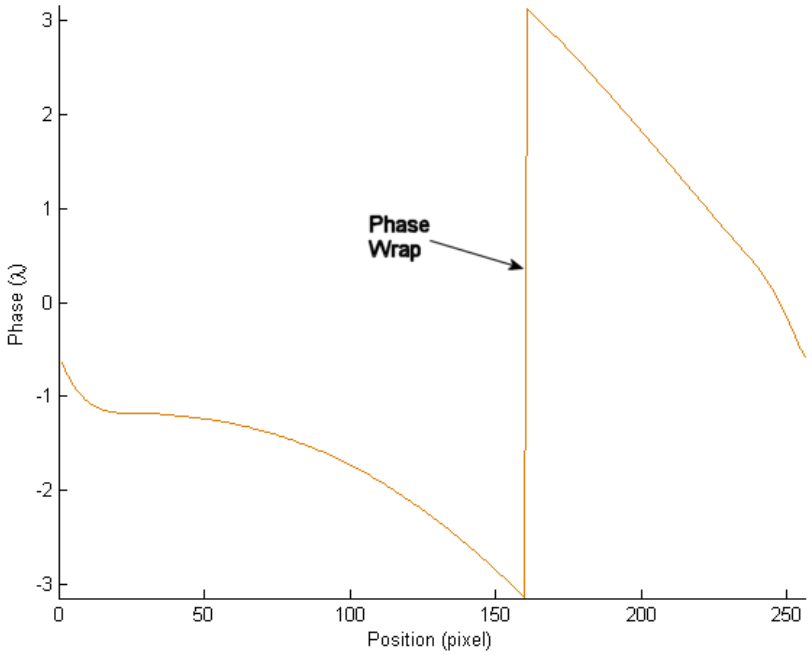

Figure 44: An example of phase wrapping demonstrates how phase is a periodic function with range (-π,π].

The simplest method for phase unwrapping is to compare the result for every adjacent scanning position. If the phase between two points varies by more that π we assume that the phase has wrapped and apply an artificial shift of 2π to the neighbour and each successive phase in the profile. If the phase shift between successive scan steps is actually greater than π this method can fail. In this case it is best to increase the frequency of scan positions so that each individual step has a smaller phase shift.

The ideal location to pick as a reference to unwrap for each voxel's phase profile is the centre point. The centre of the phase profile is representative of the phase shift of the chief ray. If the centre is chosen as the start position for unwrapping, the phase with respect to other voxels in the row is guaranteed to be continuous.

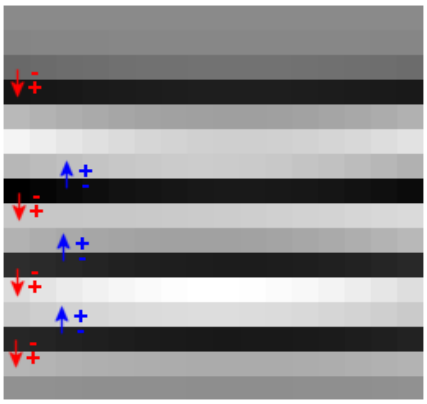

Figure 45: Column-wise phase wrapping at 16 x 16 voxels in *Peaks* specimen.

Once the phase for each profile has been unwrapped, another step is necessary. The phase of each row must be unwrapped column-wise with that of its neighbouring rows [Figure 45]. The process is mathematically similar.

4.3.5 Reference Hologram

One of the benefits of performing hologram analysis with a computer is that the influence of the optical components can be recorded and then removed from the phase information. This is done by recording a reference hologram with no specimen present. The resulting interference fringes will not have zero phase shift across its breadth, but rather some waves of shift from the aberrations introduced by the optical components. For the wavefront-split confocal holograph, spherical aberration, coma, and distortion contribute to the wavefront error.

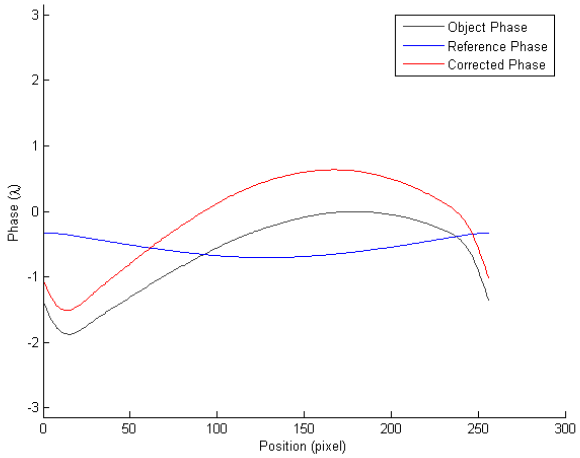

Figure 46: Reference phase is subtracted from object phase to provide phase corrected by contributions of optical components.

The reference phase profile is subtracted from the object phase profile to provide a corrected phase profile measurement [Figure 46]. In this way all the optical aberrations of the system can be removed. For the sample scan prototype only a single reference hologram needs to be recorded. For the beam scan system a reference hologram must be taken for each scan position. The optical aberrations will change as the beam rasters over the optical surfaces. In particular coma will shift dramatically.

4.4 Index of Refraction Reconstruction

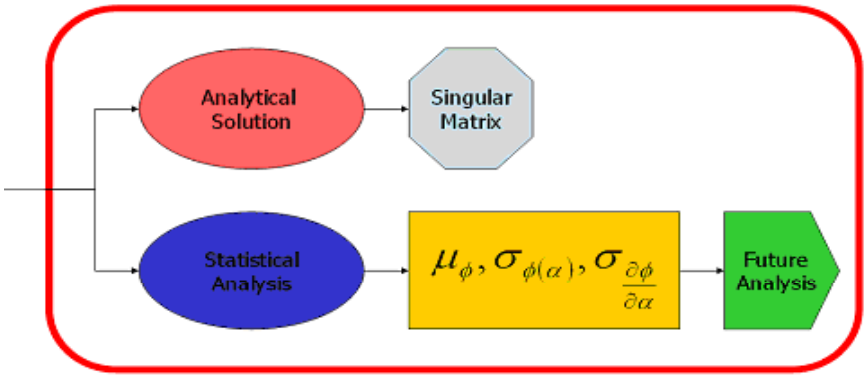

Figure 47: Step 3, reconstruction of index of refraction from phase measurement

Once the phase profile for each voxel has been recovered it is not a trivial process to reconstruct the index of refraction for each individual voxel. The phase measured in the profile is the integrated phase shift for a ray as it travels through the specimen. However, we want to determine the specific phase shift $\Delta\phi$ over a given voxel. There are a number of possible solutions: analytic solution, tomographic reconstruction algorithms, incremental correction from the boundary conditions, and statistical analysis [Figure 47].

4.4.1 Analytical Solution

The most obvious method is to try to solve the index of refraction analytically using Gaussian elimination. This involves assembling a matrix that maps every ray and the voxels they travel through the object to its associated phase shift value. The matrix-vector equation takes the form

$$\begin{bmatrix} \Delta n_{00} & \Delta n_{01} & \dots \\ \Delta n_{10} & \Delta n_{11} & \dots \\ \dots & \dots & \dots \end{bmatrix} \begin{bmatrix} \mathbf{r}_1(\alpha) \\ \mathbf{r}_2(\alpha) \\ \dots \end{bmatrix} = \begin{bmatrix} \phi_1(\alpha) \\ \phi_2(\alpha) \\ \dots \end{bmatrix}. \qquad 53$$

A third dimension for α is not depicted.

This method fails because the resulting matrix is extremely sparse. Each ray traverses only a small number of voxels in the index map. Due to sparseness the matrix is singular and cannot be inverted. Gaussian elimination requires the matrix be invertible to find a solution.

4.4.2 Tomography Algorithms

There are several methods used in tomography to perform 3-dimensional reconstruction. Since physically the full cone angle Θ_C of a confocal holography beam is equivalent to the sweep Θ_T in a tomographic system the degree of information collected via triangulation is identical for a given angle.

The ability of tomographic reconstruction to reconstruct an accurate 3-dimensional representation of an object is dependant on the span covered in **k**-space (i.e. frequency space) [Kak, 3.6, 1999]. This is known as the Fourier slice theorem. In order to be able to completely define an object the sweep angles α must cover the span from $\pi/2$ to $-\pi/2$.

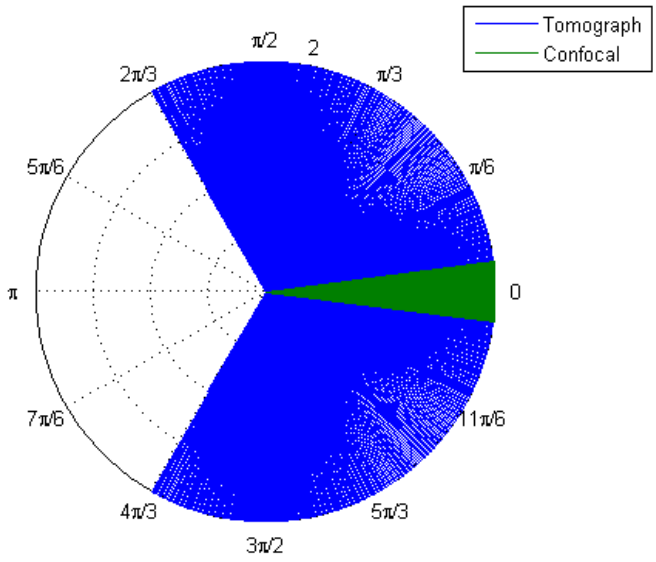

Figure 48: A k-space plot shows the small frequency space span of confocal holography compared to complete span by tomography with many projections.

Tomographic algorithms typically take a slightly wider span from 2π/3 to -2π/3 in order to guarantee complete coverage in the case of diffraction in the specimen. The results are very accurate and work for general cases. However when limited to the much more narrow sweep angles of confocal holography (12 - 20°) tomographic algorithms break down and exhibit a phenomenon known as *streaking*. The polar plot [Figure 48] shows how small the **k**-space coverage of a confocal beam is compared to tomography.

The conclusion is that we cannot apply tomographic algorithms designed to work in the general case to confocal holography. Instead we must know something about the morphology of the specimen and develop algorithms for reconstruction of special cases.

4.4.3 Incremental Correction Algorithm

A method to solve for the index of refraction where the variation is an independent function in each dimension such that

$$n(x,y,z) = f(x) + g(y) + h(z) \qquad 54$$

has been developed [Lai, 2005]. This method is suitable for the linear gradient [Figure 49, 50, 51] and also the cylindrical distribution (not shown).

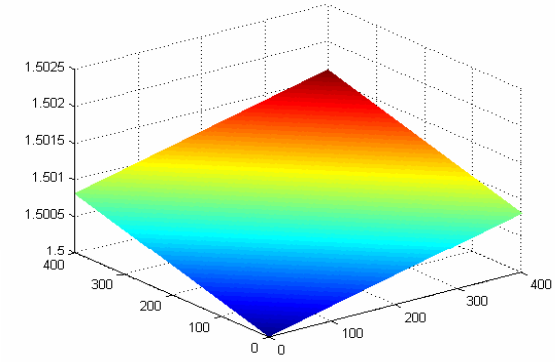

Figure 49: Source linear gradient index of refraction map [Lai, 2005].

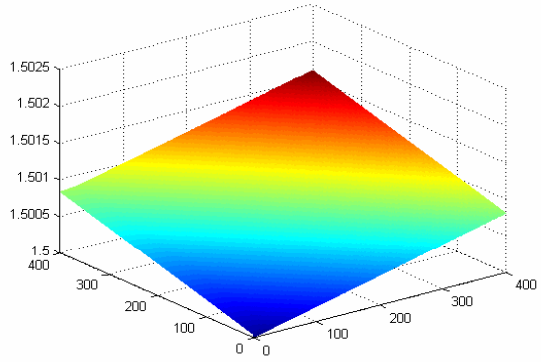

Figure 50: Incremental corrected result of linear gradient [Lai, 2005].

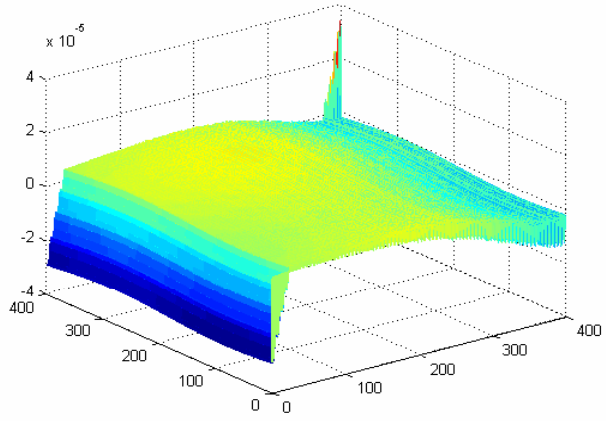

Figure 51: The calculated difference (error) between the source and resulting index of refraction maps[Lai, 2005].

The method of incremental correction is not suitable for a Gaussian distribution or other functions with dependant variables. There is still a need to develop special methods for other distributions that are superior to standard tomography methods in order to reduce artifacts and improve resolution along the optical axis.

4.4.4 Statistical Moments

Visual observation of the beam phase profile reveals that it is not uniform and depending on the position of the focus the shape of the curve changes. This suggests another possible solution to establish the local phase shift and index of refraction in three

dimensions. Descriptive statistics, such as the mean and variance, might be used to develop a heuristic method to find a solution for the index of refraction. Descriptive statistics are based around the concept of statistical moments.

The n[th] statistical *raw moment* for a data sequence x is defined as

$$\mu_n' = \left\langle x^n \right\rangle = \int x^n \, \mathrm{P}(x) dx \qquad 55$$

for some n = 1,2,3,4,… P(x) is the probability density function, e.g. the probability of x being sampled at a given point. The best known raw moment is the mean, μ_1', which is often simply denoted μ.

The n[th] statistical *central moment* is defined as

$$\mu_n = \left\langle \left(x - \langle x \rangle \right)^n \right\rangle = \int (x - \mu)^n \, \mathrm{P}(x) dx \qquad 56$$

[Weisstein, 2005b]. The second central moment μ_2 is the variance. The central moment is computationally expensive to calculate, but it is possible to define the first few central moments in terms of the raw moments,

$$\mu_1 = 0, \qquad 57$$

$$\mu_2 = -\mu_1'^2 + \mu_2', \qquad 58$$

$$\mu_3 = 2\mu_1'^3 - 3\mu_1'\mu_2' + \mu_3', \qquad 59$$

$$\mu_4 = -3\mu_1'^4 + 6\mu_1'^2\mu_2' - 4\mu_1'\mu_3' + \mu_4' \qquad 60$$

[Weisstein, 2005b]. There 3[rd] and 4[th] central moments are also used in descriptive statistics to define two parameters, the *skewness* and the *kurtosis*.

Skewness is a measure of the symmetry of a distribution. A normal (Gaussian) distribution has zero skewness. A distribution with a larger proportional distribution to the left (in negative space) would have negative skewness. Similarly a distribution with larger distribution to the right would have positive skewness. The skewness is defined as

$$\gamma_1 = \frac{\mu_3}{\mu_2^{3/2}} \qquad 61$$

[Weisstein, 2005b]. It is essentially the 3rd central moment normalized by the variance. Because the variance of the beam profile can easily be zero we will from now on consider the skewness and 3rd central moment synonyms. Otherwise the statistical analysis has a tendency to calculate the skewness of a voxel's phase profile as being infinity.

The kurtosis is similarly defined as

$$\gamma_2 = \frac{\mu_4}{\mu_2^2} - 3 \qquad 62$$

or more properly called the *kurtosis excess* with the minus three term [Weisstein, 2005b]. The kurtosis is a measure of the peakness of a distribution. A normal distribution has a kurtosis of three or a kurtosis excess of $\gamma_2 = 0$. A distribution with a steep peak has $\gamma_2 > 0$ whereas a flatter peak has $\gamma_2 < 0$. Again because of the presence of the variance as a normalizing factor in the denominator, we will ignore it and define the kurtosis as the 4th central moment from now on.

4.4.5 Numerical Differentiation

Another possible source of information to exploit for a statistical heuristic method is to calculate the descriptive statistics of the 1st and 2nd derivatives of the phase profile. Numerical derivatives can be calculated by using a difference equation. The accuracy of the difference equations can be very high if several points are used. For this project, a five-point formula was used [Burden, 1997]:

$$f'(x_0) = \frac{1}{12h}\left[f(x_0 - 2h) - 8f(x_0 - h) + 8f(x_0 + h) - f(x_0 + 2h)\right] + \frac{h^4}{30} f^{(5)}(\xi) \qquad 63$$

with h being the step size. On a computer h is always one array element. The last term is the error function for ξ lying between x_o and $x_o + 4h$. The error is very small due to the fifth order derivative.

This function is suitable for differentiating in the middle of the beam profile but not on the end-points for either side. For the end-points, a different function is used:

$$f'(x_0)=\frac{1}{12h}\begin{bmatrix}-25f(x_0)+48f(x_0+h)-36f(x_0+2h)\\+16f(x_0+3h)-3f(x_0+4h)\end{bmatrix}+\frac{h^4}{5}f^{(5)}(\xi). \qquad 64$$

The error of the end-point method is six times higher than that of the midpoint method.

4.4.6 Graphical Representation

The statistical moments of the phase can be represented graphically. The particular moment of the phase profile of each voxel is computed and auto-scaled in grey. The base measurement is taken to be the mean phase shift. By observation the statistical moments that appear to be significant are the phase variance, the variance of the 1st derivative of the phase, and the kurtosis of the phase [Figure 52].

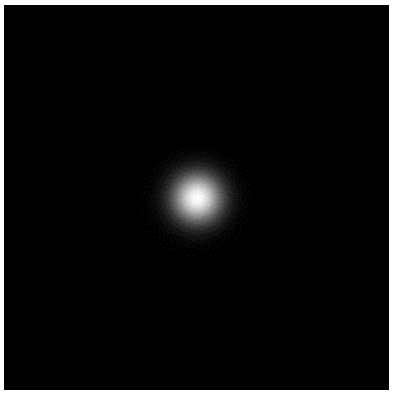

Original Index Map

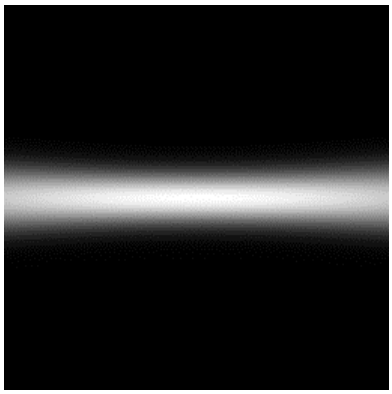

Mean Phase

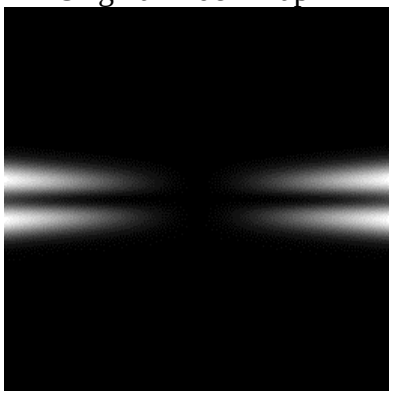

Phase Variance

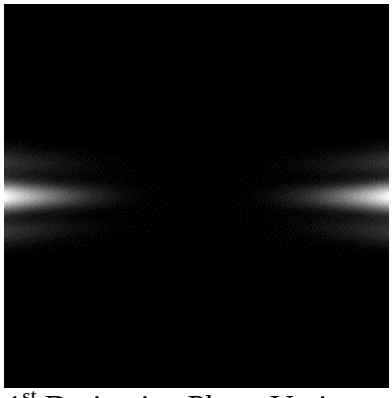

1st Derivative Phase Variance

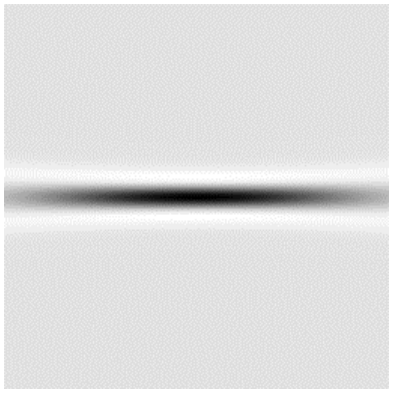

Phase Kurtosis

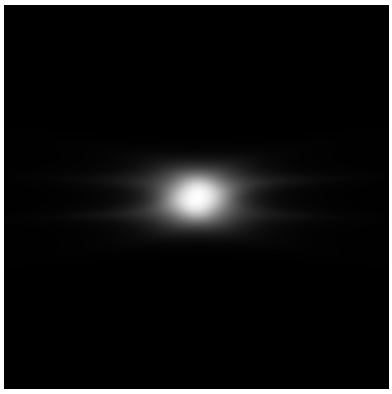

Normalized Mean

Figure 52: Graphical representation of phase statistical moments.

If the mean is divided by the sum of the two variance distributions the result looks similar to the original index map. This normalization does not represent an equivalent to $\Delta\phi$. However the morphology is encouraging as it does suggest that descriptive statistics may be a successful route to determining the 3-dimensional index of refraction.

Table 6: Statistical Moment Extrema for Gaussian Index Map

Moment	Maximum	Minimum
Variance	0.21	0.0
1st Derivative Variance	$5.7 \cdot 10^{-5}$	0.0
Kurtosis	1.4	-12

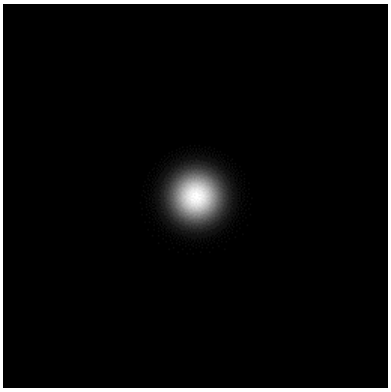

Original Gaussian Index Map

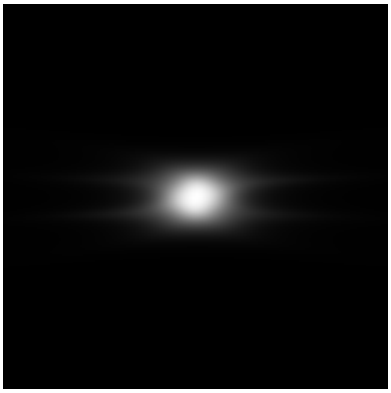

Gaussian Statistically Normalized Result

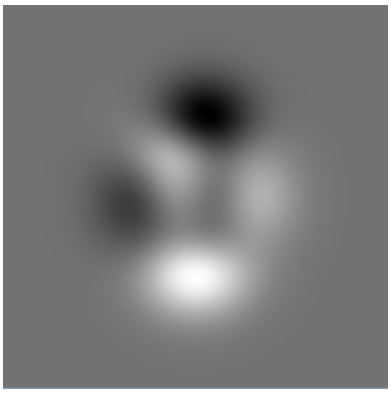

Original *Peaks* Index Map

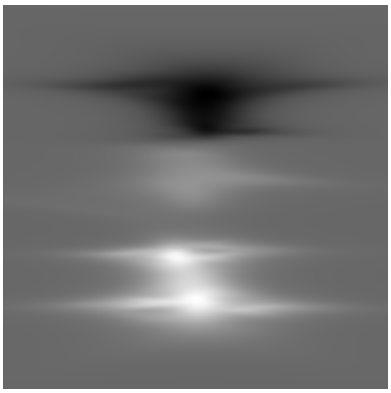

Peaks Statistically Normalized Result

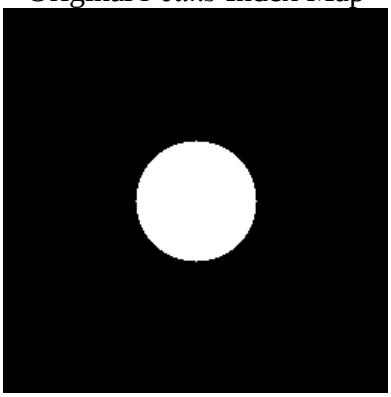

Original Disk Index Map

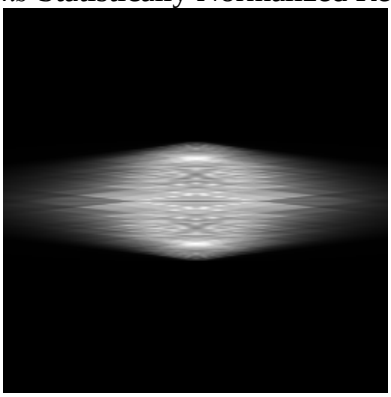

Disk Statistically Normalized Result

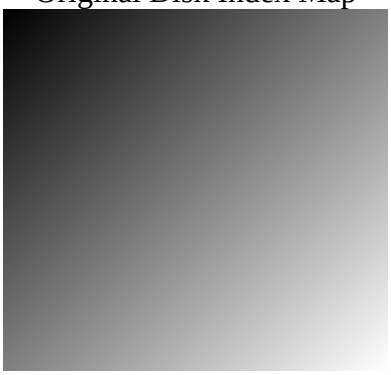

Original Linear Gradient Index Map

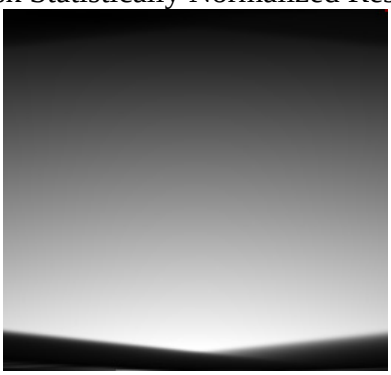

Gradient Statistically Normalized Result

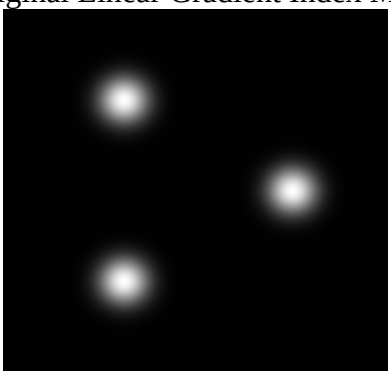

Original Tri-gaussian Index Map

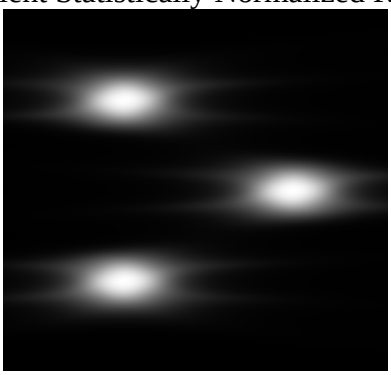

Tri-gaussian Statistically Normalized Result

Figure 53: Side-by-side comparison of original index of refraction maps and their statistically normalized results.

By examining a side-by-side comparison of a number of index maps compared to their statistically normalized results [Figure 53] an impression of the efficacy of the method for said distributions. For simple Gaussian distributions the results are promising. For more complicated objects, such as *Peaks*, the result is more difficult to interpret. For the linear gradient the method fails.

4.4.7 Heuristic Approach to a Solution

The variance, variance of the derivative, and kurtosis all contain what appears to be useful information regarding the variation in index of refraction. One is naturally led to question whether this information can be used to develop some algorithm to provide a better estimate of the index of refraction than the sample mean. There has been some recent interest in the potential for using statistics for tomographic reconstruction in electron microscopy [Sorzano, 2005] as well as positron emission tomography [Browne, 1996]. However the methods presented are not directly applicable.

If we return to the original estimator function

$$\mathrm{E}[\Delta\phi] = \sum_{x=0}^{N-1} \Delta\phi(x)\mathrm{P}(\Delta\phi) \qquad 65$$

we notice that for the sample mean the function $\mathrm{P}(\Delta\phi)$ is a constant, namely $1/N$. In other words each ray in the phase profile has the same weight. It is plainly not true to state that the each ray is equally likely to predict the correct phase shift. Therefore the sample mean does not represent an accurate $\Delta\phi$ for a voxel. This can be seen from the graphical representation of the mean phase compared to the original index map: the two are not comparable.

Instead of taking the probability density function as being constant we can develop a heuristic method that takes into account the apparent reliability or confidence of each ray segment in the phase profile. The only condition is that $\mathrm{P}(\Delta\phi)$ must sum to unity over N.

One possible method to compute the confidence of a given ray would be to sum the variance of each voxel it passes over. A ray with a path that extends through a region of space with little variation in index of refraction should have a low variance sum which is

to say a high confidence. Then the ϕ for that ray segment, divided by the length of the ray, should provide a reliable estimator for $\Delta\phi$ of voxels lying along the ray.

Computing the variance sum of every ray for the phase profile of every voxel would be computational expensive. It should suffice to sample a small number of rays (less than ten) through the phase profile and then interpolate to derive P($\Delta\phi$). The simplest interpolation method would be to create a linear piece-wise probability density function [Figure 54]. This could be improved by using interpolation techniques such as cubic splines or quadrature methods to produce a smoother function.

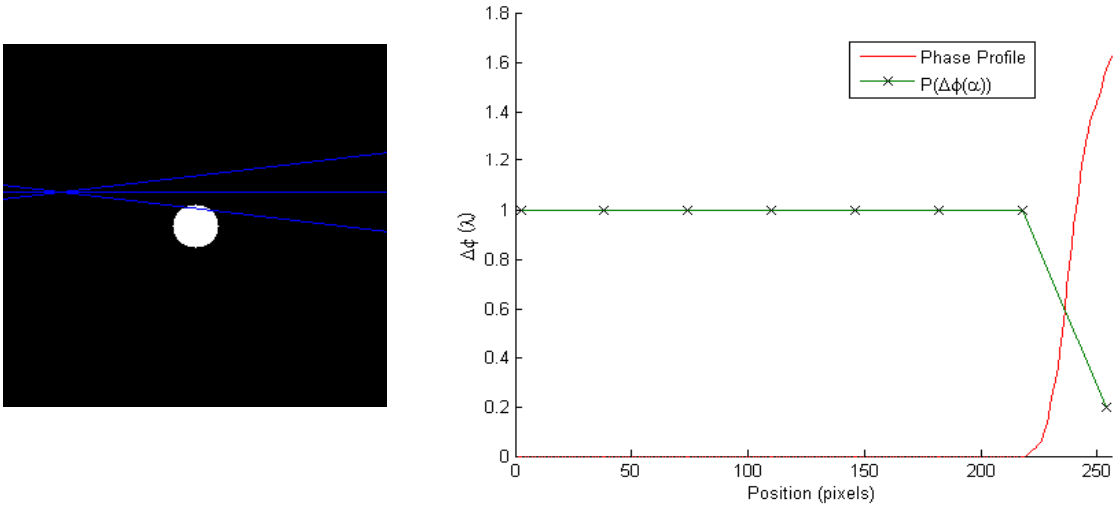

Figure 54: Piece-wise probability density function for phase profile shows how variance increases on the edge that passes through the disk object

The index of refraction would be determined first for voxels with sampled rays segments that have a high confidence, i.e. flat phase profiles with zero kurtosis. This would provide boundary conditions for as of yet undetermined voxel positions. In an incremental heuristic manner the voxels with increasing variance and kurtosis could be estimated in turn until a complete index map is developed. Each successive step would deliver a high confidence $\Delta\phi$ datum for individual voxels which in turn can be used to modify the probability density function for adjacent voxels.

4.5 Software Package

The steps outlined in the computer simulation and analysis was implemented as a software package in Visual Basic .NET. Visual Basic was chosen as a programming language due to the ease of creating a user interface and displaying graphical output.

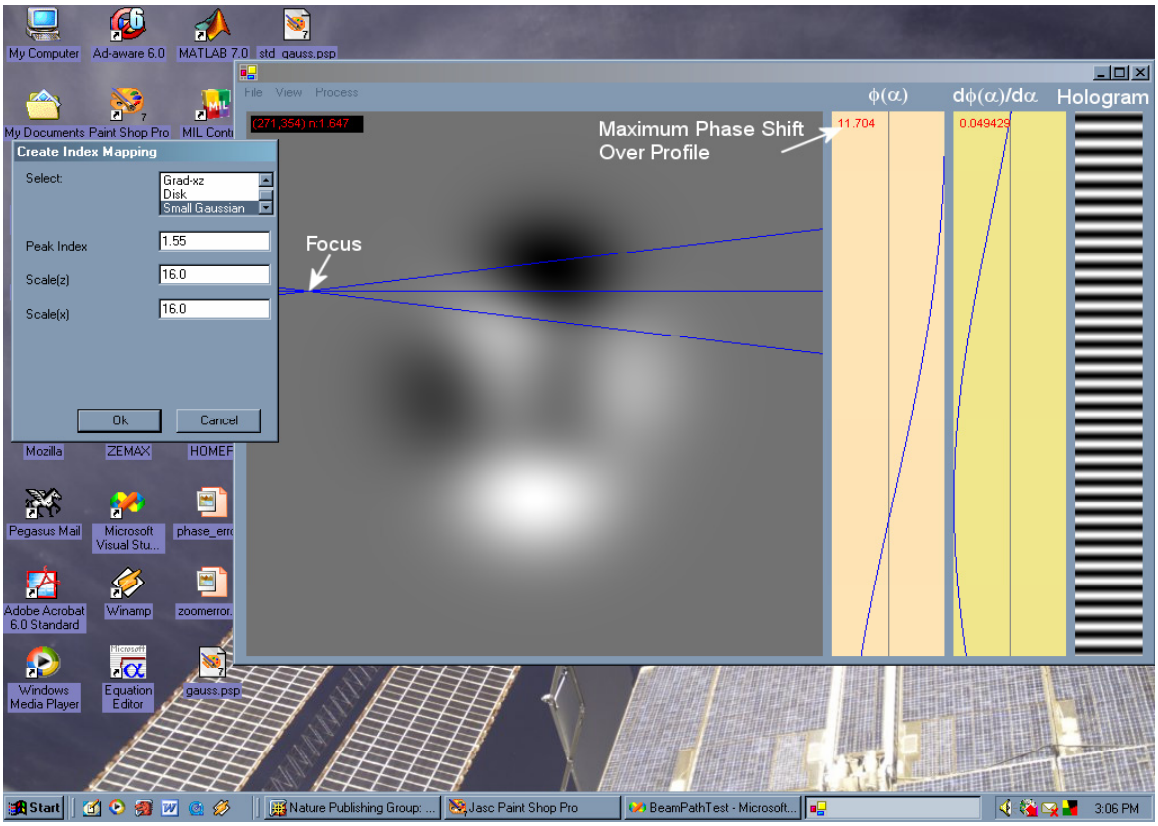

Figure 55: This screenshot of software package shows the index map (middle) with beam focus position set by the user and an associated phase profile, derivative of the phase profile, and simulated hologram on right-hand side.

The software package is designed to help the user to explore the mechanics of confocal holography and better understand how it operates. As such it is capable of producing a wide variety of graphical outputs [Figure 55]. The main window (top-left) displays the index map along with a convergent beam that can be moved about with the mouse. As the focus is shifted through the index map the phase profile and hologram are dynamically updated on this side.

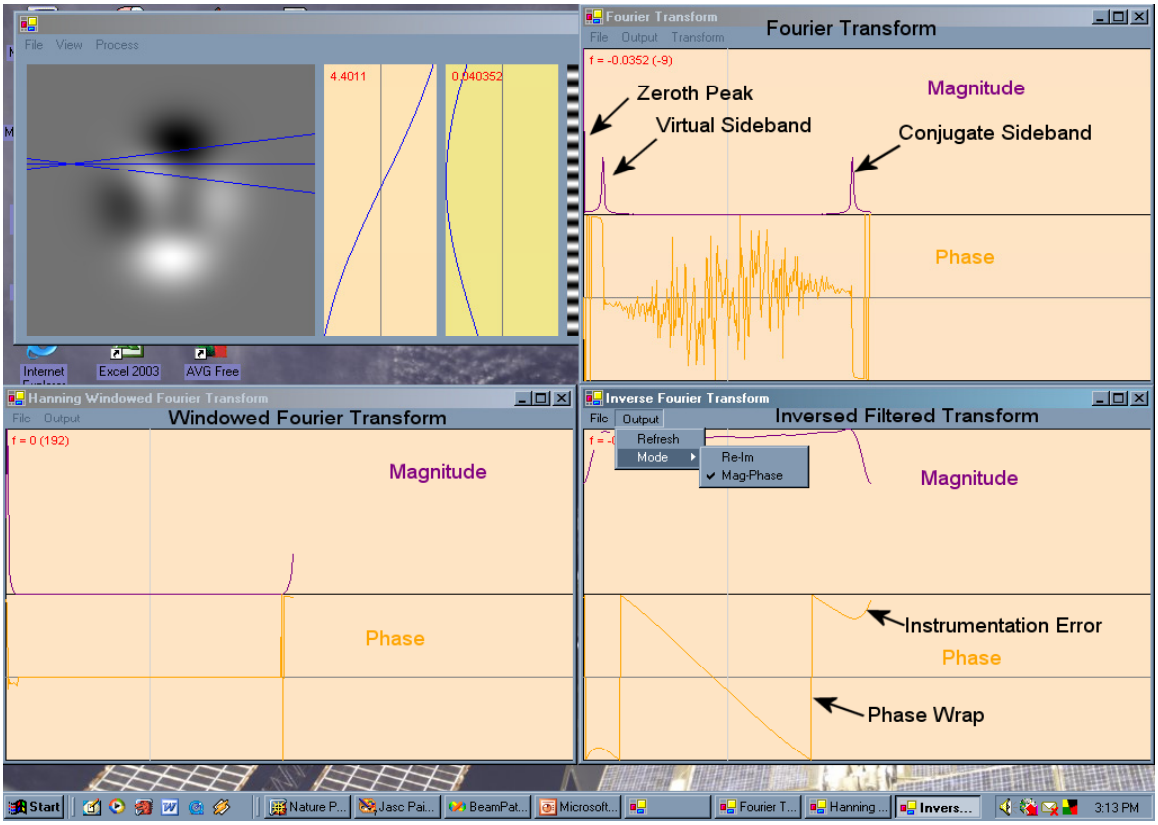

Figure 56: Details of Fourier filter windows shows Fourier filter (top right), windowed sideband (bottom left), and inverse windowed filter (bottom right).

The program can also display windows of the hologram in Fourier space as well as the resulting phase after windowing and shifting [Figure 56]. A variety of apodization functions are available to the user.

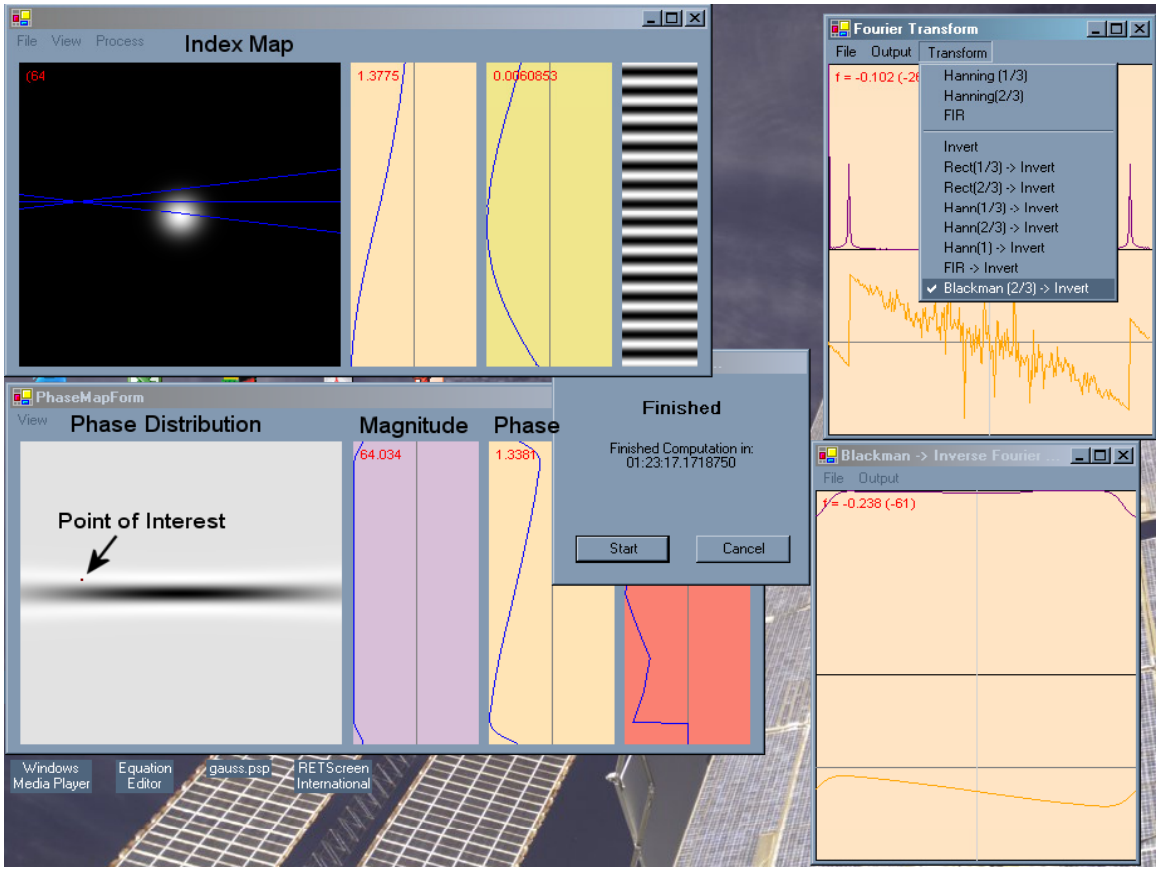

Figure 57: Screen shot depiction of phase profile map (bottom left) with associated magnitude and phase for a point of interest; phase distribution graphic is displaying kurtosis of phase.

In additional to allowing the user to select an individual point to examine it will also compute a phase map (bottom-left) of the phase profile for every voxel displayed on the index map [Figure 57]. Depending on the resolution settings this can take anywhere from seconds to hours to thousands of years to complete. The computation of the phase map also calculates a wide variety of statistical moments and can display their distributions graphically. The user can click on the phase map and the program will automatically place the confocal focus in the main window on the same point. This allows for easy comparison of the original simulated hologram and the Fourier filtered results.

4.6 Future Work

The software package developed for this analysis was written with the intention of being highly visual. It is in no way optimized for computational performance. Many of the data structures used are wasteful of computer memory in order to store results of

questionable value for the end result. For example, mean, variance, skewness, and kurtosis of the phase profile and 1st and 2nd derivatives of the phase profile are all stored in memory in spite of the fact that most are not computationally useful. The program needs to be adapted to act as a microscope control and reconstruction software package. In particular a module to control the motion control (beam scanning) hardware with synchronous camera acquisition is necessary. For performance reasons it would be logical to reprogram the system in C++ rather than Visual Basic and eliminate many of unneeded graphical computations.

A future version of the program should incorporate the ability to simulate the effect of Seidel aberrations such as spherical and coma into the ray propagation and hologram simulation module. Also, in addition to index of refraction each voxel should also contain information on the coefficient of scattering, coefficient of absorption, and anisotropic scattering factor to allow for the simulation of amplitude data.

The instrumentation error from the apodization function remains an ongoing problem. A potential solution is to investigate deconvolution algorithms. The most common use of deconvolution that I am aware of is in the field of adaptive optics. A literature review of this topic may yield a solution.

Lastly, the development of algorithms to recover the local variation in index of refraction from the phase measurement is needed for a variety of special cases. The incremental correction method has been shown to be effective for index distributions where the variation is independent for each axis [Lai, 2005]. The descriptive statistics heuristic method shows strong promise to be able to achieve accurate reconstruction of index for more complicated distributions. It appears to be particularly effective at the reconstruction of nearly normal distributions that are commonly found in nature.

5.0 Apparatus Vibration Analysis

5.1 Overview

All buildings have structural resonances that cause them to vibrate. The vibrations can disturb a number of scientific and engineering processes, such as semi-conductor fabrication, metrology, and interferometry. Vibration can create a great deal of fringe shift in time that destroys the sensitivity of the holographic microscope [Figure 58].

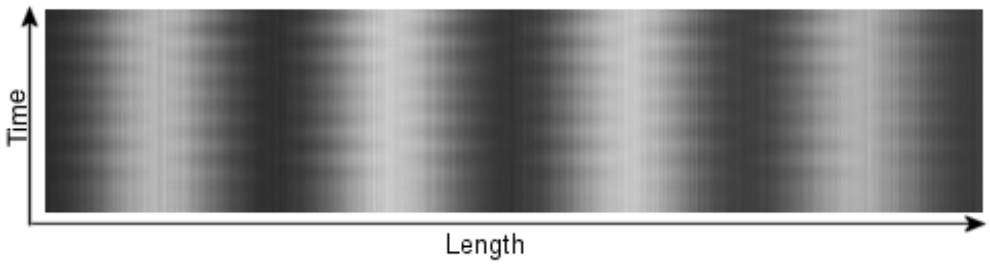

Figure 58: Interference fringes shift back and forth in time when the microscope is disturbed by structural vibration, making measurements impossible.

Structural vibrations are produced from a number of sources. Typical sources include:

1. Wind loading.
2. Vehicular traffic in the vicinity.
3. High-volume air conditioning (HVAC) and heating systems.
4. Operating machinery (such as mills, stamping presses).
5. Loading and unloading operations.

For the Engineering Lab Wing, the primary sources of vibration are most likely the ventilation system and the machinery in the machine shops. The machine shops mostly produce large transients when mills and stamps are in operation. The computer-assisted milling machines produce a steady-state vibration when they are operating, particularly the model in B127. These sources can be worked around through scheduling. However, the vibration produced by the ventilation system is a steady-state source that is always present. Hence there is no quiescent time when experiments could take place without being disturbed.

It is also possible that air currents could induce oscillations in the opto-mechanical hardware on the surface of the optical table. In addition to bulk flow of air applying

pressure to the table, acoustical vibrations can be transmitted through the air. Acoustical sources of vibration typically become important once a system is isolated from structural vibration.

5.2 Vibration Theory

If we assume that the structural vibrations are composed of a set of harmonic waves, the acceleration of the floor at some point can be expressed by

$$\mathrm{a}_z(t) = \sum_{n=0}^{N-1} A_n \sin(\nu_n t) \qquad 66$$

with N possible modes. While N can be arbitrarily large, to a good approximation only the components where A_n is a significant fraction of the overall power need to be considered. The obvious question is how to locate the associated frequencies ν_n.

The Fourier transform is very commonly used in signal processing [Oppenheim, 1975]. It is a means of transposing a function in time space to a function in frequency space.

$$\mathrm{H}(f) = \int_{-\infty}^{+\infty} \mathrm{h}(t) e^{2ift}\, dt \qquad 67$$

where *h(t)* is the continuous sampled function of time, *H(f)* is the continuous Fourier transform of the function. If a signal is composed of a small set of harmonic functions, then in frequency space those sinusoidal functions should be transposed to Dirac-like delta functions.

In the discrete case, the integral can be replaced by the Fourier series,

$$\mathrm{H}_\mathrm{d}(k\Delta f) = \Delta t \sum_{n=0}^{N-1} \mathrm{h}(n\Delta t) e^{2i\pi kn\Delta f\Delta t} \qquad 68$$

where N is the total number of samples, and k is the index for the computed set of discrete frequency components for k = 0,1,2, … N-1. Δt is the sampling interval; Δf is its equivalent in the frequency domain and is equal to $1/N\Delta t$.

As the resulting data set is complex, it contains both the magnitude and phase information for the frequencies. For analysis purposes the transform data are then separated into the two components. By graphing the magnitude versus the frequency it is easy to locate the peak frequencies that contribute to the recording vibration signal. Most

of the lesser components are not real but artifacts of white noise produced by the amplification electronics. The phase has no relevance in this case.

The *power* of the signal, denoted $P_{xx}(f)$, can be estimated from Fourier series as

$$\hat{\mathrm{P}}_{xx}(k\Delta f) = \frac{|H_d(k\Delta f)|^2}{\Delta t \Delta f N^2}. \qquad 69$$

This method of estimating the power spectrum density is known as a *periodogram*. It expresses the energy per unit time present in a given frequency of vibration.

In addition to determining the power in individual frequencies of vibration it is desirable to know the maximum displacement of the floor and table surface. The table displacement is an indication as to the expected shift seen in the interference pattern of the holographic microscope. The accelerometer measures acceleration and to find the displacement a double integration must be performed such that

$$\mathrm{z}(t) = \sum_{n=0}^{N-1} \frac{A_n}{\nu_n^2} \sin(\nu_n t). \qquad 70$$

Finding the set of harmonics ν_n for $z(t)$ is straightforward. In the simplest case, there is only one component frequency and so A_n is equal to twice the mean acceleration $\langle a \rangle$. A most rigorous analysis would integrate the vibration produced by each frequency and then create a superposition of many functions to determine the mean and maximum floor displacement.

If the vibration of both the table and floor can be measured simultaneously then it becomes desirable to determine the correlation of the two signals. The correlation between two sequences x and y can be described as

$$c_{xy}(i) = \sum_i \left(x_i - \langle x \rangle\right)\left(y_i - \langle y \rangle\right) \quad 71$$

where *i* spans the entire length of the sequences. It is similarly possible to compare a sequence to its previous values in time to look for periodicities in the data. This is known as the autocorrelation and defined as

$$c_{xx}(i) = \sum_j x_i x_{i+j} \ . \quad 72$$

5.3 Quantifying Sources of Vibration

By using two accelerometers to record simultaneous data, it becomes reasonable to analyze the coupling between the floor and the table surface through cross-correlation and cross power spectral density analysis. An experiment was conducted to attempt to quantify if the source of vibrations evident in the interference fringes was due to structural vibration, air currents, or acoustical coupling.

The objectives of this experiment were:

1. To establish if the isolation system is functioning to its specifications.
2. To attempt to determine if any source of vibration not transmitted through the isolation system is produced either by the table resonances or acoustical coupling.

See Appendix B for a discussion of the experimental procedure.

5.3.1 Statistical Analysis of Data

Once the vibration data has been collected from the accelerometers it is valuable to analyze it to see if there is correlation between the floor and optical table.

Table 7: Raw Accelerometer Outputs

Accelerometer	**RMS** (V)	**Maximum** (V)
Table	0.60	2.52
Floor	1.72	6.85
Noise	0.02	-

Cursory examination of the voltage data shows that the amplitude of the table is about three times less than that of the floor. This is consistent with previous observations. The noise was a measure of the combination of electronic noise, and circuit cross-talk. Noise is approximately 3.3 % of the signal strength.

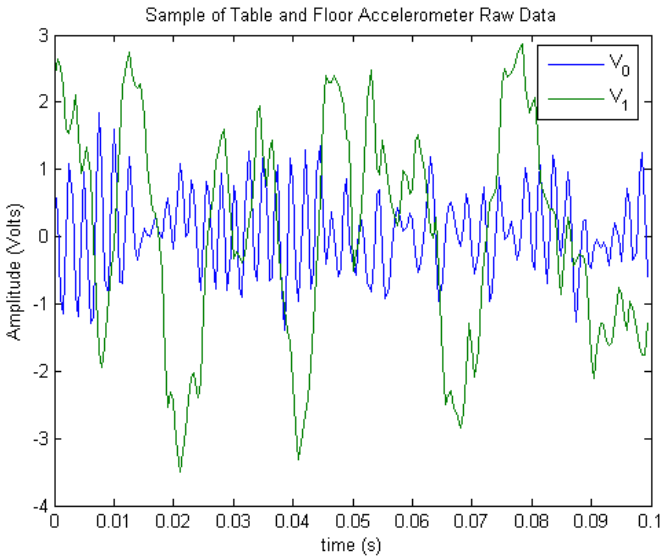

Figure 59: Graph of acceleration versus time for table (V_o) and floor (V_1) over 0.1 s

By observing the raw voltage data from the two accelerometers in parallel [Figure 59], we can quickly observe that the table (V_0) is missing the large amplitude, low-frequency component that is very obvious in the floor (V_1).

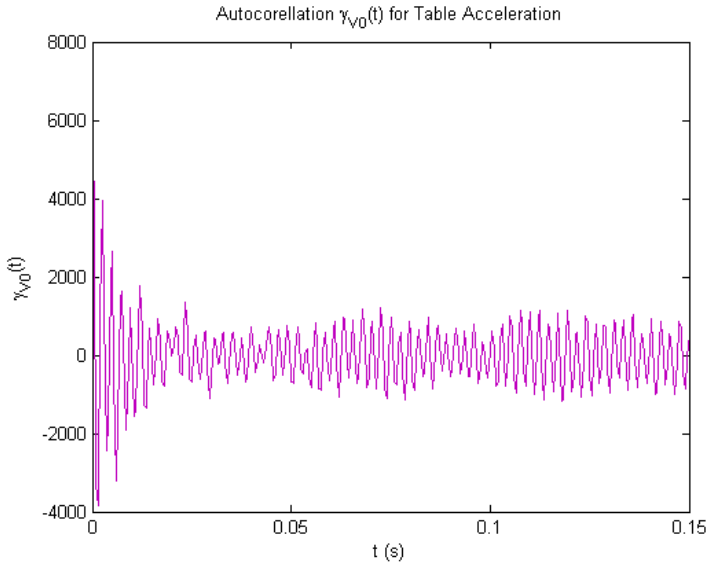

Figure 60: Autocorrelation of table vibration over 0.15 s

The autocorrelation of the table [Figure 60] shows that it is almost entirely a sinusoidal process, as the periodicity shows. There is decay for time shifts close to zero, which is suggestive of a moving average process, such as damping.

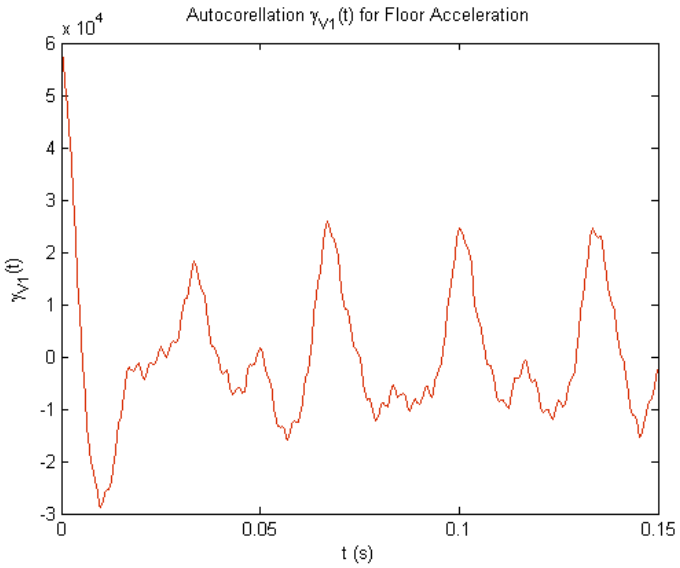

Figure 61: Autocorrelation of floor vibration over 0.15 s

The floor vibration autocorrelation is also almost entirely periodic [Figure 61]. It is unusual to see that the correlation begins highly positive, and then drops to become highly negative, before that process decays away and the periodic component dominants. Because the two signals are almost entirely periodic, the cross-correlation does not exhibit any interesting features.

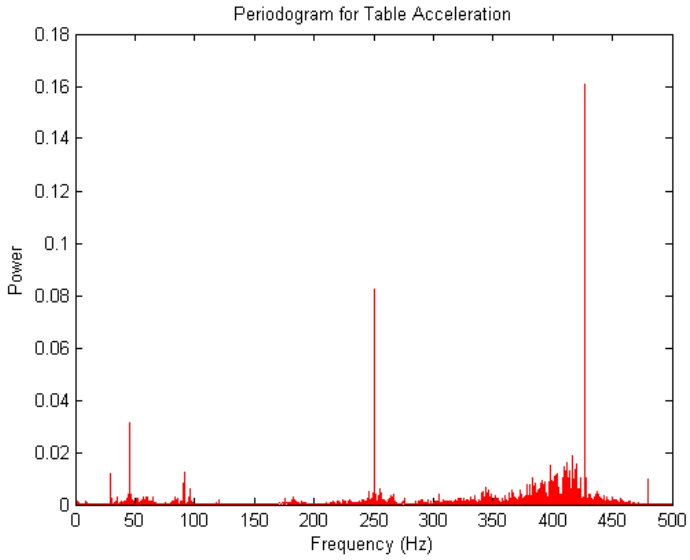

Figure 62: Periodogram of table vibration up to 500 Hz

The periodogram for the table surface [Figure 62] displays a surprising portion of the power spectrum density being contained at higher frequencies, particularly 250 Hz and 425 Hz. There is a lot of broad-band noise observed, which suggests a Gaussian white

noise source in addition to the major frequencies. At low frequencies (< 100 Hz) the largest frequency component appears at approximately 45 Hz with additional contributions from 30 and 90 Hz signals.

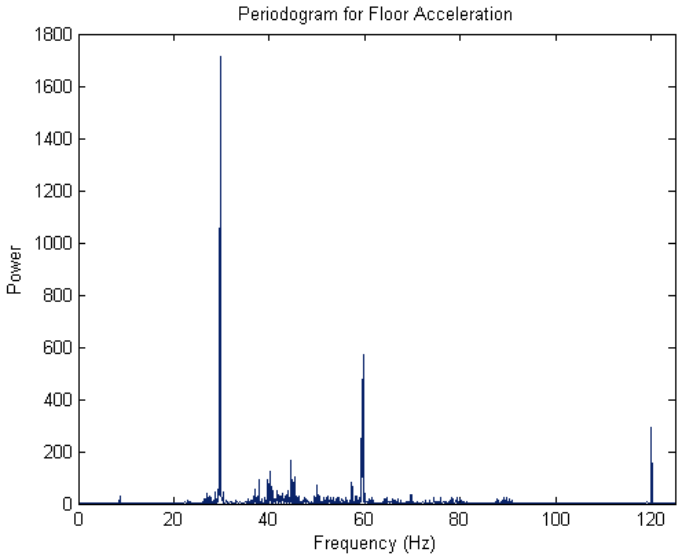

Figure 63: Periodogram of low frequency floor bibration up to 125 Hz

The floor power spectrum density is dominated by the lower frequencies [Figure 63]. At low frequencies the dominant component of the vibration spectrum is from a 30 Hz signal and its multi-modes at higher frequencies. Note the difference in the magnitude of the power at these frequencies compared to the peaks in the low frequency table periodogram. The power densities of the primary frequencies seen in the floor are much higher than those on the table surface.

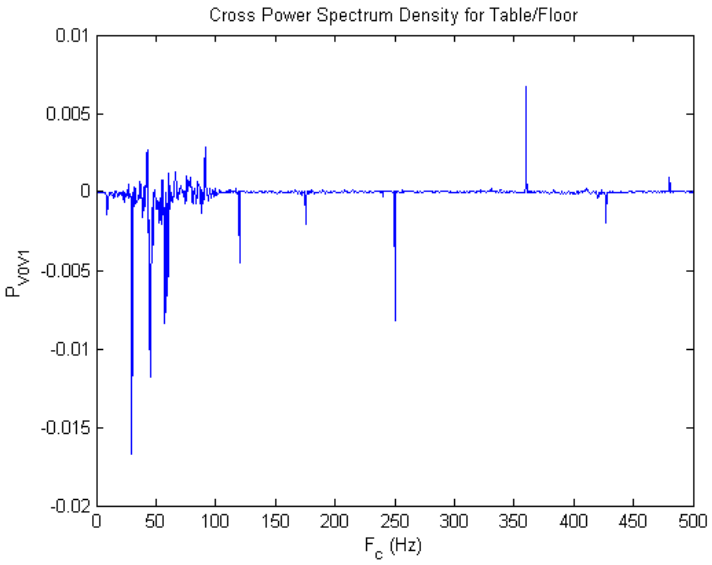

Figure 64: Cross power spectrum density of table and floor up to 500 Hz

The cross power spectrum density [Figure 64] shows mostly negative correlation between the frequency powers of the floor and the table. This shows that the table and the floor are not strongly coupled. Past 100 Hz there is practically no positive values, with the exception of a peak at 360 Hz. The positive cross power density at 360 Hz is somewhat strange. It is clearly a peak in the floor periodogram, but appears to be a part of the white noise in the table. That would suggest that it is an artifact in the data.

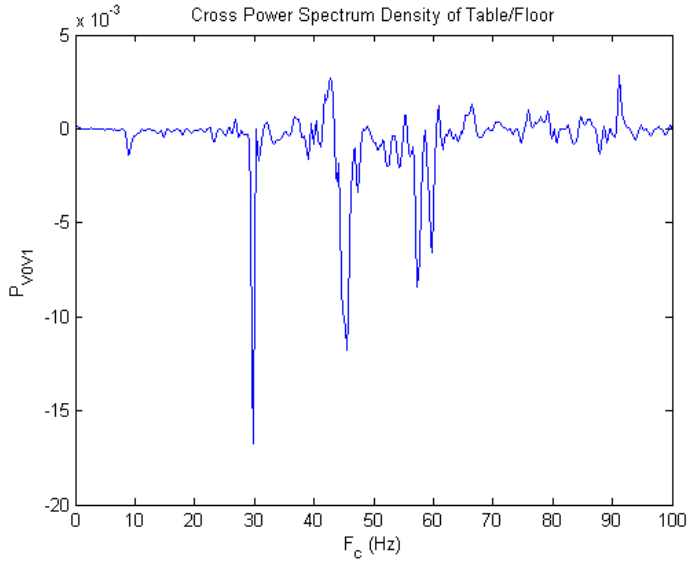

Figure 65: Low frequency cross power spectrum density of table and floor up to 100 Hz

The cross power spectrum in the range 0 – 100 Hz [Figure 65] shows that the table appears to be damping the 30 Hz and 60 Hz signals from the floor. The 90 Hz signal

appears to be high enough in frequency to penetrate the damping system, or perhaps acoustically couple.

5.3.2 Discussion of Results

The most important question is to try to identify the source of vibrations in the table surface. There are three possible sources:

1. Floor vibrations that pass through the isolating legs and into the table
2. Table resonant frequencies.
3. Acoustical coupling with noise produced by the HVAC system.

For transmission through the pneumatic isolators to the table we can look at the cross power spectrum density from 0.5 – 100 Hz. Generally what we expect to see is damping and some frequency shifting. Frequencies that are not totally damped by the isolators should be shifted to a slightly higher frequency. This appears to be what is happening. We can see that for every major negative peak, there is usually a slightly smaller positive peak at a slightly higher frequency. The power spectrum of the table itself shows that the energy of these low frequencies (0 – 100 Hz.) contains a minority of the energy in the entire table surface. At frequencies above these mechanical vibrations are usually not present and the dominant source is acoustical according to the manufacturer.

In the case of table resonances, they have to have an energy source to pump them, so it seems likely that increased isolation could create a more quiescent surface.

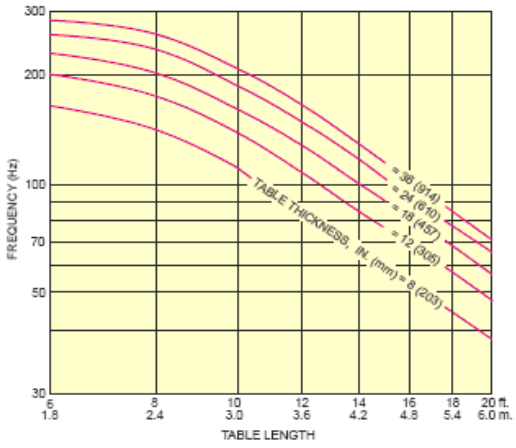

Figure 66: Minimum resonance rrequency for Newport optical tables [Newport, 2003]

The Newport RS4000 measures 1.5 m wide by 2.4 m long by 305 mm deep. According to [Figure 66] the lowest resonance frequency we should observe in the table surface is approximately 175 Hz. Examination of the table's power spectrum shows that there is some signal at that frequency but it is minor compared to peaks at 250 Hz and 425 Hz. These may be higher resonance frequencies in the table. They may also be acoustical frequencies that are present in the room.

The last potential noise source – acoustical coupling – is the most difficult to definitively establish. Subjectively we expect acoustical noise to be white, potentially with some resonance frequencies if they are emanating from a specific source. Without a microphone system and associated power spectrum we cannot establish the presence of acoustical resonances. However, we can assume that white noise is present and we can see the presence of white noise in the periodogram of the table surface accelerometer measurements. Most of the energy in the table is widely spread out through the upper frequency spectrums, which suggests either white acoustical noise, or white electrical noise in the amplification circuit.

Tests for noise in the circuit showed approximately 7.5 mV rms with the accelerometers disconnected. With one accelerometer operating the noise rose to approximately 20 mV rms, presumably due to some cross-talk through induction. With the accelerometer operating, the signal strength was approximately 600 mV rms. Thus the system noise is about 3.3 %. The noise present in the periodogram is greater than the electrical error so much of it must be comprised from acoustical sources.

5.3.3 Experiment Conclusions

The pneumatic isolator units are intended to operate over the region 0.1 – 100 Hz, with a resonance at approximately 1.2 Hz depending on their mass load. We have never seen the low frequency resonance from the pneumatic isolators in our measurements. The maximum power of any one frequency on the table surface is 0.03 at 45 Hz whereas the floor has a maximum power while the floor has a peak power of 1700 at 30 Hz. Since the advertised attenuation is approximate -60 dB at these frequencies the system is performing better than its claims. A note on the units for power: since the data was not transformed from Volts to m/s^2, the power is not Watts but it is a linearly relative value.

In terms of the acoustical coupling there does appear to be a Gaussian white noise source that is coupled to the table. This acoustical noise is exciting some of the table's higher structural resonant frequencies. White noise, being broad-band, is will pump any resonance frequencies in the system. This applies to not just the structure of the table itself but also to every component on the table. Hence it is very important to reduce the amount of white acoustical noise around the table surface or it will greatly increase the vibrational motion in the opto-mechanical components. The acoustical situation can be made more quiescent through modifications to the lab and the construction of an enclosure for the microscope system.

6.0 Conclusion

As a technique, optical confocal holographic microscopy holds promise to better characterize many physical processes in materials science, such as combustion and convection. It also may contribute to the biological sciences by imaging low-contrast, weak-phase objects. Thanks to the ongoing, continued improvement in computer processing speed it is now practical to reconstruct index of refraction maps from large sets of holograms. With further development confocal holography holds promise to become a popular method for imaging and characterization in the materials and biological sciences.

6.1 Methodological Advantages versus Tomography

As described in the body of the thesis the primary competition to optical confocal holography is optical tomographic holography. While tomography offers the potential for superior resolution along the optical axis it has been shown that confocal holography has valuable benefits for experiments. First, a beam scanning version of the confocal holographic microscope has been designed that will allow the examination of fluid experiments without inertial disturbance. Second, confocal holography only requires a signal flat optical window into the specimen chamber when operating in reflection mode, potentially increasing the number of experimental configurations that may be conducted. Together these advantages make confocal holography eminently more practical for truly non-invasive measurements of the internal index of refraction of materials.

6.2 Optical Design

The current state of the optical design has for all practical purposes reached its zenith. The optical performance of all lens systems has been optimized and aberrations minimized. Non-sequential analysis has demonstrated the ability of the system to conduct beam scanning and generated holograms from rigorous physical optical simulation.

In order to further improve the optical system experimentation is needed. With future experimental results it should become more practical to assess the trade-offs in amplitude versus wavefront split configurations. The effect of wavefront error and optics imperfections and the ability of reference holograms to remove their influence will

become apparent. The practicality of using polarizing optics to conduct beam splitting and filtering will become apparent. When the physical microscope is assembled actual spatial resolution of the system can be measured. The assembled system can be prepared for characterization of early experiments to establish the capabilities of the optical confocal holographic microscope.

6.3 Computer Simulation and Analysis

The use of computers to simulate holograms and analyze the results has been invaluable in advancing the understanding of how confocal holography works. The use of visual feedback was critical in demonstrating the critical importance of the phase profile to the ability to resolve objects in three-dimensions. By writing all aspects of the analysis program it was possible to remove the "black box" issues associated with third-party software packages. For example, the instrumentation error associated with apodization filters is ignored in most explanations of the reconstruction process but becomes highly deleterious for confocal holography. This creates the possibility for a solution in the future to this problem that will also contribute to the advancement of all holography techniques.

6.4 Caveat: Lack of Experimental Results

The development of the confocal holographic microscope has been hampered due to a lack of experimental data. The absence of experimental results is due to a contamination accident beyond our control in the optics laboratory which rendered unsafe or unusable the majority of our equipment. Another difficulty encountered was the unacceptable level of structural vibration found in the Engineering Lab Wing. Hopefully once equipment has been replaced the vibration issues will be more tolerable in the new laboratory space which is located much further away from the building HVAC system than the previous lab. As the experimental apparatus is restored to operating condition future advances in confocal holography should proceed at a swifter pace.

6.5 Educational Benefits

The development of the confocal holographic microscope was a broad project that required learning new science and techniques:

1. A much deeper understanding of wave interference and other optical phenomena than provided by undergraduate studies.
2. Research into a wide variety of optical systems from lasers to anti-reflection coatings to camera systems necessary to make purchasing decisions for equipment.
3. System integration and planning for a microscope consisting of several hundred parts and many interfaces.
4. Theory of structural vibration, its analysis and means of damping to create a quiescent environment.
5. Optical engineering using the popular commercial package *Zemax*.
6. Use of the CAD package *Pro/E* to design a solid model representation of the microscope.
7. The art of hologram reconstruction digitally via a computer. This in itself is a very broad topic centered on the theory of digital signal processing, a topic normally associated with electrical engineering.

Overall the thesis project has greatly expanded my research skills, made me a more critical creative thinker, and improved my discipline and work ethic. These lessons will remain valuable in any course of work that I undertake in the future.

Bibliography

Abe, Y. and Iwasaki, I. Observation of Vapor Bubble of Non-Azeotropic Binary Mixture in Microgravity with a Two-Wavelength Interferometer. Proceedings of the 5th ASME/JSME Joint Thermal Engineering Conference; San Diego. AJTE99-6418.

Born, M. and Wolf, E. Principles of Optics. Oxford: Pergamon Press; 1975.

Brenden, B. B. Acoustical holography. J. Phys. E: Sci. Instrum. 1975 Nov; (11):885-886.

Browne, J. A. and Herman, G. T. Computerized evaluation of image reconstruction algorithms. International Journal of Imaging Systems and Technology. 1996; 7(3):256-267.

Burden, R. L. and Faires, J. D. Numerical Analysis. Pacific Grove, CA: Brooks/Cole Publishing; 1997; ISBN: 0-534-95532-0.

Cathey, W. T. Optical Information Processing and Holography. New York: John Wiley & Sons; 1974; ISBN: 0-471-14078-3.

Chmelik, R.; Lovicar, L., and Harna, Z. Surface profilometry by a holographic confocal microscopy. Optica Applicata. 2003; 33(2-3):381-389.

Coherent staff. Coherent Inc. : Verdi - DPSS CW Pump Lasers [Web Page]. Accessed 2005 Dec. Available at: http://www.coherentinc.com/Lasers/index.cfm?fuseaction=show.page&id=873&loc=834.

Coufal, H. Holography: Solid information. Nature . 1998 Jun; 393:628-829. Notes: Holography Storage overview

Cowley, J. M. Twenty forms of electron holography. Ultramicroscopy. 1992 Jun; 41(4):335-348.

Crystalaser Staff. Ultra-Violet-Blue 375/405/415/440 nm Lasers [Web Page]. Accessed 2005 Dec. Available at: http://www.crystalaser.com/new/uv-laser.html, http://www.crystalaser.com/homenew.html#infrared.

Dezhong, W. and Tiange, Z. The measurement of 3-D asymmetric temperature field by using real time laser interferometric tomography. Optics and Lasers in Engineering. 2001 Sep; 36(3):289-297.

Dixon, A. E.; Damaskinos, S., and Atkinson, M. R. A scanning confocal microscope for transmission and reflection imaging. Nature. 1991; 351:551-553.

Eastman Kodak Company staff. KLI-8800 8000 Element Linear CCC Image Sensor Performance Specification. Rev 0 ed.. Rochester, NY; 2000 Oct 3.

Feng, J.; Okamoto, K.; Tsuru, D.; Madarame, H., and Fumizawa, M. Visualization of 3D gas density distribution using optical tomography. Chemical Engineering Journal. 2002 Apr 28; 86(3):243-250.

Focus Software staff. ZEMAX Optical Design Program. 10.0 ed. Tucson: Focus Software; 2001.

Fujita, T. and McCartney, M. R. Phase recovery for electron holography using Gerchberg–Papoulis iterative algorithm. Ultramicroscopy. 2005 Mar; 102(4):279-286.

Furlong, C.; Siegel, A. M., and Pryputniewicz, R. J. Confocal optoelectronic holography microscope for materials and structural characterization of MEMS. Materials Research Society Symposium Proceedings: G12.4. 109-114.

Gabor, D. Microscopy by Reconstructed Wave Fronts, I. Proceedings of the Royal Society of London, A. 1949 Jul; 197(1051):454-487.

Gabor, D. Microscopy by Resconstructed Wave Fronts, II. The Proceedings of the Physical Society . 1951 Jun; 64(6):449-469.

---. Theory of Electron Interference Experiments. Reviews of Modern Physics. 1956 Jul; 28(3):260-276.

Geola uab & Slavich OAO staff. Emulsions for Holography [Web Page]. Accessed 2005 Nov 29. Available at: http://www.slavich.com/technical.htm.

Hamilton, D. K. and Matthews, H. J. The confocal interference microscope as a surface profilometer. Optik. 1985; 71(1):31-34.

Harihanan, P. Basics of Interferometry. Boston: Academic Press; 1992.

Hecht, E. Optics. 3rd ed. Addison Wesley Longman; 1998.

Herring, R. A. Confocal scanning Laser holography, and an associated microscope: a proposal. Optik. 1997; 105:65-68.

Huber, G.; Kellner, T.; Kretschmann, H. M.; Sandrock, T., and Scheife, H. Compact diode pumped cw solid-state lasers in the visible spectral region. Optical Materials. 1999 Jan; 11(2-3):205-216.

Kak, A. and Slaney, M. Principles of Computerized Tomographic Imaging. 2nd ed. New York: IEEE Press; 2001.

Karim, M. A. and Awwal, A. A. S. Optical Computing: An Introduction. New York: John Wiley & Sons; 1992.

Lai, G.; Hirayami, T.; Ishizuka, K.; Takayoshi, T., and Tonomura, A. Three-dimensional

reconstruction of electric-potential distribution in electorn-holographic interferometry. Applied Optics. 1994 Feb; 33(5):829-833.

Lai, S. An Algorithm for 3-D Refractive Index Measurement in Holographic Confocal Microscopy. Ultramicroscopy. In Print; 7 pages.

Laurin, D. (Hertzberg Institute of Astrophysics). [Personal communication regarding design of telecentric lenses.]Victoria, BC; 2004 Feb.

Lehmann, M. and Lichte, H. Tutorial on Off-Axis Electron Holography. Microscopy & Microanalysis. 2002; 8:447-466.

Leith, E. N. and Upatnieks, J. Wavefront reconstruction with diffused illumination and three-dimensional objects. Journal of the Optical Society of America - A. 1964; 54:1295-1301.

Levitan, E. and Herman, G. T. A Maximum A Posteriori Probability Expectation Maximization Algorithm for Image Reconstruction in Emission Tomography. IEEE Transactios on Medical Imaging. 1987 Sep; 6(3):185-192.

Melles Griot staff. Melles Griot: The Pratical Application of Light. Carlsbad, CA; 1999pp.11.10-11.11.

Mewes, D. Measurement of temperature fields by holographic tomography. Experimental Thermal and Fluid Science. 1991 Mar; 4(2):171-181.

Michalski, J. What is Telecentricity? [Web Page]. Accessed 2005 Dec. Available at: http://www.edmundoptics.com/techsupport/displayarticle.cfm?articleid=261.

Newport staff. Newport Resource 2003. Irvine, CA ; 2003p.1174www.newport.com.

Oppenheim, A. and Schafer, R. Digital Signal Processing. London: Prentice-Hall International; 1975.

Palacios, F.; Ricardo, J.; Palacios, D.; Goncalves, E.; Valin, J. L., and De Souza, R. 3D image reconstruction of transparent microscopic objects using digital holography. Optics Communications. 2005 Apr 1; 248(1-3):41-50.

Philipp, H.; Neger, T.; Jager, H., and Woisetschlager, J. Optical tomography of phase objects by holographic interferometry. Measurement. 1992; 10(4):170-181.

Press, W.; Flannery, B.; Teukolsky, S., and Vetterling, W. Numerical Recipes in C. 2nd ed. Cambridge: Cambridge University PRess; 1992.

Rea, N. P.; Wilson, T., and Juskaitis, R. Semiconductor laser confocal and interference microscopy. Optics Communications. 1996 Apr 1; 125(1-3):158-167.

Roggemann, M. C.; Welsh, B. M.; Gardner, P. J.; Johnson, R. L., and Pedersen, B. L.

Sensing three-dimensional index-of-refraction variations by means of optical wavefront sensor mesaurements and tomographic reconstruction. Optical Engineering. 1995 May; 34(5):1374-1383.

Rothwell, T. A. and Shegelski, M. R. A. Tomographic reconstruction of multiple in-line electron holograms of realistic objects. Micron. 2005 Jan; 36(1):31-45.

Saxby, G. Practical Holography. New York: Prentice Hall; 1998.

Schnars, U. and Juptner, W. P. O. Digital Recording and Reconstruction of Holograms. Measurement Science and Technology. 2002 Aug; 13:R85 - R101.

Sorzano, C. O. S.; Marabini, R.; Herman, G. T., and Carazo, J. M. Multiobjective algorithm parameter optimization using multivariate statistics in three-dimensional electron microscopy reconstruction. Pattern Recognition. 2005 Dec; 38(12):2587-2601.

Steiner, R.; Kunzi-Rapp, K., and Scharffetter-Kochanek, K. Optical Coherence Tomography: Clinical Applications in Dermatology. Medical Laser Application. 2003; 18(3):249-259.

Sur, B.; Rogge, R. B.; Hammond, R. P.; Anghel, V. N. P., and Katsaras, J. Atomic structure holography using thermal neutrons. Nature. 2001 Nov; 414:525-527.

Timmerman, B. H.; Watt, D. W., and Bryanston-Cross, P. J. Quantitative visualization of high-speed 3D turbulent flow structures using holographic interferometric tomography. Optics & Laser Technology. 1999 Feb; 31(1):53-65.

Tonomura, A. Electron Holography. Berlin - New York: Springer-Verlag; 1993. (H. Lotsch. Springer Series in Optical Sciences; 70).

Vest, C. M. Holographic interferometry. New York : Wiley & Sons; 1979.

Volkl, E. and Lehmann, M. The Reconstruction of Off-Axis Electron Holograms. E. Volkl, L. F. Allard D. C. Joy. Introduction to Electron Holography. 1st ed. New York: Kluwer Academic; 1999.

Wang D. and Zhuang T. The measurement of 3-D asymmetric temperature field by using real time laser interferometric tomography. Optics and Lasers in Engineering. 2001 Sep; 36(3):289-297.

Weiner, N. Extrapolation, Interpolation, and Smoothing of Stationary Time Series. Boston: MIT Press; 1964; ISBN: 0-262-73005-7.

Weisstein, E. W. Apodization Function [Web Page]. Accessed 2005 Aug 11. Available at: http://mathworld.wolfram.com/ApodizationFunction.html.

Weisstein, E. W. Central Moment [Web Page]. Accessed 2005 Aug 13. Available at:

http://mathworld.wolfram.com/CentralMoment.html.
Notes: Also: http://mathworld.wolfram.com/RawMoment.html,
http://mathworld.wolfram.com/Skewness.html,
http://mathworld.wolfram.com/Kurtosis.html

Wikipedia. Holographic Versatile Disk [Web Page]. Accessed 2005 Aug 2. Available at: http://en.wikipedia.org/wiki/Holographic_Versatile_Disc.

Yang, G. G; Chen, H. S., and Leith, E. N. Volume Reflection Holographic Confocal Imaging. Applied Optics. 2000 Aug; 39(23):4076-4079.

Appendix A – Zemax Model Parameters

A.1 Prototype Sample Scan Confocal Holographic Microscope

- Non-sequential
- 457.5 nm wavelength
- Linear polarized light

Object #	Object Type	Comment	Ref Object	Inside Of	X Position	Y Position	Z Position
1	Source Ellipse	BE1	0	0	0	0	0
2	Null Object	WAVEFRONT SPLITTER	0	0	0	0	50
3	Poly Object	PRISM25.POB	2	0	0	0	0
4	Poly Object	PRISM25.POB	2	0	0	0	48
5	Null Object	----------	0	0	0	0	0
6	Null Object	TELECENTRIC	2	0	0	0	100
7	Poly Object	PRISM22-5.POB	6	0	0	0	0
8	Standard Lens	LPX178	6	0	0	0	65
9	Standard Lens	LAO124	8	0	0	0	9.5665
10	Standard Lens	LAO124	9	0	0	0	6.23
11	Standard Lens	LPX137	9	0	0	0	30.9006
12	Null Object	CONFOCAL	11	0	0	0	16.6946
13	Standard Lens	LPX137	12	0	0	0	11.494631
14	Standard Lens	LAO124	13	0	0	0	27.3706
15	Standard Lens	LAO124	14	0	0	0	2.5
16	Standard Lens	LPX178	15	0	0	0	11.5965
17	Null Object	----------	0	0	0	0	0
18	Null Object	APERATURE LENS	16	0	0	0	35
19	Standard Lens	LPX178	18	0	0	0	0
20	Standard Lens	LAO124	19	0	0	0	9.5665
21	Standard Lens	LAO124	20	0	0	0	6.23
22	Standard Lens	LPX137	20	0	0	0	30.9006
23	Annulus	APERATURE 1	18	0	0	11.374	39.45
24	Annulus	APERATURE 2	18	0	0	-11.374	39.45
25	Null Object	----------	0	0	0	0	0
26	Null Object	PROJECTOR	18	0	0	0	100
27	Poly Object	PRISM10-0.POB	26	0	0	0	0
28	Standard Lens		27	0	0	0	10
29	Detector Rect	CAMERA	26	0	0	0	215

Object #	Tilt About X	Tilt About Y	Tilt About Z	Material	Param 1	Param 2
1	0	0	0	-	400	200000000

2	0	0	0	-			
3	0	0	0	BK7	17.5	1	
4	180	0	0	BK7	17.5	1	
5	0	0	0	-			
6	0	0	0	-			
7	0	0	0	BK7	16.5	1	
8	0	0	0	BK7	51.822	0	
9	0	0	0	SK11	64.279745	0	
10	0	0	0	SF5	-44.980209	0	
11	0	0	0	BK7	36.311	0	
12	0	0	0	-			
13	0	0	0	BK7	0	0	
14	0	0	0	SF5	180.440274	0	
15	0	0	0	SK11	44.980209	0	
16	0	0	0	BK7	0	0	
17	0	0	0	-			
18	0	0	0	-			
19	0	0	0	BK7	51.822	0	
20	0	0	0	SK11	64.279745	0	
21	0	0	0	SF5	-44.980209	0	
22	0	0	0	BK7	36.311	0	
23	0	0	0	ABSORB	15	15	
24	0	0	0	ABSORB	15	15	
25	0	0	0	-			
26	0	0	0	-			
27	0	0	0	BK7	17.5	1	
28	0	0	0	BK7	-100	0	
29	0	0	90	ABSORB	25	25	

Object #	Param 3	Param 4	Param 5	Param 6	Param 7	Param 8	Param 9
1	0.1	0	0	6	6	0	0
2							
3							
4							
5							
6							
7							
8	15	15	4.2	0	0	15	15
9	15	15	6.23	-44.980209	0	15	15
10	15	15	2.5	-180.440274	0	15	15
11	15	15	5.2	0	0	15	15
12							
13	15	15	5.2	-36.311	0	15	15
14	15	15	2.5	44.980209	0	15	15
15	15	15	6.23	-64.279745	0	15	15
16	15	15	4.2	-51.822	0	15	15
17							
18							
19	15	15	4.2	0	0	15	15
20	15	15	6.23	-44.090209	0	15	15

21	15	15	2.5	-180.440275	0	15	15
22	15	15	5.2	0	0	15	15
23	0.05	0.05					
24	0.05	0.05					
25							
26							
27							
28	25	25	1.25	0	0	25	25
29	500	500	1	2	0	0	0

A.2 Beam Scan Confocal Holographic Microscope

- Non-sequential
- 457.5 nm wavelength
- Linear polarized light

Wavefront Split Configuration:

Object #	Object Type	Comment	Ref Object	Inside Of	X Position	Y Position	Z Position
1	Standard Surface	BEAMSTOP	0	0	0	0	-1
2	Source Ellipse	BE1	0	0	0	0	0
3	Null Object	WAVEFRONT SPLITTER	0	0	0	0	35
4	Poly Object	PRISM25.POB	3	0	0	0	0
5	Poly Object	PRISM25.POB	3	0	0	0	48
6	Null Object	----------	0	0	0	0	0
7	Null Object	BEAMSPLITTER 1	3	0	0	0	125
8	Poly Object	BEAMSPLITCUBE.POB	7	0	0	0	0
9	Poly Object	BEAMSPLITCUBE.POB	8	0	0	0	0
10	Standard Surface	BEAMTRAP	7	0	0	150	0
11	Null Object	----------	0	0	0	0	0
12	Null Object	GALVO 1-Y	7	0	0	0	350
13	Rectangle	SM1	12	0	0	0	0
14	Rectangular Volume	SM1 BODY	13	0	0	-81	0
15	Standard Lens	PERISCOPE SM1-1	12	0	0	75	0
16	Standard Lens	PERISCOPE SM1-2	12	0	0	316.75	0
17	Null Object	----------	0	0	0	0	0
18	Null Object	GALVO 2-X	12	0	0	391.25	0
19	Rectangle	SM2	18	0	0	0	0
20	Rectangular Volume	SM2 BODY	19	0	-53	0	0
21	Standard Lens	PERISCOPE SM2-1	18	0	0	0	75
22	Standard Lens	PERISCOPE SM2-2	18	0	0	0	316.75
23	Null Object	----------	0	0	0	0	0
24	Null Object	BEAMSPLITTER2	18	0	0	0	391.25
25	Poly Object	BEAMSPLITCUBE.POB	24	0	0	0	0
26	Poly Object	BEAMSPLITCUBE.POB	24	0	0	0	0
27	Null Object	----------	0	0	0	0	0
28	Null Object	TELECENTRIC	24	0	0	0	75

29	Poly Object	PRISM22-5.POB	28	0	0	0	0
30	Standard Lens	TELECENTRIC 1	29	0	0	0	75
31	Standard Lens	TELECENTRIC 2	30	0	0	0	46.02
32	Detector Rect	SAMPLE	31	0	0	0	55
33	Standard Lens	TELECENTRIC 3	31	0	0	0	110
34	Standard Lens	TELECENTRIC 4	33	0	0	0	-46.02
35	Poly Object	PRISM22-5.POB	34	0	0	0	-75
36	Null Object	----------	0	0	0	0	0
37	Null Object	LOOP MIRRORS	35	0	0	0	-75
38	Standard Surface	BT2	24	0	0	150	0
39	Standard Surface	M1	37	0	0	0	0
40	Standard Surface	M2	37	0	0	-175	0
41	Standard Lens	PERI LOOP 1	24	0	0	-175	81
42	Standard Lens	PERI LOOP 2	24	0	0	-175	421
43	Standard Surface	M3	24	0	0	-175	0
44	Null Object	----------	0	0	0	0	0
45	Null Object	CAMERA PATH	7	0	0	-300	0
46	Standard Surface	M4	45	0	0	0	0
47	Poly Object	PRISM22-5.POB	45	0	0	0	150
48	Standard Lens	CONFOCAL 1	47	0	0	0	75
49	Standard Lens	CONFOCAL 2	48	0	0	0	46.02
50	Detector Rect	APERTURE CAM	49	0	0	12.4183	57.249
51	Standard Surface	25UM APERTURE	49	0	0	12.4183	57.25
52	Standard Surface	25UM APERTURE	49	0	0	-12.4183	57.25
53	Detector Rect	POST-AP CAM	49	0	0	12.4183	57.251
54	Poly Object	PRISM12-5.POB	49	0	0	0	90
55	Standard Lens	PROJECTOR 1	54	0	0	0	15
56	Detector Rect	CCD CAMERA	55	0	0	0	120

Object #	Tilt About X	Tilt About Y	Tilt About Z	Material	Param 1	Param 2
1	0	0	0	ABSORB	0	0
2	0	0	0	-	300	200000000
3	0	0	0	-		
4	0	0	0	BK7	17.5	1
5	180	0	0	BK7	17.5	1
6	0	0	0	-		
7	0	0	0	-		
8	0	90	0	BK7	50.8	1
9	0	0	180	BK7	50.8	1
10	90	0	0	ABSORB	0	0
11	0	0	0	-		
12	0	0	0	-		
13	45	0	0	MIRROR	35	59.45
14	90	0	0	ABSORB	34.25	40
15	-90	0	0	BK7	57.2395	-0.608952
16	90	0	0	BK7	57.2395	-0.608952
17	0	0	0	-		
18	0	0	0	-		
19	45	0	0	MIRROR	33	46.5
20	0	-90	0	ABSORB	34.25	40
21	0	0	0	BK7	57.2395	-0.608952

22	180	0	0	BK7	57.2395	-0.608952	
23	0	0	0	-			
24	0	0	0	-			
25	0	90	90	BK7	50.8	1	
26	0	90	270	BK7	50.8	1	
27	0	0	0	-			
28	0	0	0	-			
29	0	0	0	BK7	17.5	1	
30	0	0	0	BK7	111.248085	0	
31	0	0	0	BK7	49.782232	0	
32	0	0	90		15	5	
33	180	0	0	BK7	49.782232	0	
34	0	0	0	BK7	111.248085	0	
35	0	0	0	BK7	17.5	1	
36	0	0	0	-			
37	180	0	0	-			
38	90	0	0	ABSORB	0	0	
39	-45	0	0	MIRROR	0	0	
40	45	0	0	MIRROR	0	0	
41	0	0	0	BK7	84.905406	-0.661406	
42	180	0	0	BK7	84.905406	-0.661406	
43	135	0	0	MIRROR	0	0	
44	0	0	0	-			
45	0	0	0	-			
46	-45	0	0	MIRROR	0	0	
47	0	0	0	BK7	17.5	1	
48	0	0	0	BK7	111.248085	0	
49	0	0	0	BK7	49.782232	0	
50	0	0	90		0.1	0.1	
51	0	0	0	ABSORB	0	0	
52	0	0	0	ABSORB	0	0	
53	0	0	90		0.1	0.1	
54	0	0	0	BK7	17.5	1	
55	0	0	0	BK7	-300	0	
56	0	0	90	ABSORB	28.672	28.672	

Object #	Param 3	Param 4	Param 5	Param 6	Param 7	Param 8	Param 9
1	30	0					
2	0.1	0	0	12.75	12.75	0	0
3							
4							
5							
6							
7							
8							
9							
10	30	0					
11							
12							
13							
14	180	34.25	40	0	0	0	0

15	45	45	30	0	0	45	45
16	45	45	30	0	0	45	45
17							
18							
19							
20	180	34.25	40	0	0	0	0
21	45	45	30	0	0	45	45
22	45	45	30	0	0	45	45
23							
24							
25							
26							
27							
28							
29							
30	45	45	30	-124.179652	0	45	45
31	30	30	30	0	0	30	30
32	900	300	0	2	0	0	0
33	30	30	30	0	0	30	30
34	45	45	30	-124.179652	0	45	45
35							
36							
37							
38	30	0					
39	50	0					
40	50	0					
41	45	45	20	0	0	45	45
42	45	45	20	0	0	45	45
43	50	0					
44							
45							
46	50	0					
47							
48	45	45	30	-124.179652	0	45	45
49	30	30	30	0	0	30	30
50	500	500	0	2	0	0	0
51	10	0.0125					
52	10	0.0125					
53	500	500	0	2	0	0	0
54							
55	30	30	1.2	0	0	30	30
56	1024	1024	1	2	0	0	0

Amplitude Split Configuration:

Object #	Object Type	Comment	Ref Object	Inside Of	X Position	Y Position	Z Position
1	Source Ellipse	BE1	0	0	0	0	0
2	Null Object	WAVEFRONT SPLITTER	0	0	0	0	50

3	Null Object	----------	0	0	0	0	0
4	Null Object	BEAMSPLITTER 1	2	0	0	0	125
5	Poly Object	BEAMSPLITCUBE.POB	4	0	0	0	0
6	Poly Object	BEAMSPLITCUBE.POB	5	0	0	0	0
7	Standard Surface	REFERENCE MIRROR	4	0	0	150	0
8	Null Object	----------	0	0	0	0	0
9	Null Object	GALVO 1-Y	4	0	0	0	350
10	Rectangle	SM1	9	0	0	0	0
11	Rectangular Volume	SM1 BODY	10	0	0	-81	0
12	Standard Lens	PERISCOPE SM1-1	9	0	0	75	0
13	Standard Lens	PERISCOPE SM1-2	9	0	0	316.75	0
14	Null Object	----------	0	0	0	0	0
15	Null Object	GALVO 2-X	9	0	0	391.25	0
16	Rectangle	SM2	15	0	0	0	0
17	Rectangular Volume	SM2 BODY	16	0	-53	0	0
18	Standard Lens	PERISCOPE SM2-1	15	0	0	0	75
19	Standard Lens	PERISCOPE SM2-2	15	0	0	0	316.75
20	Null Object	----------	0	0	0	0	0
21	Null Object	BEAMSPLITTER2	15	0	0	0	391.25
22	Poly Object	BEAMSPLITCUBE.POB	21	0	0	0	0
23	Poly Object	BEAMSPLITCUBE.POB	21	0	0	0	0
24	Null Object	----------	0	0	0	0	0
25	Null Object	TELECENTRIC	21	0	0	0	75
26	Standard Lens	TELECENTRIC 1	25	0	0	0	75
27	Standard Lens	TELECENTRIC 2	26	0	0	0	46.02
28	Standard Lens	TELECENTRIC 3	27	0	0	0	112.86
29	Standard Lens	TELECENTRIC 4	28	0	0	0	-46.02
30	Null Object	----------	0	0	0	0	0
31	Null Object	LOOP MIRRORS	29	0	0	0	-125
32	Standard Surface	BT2	21	0	0	150	0
33	Jones Matrix	HALF-WAVE PLATE	21	0	0	-75	0
34	Standard Surface	M1	31	0	0	0	0
35	Standard Surface	M2	31	0	0	-175	0
36	Standard Lens	PERI LOOP 1	21	0	0	-175	81
37	Standard Lens	PERI LOOP 2	21	0	0	-175	421
38	Standard Surface	M3	21	0	0	-175	0
39	Null Object	----------	0	0	0	0	0
40	Null Object	CAMERA PATH	4	0	0	-300	0
41	Standard Surface	M4	40	0	0	0	0
42	Standard Lens	CONJ 1	40	0	0	0	100
43	Standard Lens	CONJ 2	40	0	0	0	146.02
44	Detector Rect	CAMERA 1	40	0	0	0	300
45	Detector Rect	CAMERA 2	40	0	0	0	300

Object #	Tilt About X	Tilt About Y	Tilt About Z	Material	Param 1	Param 2
1	0	0	0	-	300	50000000
2	0	0	0	-		
3	0	0	0	-		
4	0	0	0	-		
5	0	90	0	BK7	50.8	1

6	0	0	180	BK7	50.8	1	
7	90	0	0	MIRROR	0	0	
8	0	0	0	-			
9	0	0	0	-			
10	45	0	0	MIRROR	35	59.45	
11	90	0	0	ABSORB	34.25	40	
12	-90	0	0	BK7	57.2395	-0.608952	
13	90	0	0	BK7	57.2395	-0.608952	
14	0	0	0	-			
15	0	0	0	-			
16	45	0	0	MIRROR	33	46.5	
17	0	-90	0	ABSORB	34.25	40	
18	0	0	0	BK7	57.2395	-0.608952	
19	180	0	0	BK7	57.2395	-0.608952	
20	0	0	0	-			
21	0	0	0	-			
22	0	90	90	BK7	50.8	1	
23	0	90	270	BK7	50.8	1	
24	0	0	0	-			
25	0	0	0	-			
26	0	0	0	BK7	111.248085	0	
27	0	0	0	BK7	49.782232	0	
28	180	0	0	BK7	49.782232	0	
29	0	0	0	BK7	111.248085	0	
30	0	0	0	-			
31	180	0	0	-			
32	90	0	0	ABSORB	0	0	
33	90	0	0		25	25	
34	-45	0	0	MIRROR	0	0	
35	45	0	0	MIRROR	0	0	
36	0	0	0	BK7	84.905406	-0.661406	
37	180	0	0	BK7	84.905406	-0.661406	
38	135	0	0	MIRROR	0	0	
39	0	0	0	-			
40	0	0	0	-			
41	-45	0	0	MIRROR	0	0	
42	0	0	0	BK7	111.248085	0	
43	0	0	0	BK7	111.248085	0	
44	0	0	0		12.5	12.5	
45	0	0	0		1	1	

Object #	Param 3	Param 4	Param 5	Param 6	Param 7	Param 8	Param 9
1	0.1	0	0	12.75	12.75	0	0
2							
3							
4							
5							
6							

7	30	0					
8							
9							
10							
11	180	34.25	40	0	0	0	0
12	45	45	30	0	0	45	45
13	45	45	30	0	0	45	45
14							
15							
16							
17	180	34.25	40	0	0	0	0
18	45	45	30	0	0	45	45
19	45	45	30	0	0	45	45
20							
21							
22							
23							
24							
25							
26	45	45	30	-124.179652	0	45	45
27	30	30	30	0	0	30	30
28	30	30	30	0	0	30	30
29	45	45	30	-124.179652	0	45	45
30							
31							
32	30	0					
33	0	0	1	0	1	0	0
34	50	0					
35	50	0					
36	45	45	20	0	0	45	45
37	45	45	20	0	0	45	45
38	50	0					
39							
40							
41	50	0					
42	45	45	30	-124.179652	0	45	45
43	30	30	30	0	0	30	30
44	1000	1000	1	2	0	0	0
45	1000	1000	1	2	0	0	0

A.3 Telecentric Lens Systems

A.3.1 Commercial High-Resolution 1A Telecentric for Prototype System

- Sequential Mode
- 457.5 nm wavelength
- Fields: ±10°, ±12°, ±14°

- Entrance aperture diameter: 10 mm

#	Type	Comm	Curvature	Thickness	Glass	Semi-Diameter	Conic	Param 0	Param 1	Param 2	Param 3
0	STANDARD		0.00E+00	1.00E+10		0.00E+00	0.00E+00	0.00E+00	0.00E+00	0.00E+00	0.00E+00
1	STANDARD		0.00E+00	1.50E+01		5.00E+00	0.00E+00	0.00E+00	0.00E+00	0.00E+00	0.00E+00
2	STANDARD	LPX178	1.93E-02	4.20E+00	BK7	1.50E+01	0.00E+00	0.00E+00	0.00E+00	0.00E+00	0.00E+00
3	STANDARD		0.00E+00	5.37E+00		1.50E+01	0.00E+00	0.00E+00	0.00E+00	0.00E+00	0.00E+00
4	STANDARD	LAO124	1.56E-02	6.23E+00	SK11	1.50E+01	0.00E+00	0.00E+00	0.00E+00	0.00E+00	0.00E+00
5	STANDARD		-2.22E-02	2.50E+00	SF5	1.50E+01	0.00E+00	0.00E+00	0.00E+00	0.00E+00	0.00E+00
6	STANDARD		-5.54E-03	0.00E+00		1.50E+01	0.00E+00	0.00E+00	0.00E+00	0.00E+00	0.00E+00
7	STANDARD		0.00E+00	2.22E+01		0.00E+00	0.00E+00	0.00E+00	0.00E+00	0.00E+00	0.00E+00
8	STANDARD	LPX137	2.75E-02	5.20E+00	BK7	1.50E+01	0.00E+00	0.00E+00	0.00E+00	0.00E+00	0.00E+00
9	STANDARD		0.00E+00	0.00E+00		1.50E+01	0.00E+00	0.00E+00	0.00E+00	0.00E+00	0.00E+00
10	STANDARD		0.00E+00	1.15E+01		1.50E+01	0.00E+00	0.00E+00	0.00E+00	0.00E+00	0.00E+00
11	STANDARD		0.00E+00	0.00E+00		1.00E+01	0.00E+00	0.00E+00	0.00E+00	0.00E+00	0.00E+00

Merit Function:

#	Type	Int1	Int2	Hx	Hy	Px	Py	Target	Weight	Value	Contrib
1	COMA	0	1	0.00E+00	0.00E+00	0.00E+00	0.00E+00	0.00E+00	0.00E+00	-1.80E+00	0.00E+00
2	SPHA	0	1	0.00E+00	0.00E+00	0.00E+00	0.00E+00	0.00E+00	0.00E+00	1.27E+00	0.00E+00
3	RANG	11	1	0.00E+00	1.00E+00	0.00E+00	0.00E+00	0.00E+00	1.00E+05	4.79E-03	2.29E-05
4	MNCA	1	10	0.00E+00	0.00E+00	0.00E+00	0.00E+00	5.00E+00	1.00E+05	-5.00E+00	1.00E+02
5	MXCA	1	10	0.00E+00	0.00E+00	0.00E+00	0.00E+00	5.00E+01	1.00E+05	5.00E+01	0.00E+00
6	DMFS	0	0	0.00E+00	0.00E+00	0.00E+00	0.00E+00	0.00E+00	0.00E+00	0.00E+00	0.00E+00
7	BLNK	0	0	0.00E+00	0.00E+00	0.00E+00	0.00E+00	0.00E+00	0.00E+00	0.00E+00	0.00E+00
8	BLNK	0	0	0.00E+00	0.00E+00	0.00E+00	0.00E+00	0.00E+00	0.00E+00	0.00E+00	0.00E+00
9	BLNK	0	0	0.00E+00	0.00E+00	0.00E+00	0.00E+00	0.00E+00	0.00E+00	0.00E+00	0.00E+00
10	BLNK	0	0	0.00E+00	0.00E+00	0.00E+00	0.00E+00	0.00E+00	0.00E+00	0.00E+00	0.00E+00
11	TRAC	0	1	0.00E+00	1.00E+00	1.68E-01	2.91E-01	0.00E+00	2.91E-01	1.02E-02	3.00E-10
12	TRAC	0	1	0.00E+00	1.00E+00	3.54E-01	6.12E-01	0.00E+00	4.65E-01	1.85E-02	1.59E-09
13	TRAC	0	1	0.00E+00	1.00E+00	4.71E-01	8.16E-01	0.00E+00	2.91E-01	2.78E-02	2.24E-09
14	TRAC	0	1	0.00E+00	1.00E+00	3.36E-01	0.00E+00	0.00E+00	2.91E-01	7.14E-03	1.48E-10
15	TRAC	0	1	0.00E+00	1.00E+00	7.07E-01	0.00E+00	0.00E+00	4.65E-01	1.76E-02	1.45E-09
16	TRAC	0	1	0.00E+00	1.00E+00	9.42E-01	0.00E+00	0.00E+00	2.91E-01	3.04E-02	2.68E-09
17	TRAC	0	1	0.00E+00	1.00E+00	1.68E-01	-2.91E-01	0.00E+00	2.91E-01	4.66E-03	6.32E-11
18	TRAC	0	1	0.00E+00	1.00E+00	3.54E-01	-6.12E-01	0.00E+00	4.65E-01	2.25E-02	2.37E-09
19	TRAC	0	1	0.00E+00	1.00E+00	4.71E-01	-8.16E-01	0.00E+00	2.91E-01	4.13E-02	4.97E-09

A.3.2 Denis Laurin Telecentric for Beam Scan System

- Sequential mode
- 457.5 nm wavelength
- Fields: ± 7.03 mm, ±8.82 mm, ±10.63 mm
- Entrance Aperture Diameter: 80 mm

#	Type	Comm	Curvature	Thickness	Glass	Semi-Diameter	Conic	Param 0	Param 1	Param 2	Param 3

0	STANDARD		0.00E+00	5.00E+01		1.06E+01	0.00E+00	0.00E+00	0.00E+00	0.00E+00	0.00E+00
1	PARAXIAL		0.00E+00	5.00E+01		2.56E+01	0.00E+00	0.00E+00	5.00E+01	0.00E+00	0.00E+00
2	STANDARD		0.00E+00	3.00E+01		1.50E+01	0.00E+00	0.00E+00	0.00E+00	0.00E+00	0.00E+00
3	STANDARD		9.45E-03	3.00E+01	BK7	4.50E+01	0.00E+00	0.00E+00	0.00E+00	0.00E+00	0.00E+00
4	STANDARD		-5.53E-03	2.49E+01		4.50E+01	0.00E+00	0.00E+00	0.00E+00	0.00E+00	0.00E+00
5	STANDARD		1.94E-02	3.31E+01	BK7	3.00E+01	0.00E+00	0.00E+00	0.00E+00	0.00E+00	0.00E+00
6	STANDARD		0.00E+00	2.48E+01		3.00E+01	0.00E+00	0.00E+00	0.00E+00	0.00E+00	0.00E+00
7	STANDARD	MIDDLE	0.00E+00	2.48E+01		1.40E+01	0.00E+00	0.00E+00	0.00E+00	0.00E+00	0.00E+00
8	STANDARD		0.00E+00	3.31E+01	BK7	3.00E+01	0.00E+00	0.00E+00	0.00E+00	0.00E+00	0.00E+00
9	STANDARD		-1.94E-02	2.49E+01		3.00E+01	0.00E+00	0.00E+00	0.00E+00	0.00E+00	0.00E+00
10	STANDARD		5.53E-03	3.00E+01	BK7	4.50E+01	0.00E+00	0.00E+00	0.00E+00	0.00E+00	0.00E+00
11	STANDARD		-9.45E-03	3.00E+01		4.50E+01	0.00E+00	0.00E+00	0.00E+00	0.00E+00	0.00E+00
12	STANDARD		0.00E+00	5.00E+01		1.61E+01	0.00E+00	0.00E+00	0.00E+00	0.00E+00	0.00E+00
13	PARAXIAL		0.00E+00	5.00E+01		2.64E+01	0.00E+00	0.00E+00	5.00E+01	0.00E+00	0.00E+00
14	STANDARD	DUMMY	0.00E+00	0.00E+00		1.09E+01	0.00E+00	0.00E+00	0.00E+00	0.00E+00	0.00E+00
15	STANDARD		0.00E+00	0.00E+00		1.09E+01	0.00E+00	0.00E+00	0.00E+00	0.00E+00	0.00E+00

Merit Function:

#	Type	Int1	Int2	Hx	Hy	Px	Py	Target	Weight	Value	Contrib
1	SVIG	0	0	0.00E+00	0.00E+00	0.00E+00	0.00E+00	0.00E+00	0.00E+00	0.00E+00	0.00E+00
2	EFLX	3	7	0.00E+00	0.00E+00	0.00E+00	0.00E+00	6.00E+01	1.00E+00	6.73E+01	5.21E+00
3	EFLY	3	7	0.00E+00	0.00E+00	0.00E+00	0.00E+00	6.00E+01	1.00E+00	6.73E+01	5.21E+00
4	EFLX	7	11	0.00E+00	0.00E+00	0.00E+00	0.00E+00	6.00E+01	1.00E+00	6.73E+01	5.21E+00
5	EFLY	7	11	0.00E+00	0.00E+00	0.00E+00	0.00E+00	6.00E+01	1.00E+00	6.73E+01	5.21E+00
6	MXCG	3	6	0.00E+00	0.00E+00	0.00E+00	0.00E+00	3.00E+01	1.00E+00	3.31E+01	9.14E-01
7	MNCA	4	5	0.00E+00	0.00E+00	0.00E+00	0.00E+00	1.50E+01	1.00E+00	1.50E+01	0.00E+00
8	MXCA	4	5	0.00E+00	0.00E+00	0.00E+00	0.00E+00	2.50E+01	1.00E+00	2.50E+01	0.00E+00
9	MNCA	6	7	0.00E+00	0.00E+00	0.00E+00	0.00E+00	2.50E+01	1.00E+00	2.47E+01	1.16E-02
10	MXCA	6	7	0.00E+00	0.00E+00	0.00E+00	0.00E+00	3.00E+01	1.00E+00	3.00E+01	0.00E+00
11	SPHA	0	1	0.00E+00	0.00E+00	0.00E+00	0.00E+00	0.00E+00	1.00E-04	2.25E+03	4.89E+01
12	COMA	0	1	0.00E+00	0.00E+00	0.00E+00	0.00E+00	0.00E+00	0.00E+00	-2.34E+03	0.00E+00
13	ASTI	0	1	0.00E+00	0.00E+00	0.00E+00	0.00E+00	0.00E+00	0.00E+00	6.42E+02	0.00E+00
14	DMFS	0	0	0.00E+00	0.00E+00	0.00E+00	0.00E+00	0.00E+00	0.00E+00	0.00E+00	0.00E+00
15	BLNK	0	0	0.00E+00	0.00E+00	0.00E+00	0.00E+00	0.00E+00	0.00E+00	0.00E+00	0.00E+00
16	BLNK	0	0	0.00E+00	0.00E+00	0.00E+00	0.00E+00	0.00E+00	0.00E+00	0.00E+00	0.00E+00
17	BLNK	0	0	0.00E+00	0.00E+00	0.00E+00	0.00E+00	0.00E+00	0.00E+00	0.00E+00	0.00E+00
18	BLNK	0	0	0.00E+00	0.00E+00	0.00E+00	0.00E+00	0.00E+00	0.00E+00	0.00E+00	0.00E+00
19	OPDX	0	1	0.00E+00	6.61E-01	1.68E-01	2.91E-01	0.00E+00	4.85E-02	2.20E+01	2.27E+00
20	OPDX	0	1	0.00E+00	6.61E-01	3.54E-01	6.12E-01	0.00E+00	7.76E-02	-4.65E+00	1.62E-01
21	OPDX	0	1	0.00E+00	6.61E-01	4.71E-01	8.16E-01	0.00E+00	4.85E-02	-1.40E+01	9.16E-01
22	OPDX	0	1	0.00E+00	6.61E-01	3.36E-01	0.00E+00	0.00E+00	4.85E-02	2.25E+01	2.38E+00
23	OPDX	0	1	0.00E+00	6.61E-01	7.07E-01	0.00E+00	0.00E+00	7.76E-02	-5.80E+00	2.52E-01
24	OPDX	0	1	0.00E+00	6.61E-01	9.42E-01	0.00E+00	0.00E+00	4.85E-02	-1.74E+01	1.42E+00
25	OPDX	0	1	0.00E+00	6.61E-01	1.68E-01	-2.91E-01	0.00E+00	4.85E-02	2.36E+01	2.61E+00
26	OPDX	0	1	0.00E+00	6.61E-01	3.54E-01	-6.12E-01	0.00E+00	7.76E-02	-3.75E+00	1.06E-01
27	OPDX	0	1	0.00E+00	6.61E-01	4.71E-01	-8.16E-01	0.00E+00	4.85E-02	-1.40E+01	9.20E-01
28	BLNK	0	0	0.00E+00	0.00E+00	0.00E+00	0.00E+00	0.00E+00	0.00E+00	0.00E+00	0.00E+00
29	OPDX	0	1	0.00E+00	8.30E-01	1.68E-01	2.91E-01	0.00E+00	4.85E-02	8.90E+00	3.71E-01

30	OPDX	0	1	0.00E+00	8.30E-01	3.54E-01	6.12E-01	0.00E+00	7.76E-02	-3.63E+00	9.91E-02
31	OPDX	0	1	0.00E+00	8.30E-01	4.71E-01	8.16E-01	0.00E+00	4.85E-02	7.66E-01	2.75E-03
32	OPDX	0	1	0.00E+00	8.30E-01	3.36E-01	0.00E+00	0.00E+00	4.85E-02	8.37E+00	3.29E-01
33	OPDX	0	1	0.00E+00	8.30E-01	7.07E-01	0.00E+00	0.00E+00	7.76E-02	-7.00E+00	3.68E-01
34	OPDX	0	1	0.00E+00	8.30E-01	9.42E-01	0.00E+00	0.00E+00	4.85E-02	-5.22E+00	1.28E-01
35	OPDX	0	1	0.00E+00	8.30E-01	1.68E-01	-2.91E-01	0.00E+00	4.85E-02	8.99E+00	3.79E-01
36	OPDX	0	1	0.00E+00	8.30E-01	3.54E-01	-6.12E-01	0.00E+00	7.76E-02	-4.17E+00	1.30E-01
37	OPDX	0	1	0.00E+00	8.30E-01	4.71E-01	-8.16E-01	0.00E+00	4.85E-02	1.88E+00	1.65E-02
38	BLNK	0	0	0.00E+00	0.00E+00	0.00E+00	0.00E+00	0.00E+00	0.00E+00	0.00E+00	0.00E+00
39	OPDX	0	1	0.00E+00	1.00E+00	1.68E-01	2.91E-01	0.00E+00	4.85E-02	-7.31E+00	2.51E-01
40	OPDX	0	1	0.00E+00	1.00E+00	3.54E-01	6.12E-01	0.00E+00	7.76E-02	-1.69E+00	2.14E-02
41	OPDX	0	1	0.00E+00	1.00E+00	4.71E-01	8.16E-01	0.00E+00	4.85E-02	1.97E+01	1.83E+00
42	OPDX	0	1	0.00E+00	1.00E+00	3.36E-01	0.00E+00	0.00E+00	4.85E-02	-9.86E+00	4.56E-01
43	OPDX	0	1	0.00E+00	1.00E+00	7.07E-01	0.00E+00	0.00E+00	7.76E-02	-9.03E+00	6.11E-01
44	OPDX	0	1	0.00E+00	1.00E+00	9.42E-01	0.00E+00	0.00E+00	4.85E-02	9.57E+00	4.30E-01
45	OPDX	0	1	0.00E+00	1.00E+00	1.68E-01	-2.91E-01	0.00E+00	4.85E-02	-1.02E+01	4.90E-01
46	OPDX	0	1	0.00E+00	1.00E+00	3.54E-01	-6.12E-01	0.00E+00	7.76E-02	-4.89E+00	1.79E-01
47	OPDX	0	1	0.00E+00	1.00E+00	4.71E-01	-8.16E-01	0.00E+00	4.85E-02	2.31E+01	2.49E+00
48	BLNK	0	0	0.00E+00	0.00E+00	0.00E+00	0.00E+00	0.00E+00	0.00E+00	0.00E+00	0.00E+00
49	OPDX	0	1	0.00E+00	-6.61E-01	1.68E-01	2.91E-01	0.00E+00	4.85E-03	2.36E+01	2.61E-01
50	OPDX	0	1	0.00E+00	-6.61E-01	3.54E-01	6.12E-01	0.00E+00	7.76E-03	-3.75E+00	1.06E-02
51	OPDX	0	1	0.00E+00	-6.61E-01	4.71E-01	8.16E-01	0.00E+00	4.85E-03	-1.40E+01	9.20E-02
52	OPDX	0	1	0.00E+00	-6.61E-01	3.36E-01	0.00E+00	0.00E+00	4.85E-03	2.25E+01	2.38E-01
53	OPDX	0	1	0.00E+00	-6.61E-01	7.07E-01	0.00E+00	0.00E+00	7.76E-03	-5.80E+00	2.52E-02
54	OPDX	0	1	0.00E+00	-6.61E-01	9.42E-01	0.00E+00	0.00E+00	4.85E-03	-1.74E+01	1.42E-01
55	OPDX	0	1	0.00E+00	-6.61E-01	1.68E-01	-2.91E-01	0.00E+00	4.85E-03	2.20E+01	2.27E-01
56	OPDX	0	1	0.00E+00	-6.61E-01	3.54E-01	-6.12E-01	0.00E+00	7.76E-03	-4.65E+00	1.62E-02
57	OPDX	0	1	0.00E+00	-6.61E-01	4.71E-01	-8.16E-01	0.00E+00	4.85E-03	-1.40E+01	9.16E-02
58	BLNK	0	0	0.00E+00	0.00E+00	0.00E+00	0.00E+00	0.00E+00	0.00E+00	0.00E+00	0.00E+00
59	OPDX	0	1	0.00E+00	-8.30E-01	1.68E-01	2.91E-01	0.00E+00	4.85E-02	8.99E+00	3.79E-01
60	OPDX	0	1	0.00E+00	-8.30E-01	3.54E-01	6.12E-01	0.00E+00	7.76E-02	-4.17E+00	1.30E-01
61	OPDX	0	1	0.00E+00	-8.30E-01	4.71E-01	8.16E-01	0.00E+00	4.85E-02	1.88E+00	1.65E-02
62	OPDX	0	1	0.00E+00	-8.30E-01	3.36E-01	0.00E+00	0.00E+00	4.85E-02	8.37E+00	3.29E-01
63	OPDX	0	1	0.00E+00	-8.30E-01	7.07E-01	0.00E+00	0.00E+00	7.76E-02	-7.00E+00	3.68E-01
64	OPDX	0	1	0.00E+00	-8.30E-01	9.42E-01	0.00E+00	0.00E+00	4.85E-02	-5.22E+00	1.28E-01
65	OPDX	0	1	0.00E+00	-8.30E-01	1.68E-01	-2.91E-01	0.00E+00	4.85E-02	8.90E+00	3.71E-01
66	OPDX	0	1	0.00E+00	-8.30E-01	3.54E-01	-6.12E-01	0.00E+00	7.76E-02	-3.63E+00	9.91E-02

67	OPDX	0	1	0.00E+00	-8.30E-01	4.71E-01	-8.16E-01	0.00E+00	4.85E-02	7.66E-01	2.75E-03
68	BLNK	0	0	0.00E+00	0.00E+00	0.00E+00	0.00E+00	0.00E+00	0.00E+00	0.00E+00	0.00E+00
69	OPDX	0	1	0.00E+00	1.00E+00	1.68E-01	2.91E-01	0.00E+00	4.85E-02	1.02E+01	4.90E-01
70	OPDX	0	1	0.00E+00	1.00E+00	3.54E-01	6.12E-01	0.00E+00	7.76E-02	4.89E+00	1.79E-01
71	OPDX	0	1	0.00E+00	1.00E+00	4.71E-01	8.16E-01	0.00E+00	4.85E-02	2.31E+01	2.49E+00
72	OPDX	0	1	0.00E+00	1.00E+00	3.36E-01	0.00E+00	0.00E+00	4.85E-02	9.86E+00	4.56E-01
73	OPDX	0	1	0.00E+00	1.00E+00	7.07E-01	0.00E+00	0.00E+00	7.76E-02	9.03E+00	6.11E-01
74	OPDX	0	1	0.00E+00	1.00E+00	9.42E-01	0.00E+00	0.00E+00	4.85E-02	9.57E+00	4.30E-01
75	OPDX	0	1	0.00E+00	1.00E+00	1.68E-01	-2.91E-01	0.00E+00	4.85E-02	7.31E+00	2.51E-01
76	OPDX	0	1	0.00E+00	1.00E+00	3.54E-01	-6.12E-01	0.00E+00	7.76E-02	1.69E+00	2.14E-02
77	OPDX	0	1	0.00E+00	1.00E+00	4.71E-01	-8.16E-01	0.00E+00	4.85E-02	1.97E+01	1.83E+00

A.4 Periscope Lens

- Sequential mode
- Wavelength: 457.5 nm
- Fields: 0°, ±0.5°, ±1.0°, ±2.0°, ±2.25°
- Entrance Aperture Diameter: 40 mm

A.4.1 Scanning Mirror Periscope

#	Type	Com	Curvature	Thickness	Glass	Semi-Diameter	Conic	Param 0	Param 1	Param 2	Param 3
0	STANDARD		0.00E+00	1.00E+10		0.00E+00	0.00E+00	0.00E+00	0.00E+00	0.00E+00	0.00E+00
1	STANDARD		0.00E+00	5.00E+01		2.26E+01	0.00E+00	0.00E+00	0.00E+00	0.00E+00	0.00E+00
2	STANDARD		0.00E+00	7.50E+01		2.00E+01	0.00E+00	0.00E+00	0.00E+00	0.00E+00	0.00E+00
3	EVENASPH		1.75E-02	3.00E+01	BK7	4.50E+01	-6.09E-01	0.00E+00	0.00E+00	0.00E+00	0.00E+00
4	STANDARD		0.00E+00	9.00E+01		4.50E+01	0.00E+00	0.00E+00	0.00E+00	0.00E+00	0.00E+00
5	STANDARD	MIDDLE	0.00E+00	9.00E+01		5.81E+00	0.00E+00	0.00E+00	0.00E+00	0.00E+00	0.00E+00
6	STANDARD		0.00E+00	3.00E+01	BK7	4.50E+01	0.00E+00	0.00E+00	0.00E+00	0.00E+00	0.00E+00
7	EVENASPH		-1.75E-02	7.50E+01		4.50E+01	-6.09E-01	0.00E+00	0.00E+00	0.00E+00	0.00E+00
8	PARAXIAL		0.00E+00	1.00E+02		2.24E+01	0.00E+00	0.00E+00	1.00E+02	0.00E+00	0.00E+00
9	STANDARD	DUMMY	0.00E+00	-9.00E-01		5.62E+00	0.00E+00	0.00E+00	0.00E+00	0.00E+00	0.00E+00
10	STANDARD		0.00E+00	0.00E+00		3.70E+00	0.00E+00	0.00E+00	0.00E+00	0.00E+00	0.00E+00

Merit Function:

#	Type	Int1	Int2	Hx	Hy	Px	Py	Target	Weight	Value	Contrib
1	SVIG	0	0	0.00E+00	0.00E+00	0.00E+00	0.00E+00	0.00E+00	0.00E+00	0.00E+00	0.00E+00
2	EFLX	3	5	0.00E+00	0.00E+00	0.00E+00	0.00E+00	1.15E+02	0.00E+00	1.09E+02	0.00E+00
3	EFLY	3	5	0.00E+00	0.00E+00	0.00E+00	0.00E+00	1.15E+02	0.00E+00	1.09E+02	0.00E+00
4	MXCG	3	4	0.00E+00	0.00E+00	0.00E+00	0.00E+00	3.00E+01	1.00E+00	3.00E+01	0.00E+00
5	MNCA	4	5	0.00E+00	0.00E+00	0.00E+00	0.00E+00	1.25E+02	0.00E+00	5.50E+01	0.00E+00
6	MXCA	4	5	0.00E+00	0.00E+00	0.00E+00	0.00E+00	1.45E+02	0.00E+00	1.45E+02	0.00E+00
7	PMAG	0	1	0.00E+00	0.00E+00	0.00E+00	0.00E+00	-1.00E+00	0.00E+00	0.00E+00	0.00E+00

8	SPHA	0	1	0.00E+00	0.00E+00	0.00E+00	0.00E+00	0.00E+00	1.00E-02	-1.16E+01	6.59E-01
9	COMA	0	1	0.00E+00	0.00E+00	0.00E+00	0.00E+00	0.00E+00	0.00E+00	2.11E+00	0.00E+00
10	ASTI	0	1	0.00E+00	0.00E+00	0.00E+00	0.00E+00	0.00E+00	0.00E+00	3.22E+01	0.00E+00
11	DMFS	0	0	0.00E+00	0.00E+00	0.00E+00	0.00E+00	0.00E+00	0.00E+00	0.00E+00	0.00E+00
12	BLNK	0	0	0.00E+00	0.00E+00	0.00E+00	0.00E+00	0.00E+00	0.00E+00	0.00E+00	0.00E+00
13	BLNK	0	0	0.00E+00	0.00E+00	0.00E+00	0.00E+00	0.00E+00	0.00E+00	0.00E+00	0.00E+00
14	BLNK	0	0	0.00E+00	0.00E+00	0.00E+00	0.00E+00	0.00E+00	0.00E+00	0.00E+00	0.00E+00
15	BLNK	0	0	0.00E+00	0.00E+00	0.00E+00	0.00E+00	0.00E+00	0.00E+00	0.00E+00	0.00E+00
16	OPDX	0	1	0.00E+00	0.00E+00	1.84E-01	0.00E+00	0.00E+00	1.35E-01	2.62E+00	4.49E-01
17	OPDX	0	1	0.00E+00	0.00E+00	4.12E-01	0.00E+00	0.00E+00	2.83E-01	2.64E+00	9.58E-01
18	OPDX	0	1	0.00E+00	0.00E+00	6.17E-01	0.00E+00	0.00E+00	3.67E-01	1.83E+00	5.95E-01
19	OPDX	0	1	0.00E+00	0.00E+00	7.87E-01	0.00E+00	0.00E+00	3.67E-01	-2.97E-01	1.57E-02
20	OPDX	0	1	0.00E+00	0.00E+00	9.11E-01	0.00E+00	0.00E+00	2.83E-01	-3.21E+00	1.42E+00
21	OPDX	0	1	0.00E+00	0.00E+00	9.83E-01	0.00E+00	0.00E+00	1.35E-01	-5.59E+00	2.04E+00
22	BLNK	0	0	0.00E+00	0.00E+00	0.00E+00	0.00E+00	0.00E+00	0.00E+00	0.00E+00	0.00E+00
23	OPDX	0	1	0.00E+00	1.00E+00	4.76E-02	1.77E-01	0.00E+00	2.24E-02	-1.59E+01	2.76E+00
24	OPDX	0	1	0.00E+00	1.00E+00	1.07E-01	3.98E-01	0.00E+00	4.72E-02	-9.10E+00	1.90E+00
25	OPDX	0	1	0.00E+00	1.00E+00	1.60E-01	5.96E-01	0.00E+00	6.12E-02	1.42E+00	5.98E-02
26	OPDX	0	1	0.00E+00	1.00E+00	2.04E-01	7.60E-01	0.00E+00	6.12E-02	1.25E+01	4.64E+00
27	OPDX	0	1	0.00E+00	1.00E+00	2.36E-01	8.80E-01	0.00E+00	4.72E-02	2.14E+01	1.05E+01
28	OPDX	0	1	0.00E+00	1.00E+00	2.54E-01	9.49E-01	0.00E+00	2.24E-02	2.67E+01	7.75E+00
29	OPDX	0	1	0.00E+00	1.00E+00	1.30E-01	1.30E-01	0.00E+00	2.24E-02	-1.62E+01	2.87E+00
30	OPDX	0	1	0.00E+00	1.00E+00	2.91E-01	2.91E-01	0.00E+00	4.72E-02	-1.12E+01	2.89E+00
31	OPDX	0	1	0.00E+00	1.00E+00	4.36E-01	4.36E-01	0.00E+00	6.12E-02	-3.70E+00	4.08E-01
32	OPDX	0	1	0.00E+00	1.00E+00	5.56E-01	5.56E-01	0.00E+00	6.12E-02	3.86E+00	4.43E-01
33	OPDX	0	1	0.00E+00	1.00E+00	6.44E-01	6.44E-01	0.00E+00	4.72E-02	9.63E+00	2.13E+00
34	OPDX	0	1	0.00E+00	1.00E+00	6.95E-01	6.95E-01	0.00E+00	2.24E-02	1.29E+01	1.80E+00
35	OPDX	0	1	0.00E+00	1.00E+00	1.77E-01	4.76E-02	0.00E+00	2.24E-02	-1.64E+01	2.94E+00
36	OPDX	0	1	0.00E+00	1.00E+00	3.98E-01	1.07E-01	0.00E+00	4.72E-02	-1.31E+01	3.94E+00
37	OPDX	0	1	0.00E+00	1.00E+00	5.96E-01	1.60E-01	0.00E+00	6.12E-02	-8.54E+00	2.17E+00
38	OPDX	0	1	0.00E+00	1.00E+00	7.60E-01	2.04E-01	0.00E+00	6.12E-02	-4.47E+00	5.96E-01
39	OPDX	0	1	0.00E+00	1.00E+00	8.80E-01	2.36E-01	0.00E+00	4.72E-02	-1.85E+00	7.88E-02
40	OPDX	0	1	0.00E+00	1.00E+00	9.49E-01	2.54E-01	0.00E+00	2.24E-02	-6.52E-01	4.63E-03
41	OPDX	0	1	0.00E+00	1.00E+00	1.77E-01	-4.76E-02	0.00E+00	2.24E-02	-1.61E+01	2.83E+00
42	OPDX	0	1	0.00E+00	1.00E+00	3.98E-01	-1.07E-01	0.00E+00	4.72E-02	-1.25E+01	3.60E+00
43	OPDX	0	1	0.00E+00	1.00E+00	5.96E-01	-1.60E-01	0.00E+00	6.12E-02	-7.92E+00	1.86E+00
44	OPDX	0	1	0.00E+00	1.00E+00	7.60E-01	-2.04E-01	0.00E+00	6.12E-02	-3.96E+00	4.67E-01
45	OPDX	0	1	0.00E+00	1.00E+00	8.80E-01	-2.36E-01	0.00E+00	4.72E-02	-1.50E+00	5.14E-02
46	OPDX	0	1	0.00E+00	1.00E+00	9.49E-01	-2.54E-01	0.00E+00	2.24E-02	-4.02E-01	1.76E-03
47	OPDX	0	1	0.00E+00	1.00E+00	1.30E-01	-1.30E-01	0.00E+00	2.24E-02	-1.54E+01	2.58E+00
48	OPDX	0	1	0.00E+00	1.00E+00	2.91E-01	-2.91E-	0.00E+00	4.72E-02	-	2.15E+00

							01			9.69E+00	
49	OPDX	0	1	0.00E+00	1.00E+00	4.36E-01	-4.36E-01	0.00E+00	6.12E-02	-2.14E+00	1.36E-01
50	OPDX	0	1	0.00E+00	1.00E+00	5.56E-01	-5.56E-01	0.00E+00	6.12E-02	4.96E+00	7.32E-01
51	OPDX	0	1	0.00E+00	1.00E+00	6.44E-01	-6.44E-01	0.00E+00	4.72E-02	1.01E+01	2.36E+00
52	OPDX	0	1	0.00E+00	1.00E+00	6.95E-01	-6.95E-01	0.00E+00	2.24E-02	1.30E+01	1.83E+00
53	OPDX	0	1	0.00E+00	1.00E+00	4.76E-02	-1.77E-01	0.00E+00	2.24E-02	-1.48E+01	2.38E+00
54	OPDX	0	1	0.00E+00	1.00E+00	1.07E-01	-3.98E-01	0.00E+00	4.72E-02	-7.07E+00	1.15E+00
55	OPDX	0	1	0.00E+00	1.00E+00	1.60E-01	-5.96E-01	0.00E+00	6.12E-02	3.36E+00	3.35E-01
56	OPDX	0	1	0.00E+00	1.00E+00	2.04E-01	-7.60E-01	0.00E+00	6.12E-02	1.36E+01	5.50E+00
57	OPDX	0	1	0.00E+00	1.00E+00	2.36E-01	-8.80E-01	0.00E+00	4.72E-02	2.15E+01	1.06E+01
58	OPDX	0	1	0.00E+00	1.00E+00	2.54E-01	-9.49E-01	0.00E+00	2.24E-02	2.61E+01	7.40E+00

A.4.2 Optical Loop Periscope

#	Type	Comm	Curvature	Thickness	Glass	Semi-Diameter	Conic	Param 0	Param 1	Param 2	Param 3
0	STANDARD		0.00E+00	1.00E+10		0.00E+00	0.00E+00	0.00E+00	0.00E+00	0.00E+00	0.00E+00
1	STANDARD		0.00E+00	5.00E+01		2.26E+01	0.00E+00	0.00E+00	0.00E+00	0.00E+00	0.00E+00
2	STANDARD		0.00E+00	2.56E+02		2.00E+01	0.00E+00	0.00E+00	0.00E+00	0.00E+00	0.00E+00
3	EVENASPH		1.18E-02	2.00E+01	BK7	4.50E+01	-6.61E-01	0.00E+00	0.00E+00	0.00E+00	0.00E+00
4	STANDARD		0.00E+00	1.50E+02		4.50E+01	0.00E+00	0.00E+00	0.00E+00	0.00E+00	0.00E+00
5	STANDARD	MIDDLE	0.00E+00	1.50E+02		8.62E+00	0.00E+00	0.00E+00	0.00E+00	0.00E+00	0.00E+00
6	STANDARD		0.00E+00	2.00E+01	BK7	4.50E+01	0.00E+00	0.00E+00	0.00E+00	0.00E+00	0.00E+00
7	EVENASPH		-1.18E-02	2.56E+02		4.50E+01	-6.61E-01	0.00E+00	0.00E+00	0.00E+00	0.00E+00
8	PARAXIAL		0.00E+00	1.00E+02		3.06E+01	0.00E+00	0.00E+00	1.00E+02	0.00E+00	0.00E+00
9	STANDARD	DUMMY	0.00E+00	-9.00E-01		5.48E+00	0.00E+00	0.00E+00	0.00E+00	0.00E+00	0.00E+00
10	STANDARD		0.00E+00	0.00E+00		3.70E+00	0.00E+00	0.00E+00	0.00E+00	0.00E+00	0.00E+00

Merit Function:

#	Type	Int1	Int2	Hx	Hy	Px	Py	Target	Weight	Value	Contrib
1	SVIG	0	0	0.00E+00	0.00E+00	0.00E+00	0.00E+00	0.00E+00	0.00E+00	0.00E+00	0.00E+00
2	EFLX	3	5	0.00E+00	0.00E+00	0.00E+00	0.00E+00	1.50E+02	0.00E+00	1.62E+02	0.00E+00
3	EFLY	3	5	0.00E+00	0.00E+00	0.00E+00	0.00E+00	1.50E+02	0.00E+00	1.62E+02	0.00E+00
4	MXCG	3	4	0.00E+00	0.00E+00	0.00E+00	0.00E+00	3.00E+01	1.00E+00	3.00E+01	0.00E+00
5	MNCA	4	5	0.00E+00	0.00E+00	0.00E+00	0.00E+00	1.25E+02	0.00E+00	1.25E+02	0.00E+00
6	MXCA	4	5	0.00E+00	0.00E+00	0.00E+00	0.00E+00	1.45E+02	0.00E+00	1.55E+02	0.00E+00
7	PMAG	0	1	0.00E+00	0.00E+00	0.00E+00	0.00E+00	-1.00E+00	0.00E+00	0.00E+00	0.00E+00
8	SPHA	0	1	0.00E+00	0.00E+00	0.00E+00	0.00E+00	0.00E+00	1.00E-02	-6.35E+00	7.12E+00
9	COMA	0	1	0.00E+00	0.00E+00	0.00E+00	0.00E+00	0.00E+00	0.00E+00	-7.52E+00	0.00E+00
10	ASTI	0	1	0.00E+00	0.00E+00	0.00E+00	0.00E+00	0.00E+00	0.00E+00	1.70E+01	0.00E+00
11	DMFS	0	0	0.00E+00	0.00E+00	0.00E+00	0.00E+00	0.00E+00	0.00E+00	0.00E+00	0.00E+00
12	BLNK	0	0	0.00E+00	0.00E+00	0.00E+00	0.00E+00	0.00E+00	0.00E+00	0.00E+00	0.00E+00
13	BLNK	0	0	0.00E+00	0.00E+00	0.00E+00	0.00E+00	0.00E+00	0.00E+00	0.00E+00	0.00E+00
14	BLNK	0	0	0.00E+00	0.00E+00	0.00E+00	0.00E+00	0.00E+00	0.00E+00	0.00E+00	0.00E+00

15	BLNK	0	0	0.00E+00	0.00E+00	0.00E+00	0.00E+00	0.00E+00	0.00E+00	0.00E+00	0.00E+00
16	OPDX	0	1	0.00E+00	0.00E+00	3.36E-01	0.00E+00	0.00E+00	2.49E-01	6.82E-01	2.05E+00
17	OPDX	0	1	0.00E+00	0.00E+00	7.07E-01	0.00E+00	0.00E+00	3.99E-01	5.28E-01	1.96E+00
18	OPDX	0	1	0.00E+00	0.00E+00	9.42E-01	0.00E+00	0.00E+00	2.49E-01	-1.53E+00	1.03E+01
19	BLNK	0	0	0.00E+00	0.00E+00	0.00E+00	0.00E+00	0.00E+00	0.00E+00	0.00E+00	0.00E+00
20	OPDX	0	1	0.00E+00	1.67E-01	1.68E-01	2.91E-01	0.00E+00	6.23E-02	6.70E-01	4.94E-01
21	OPDX	0	1	0.00E+00	1.67E-01	3.54E-01	6.12E-01	0.00E+00	9.97E-02	7.20E-01	9.12E-01
22	OPDX	0	1	0.00E+00	1.67E-01	4.71E-01	8.16E-01	0.00E+00	6.23E-02	-1.43E+00	2.24E+00
23	OPDX	0	1	0.00E+00	1.67E-01	3.36E-01	0.00E+00	0.00E+00	6.23E-02	4.24E-01	1.98E-01
24	OPDX	0	1	0.00E+00	1.67E-01	7.07E-01	0.00E+00	0.00E+00	9.97E-02	4.13E-01	3.00E-01
25	OPDX	0	1	0.00E+00	1.67E-01	9.42E-01	0.00E+00	0.00E+00	6.23E-02	-1.50E+00	2.47E+00
26	OPDX	0	1	0.00E+00	1.67E-01	1.68E-01	-2.91E-01	0.00E+00	6.23E-02	2.58E-01	7.31E-02
27	OPDX	0	1	0.00E+00	1.67E-01	3.54E-01	-6.12E-01	0.00E+00	9.97E-02	4.54E-01	3.63E-01
28	OPDX	0	1	0.00E+00	1.67E-01	4.71E-01	-8.16E-01	0.00E+00	6.23E-02	-9.62E-01	1.02E+00
29	BLNK	0	0	0.00E+00	0.00E+00	0.00E+00	0.00E+00	0.00E+00	0.00E+00	0.00E+00	0.00E+00
30	OPDX	0	1	0.00E+00	3.33E-01	1.68E-01	2.91E-01	0.00E+00	4.16E-02	2.18E-01	3.50E-02
31	OPDX	0	1	0.00E+00	3.33E-01	3.54E-01	6.12E-01	0.00E+00	6.65E-02	1.03E+00	1.24E+00
32	OPDX	0	1	0.00E+00	3.33E-01	4.71E-01	8.16E-01	0.00E+00	4.16E-02	-6.66E-01	3.25E-01
33	OPDX	0	1	0.00E+00	3.33E-01	3.36E-01	0.00E+00	0.00E+00	4.16E-02	-3.52E-01	9.10E-02
34	OPDX	0	1	0.00E+00	3.33E-01	7.07E-01	0.00E+00	0.00E+00	6.65E-02	6.56E-02	5.04E-03
35	OPDX	0	1	0.00E+00	3.33E-01	9.42E-01	0.00E+00	0.00E+00	4.16E-02	-1.42E+00	1.48E+00
36	OPDX	0	1	0.00E+00	3.33E-01	1.68E-01	-2.91E-01	0.00E+00	4.16E-02	-6.03E-01	2.66E-01
37	OPDX	0	1	0.00E+00	3.33E-01	3.54E-01	-6.12E-01	0.00E+00	6.65E-02	5.02E-01	2.96E-01
38	OPDX	0	1	0.00E+00	3.33E-01	4.71E-01	-8.16E-01	0.00E+00	4.16E-02	2.69E-01	5.32E-02
39	BLNK	0	0	0.00E+00	0.00E+00	0.00E+00	0.00E+00	0.00E+00	0.00E+00	0.00E+00	0.00E+00
40	OPDX	0	1	0.00E+00	5.00E-01	1.68E-01	2.91E-01	0.00E+00	4.16E-02	-6.77E-01	3.36E-01
41	OPDX	0	1	0.00E+00	5.00E-01	3.54E-01	6.12E-01	0.00E+00	6.65E-02	1.45E+00	2.48E+00
42	OPDX	0	1	0.00E+00	5.00E-01	4.71E-01	8.16E-01	0.00E+00	4.16E-02	7.68E-01	4.33E-01
43	OPDX	0	1	0.00E+00	5.00E-01	3.36E-01	0.00E+00	0.00E+00	4.16E-02	-1.65E+00	2.00E+00
44	OPDX	0	1	0.00E+00	5.00E-01	7.07E-01	0.00E+00	0.00E+00	6.65E-02	-5.18E-01	3.15E-01
45	OPDX	0	1	0.00E+00	5.00E-01	9.42E-01	0.00E+00	0.00E+00	4.16E-02	-1.30E+00	1.23E+00
46	OPDX	0	1	0.00E+00	5.00E-01	1.68E-01	-2.91E-01	0.00E+00	4.16E-02	-1.90E+00	2.65E+00
47	OPDX	0	1	0.00E+00	5.00E-01	3.54E-01	-6.12E-01	0.00E+00	6.65E-02	6.76E-01	5.37E-01
48	OPDX	0	1	0.00E+00	5.00E-01	4.71E-01	-8.16E-01	0.00E+00	4.16E-02	2.18E+00	3.47E+00
49	BLNK	0	0	0.00E+00	0.00E+00	0.00E+00	0.00E+00	0.00E+00	0.00E+00	0.00E+00	0.00E+00
50	OPDX	0	1	0.00E+00	6.67E-01	1.68E-01	2.91E-01	0.00E+00	4.16E-02	-2.02E+00	3.00E+00
51	OPDX	0	1	0.00E+00	6.67E-01	3.54E-01	6.12E-01	0.00E+00	6.65E-02	2.00E+00	4.69E+00
52	OPDX	0	1	0.00E+00	6.67E-01	4.71E-01	8.16E-01	0.00E+00	4.16E-02	2.88E+00	6.10E+00
53	OPDX	0	1	0.00E+00	6.67E-01	3.36E-01	0.00E+00	0.00E+00	4.16E-02	-3.48E+00	8.88E+00
54	OPDX	0	1	0.00E+00	6.67E-01	7.07E-01	0.00E+00	0.00E+00	6.65E-02	-1.35E+00	2.13E+00
55	OPDX	0	1	0.00E+00	6.67E-01	9.42E-01	0.00E+00	0.00E+00	4.16E-02	-	9.41E-01

										1.13E+00	
56	OPDX	0	1	0.00E+00	6.67E-01	1.68E-01	-2.91E-01	0.00E+00	4.16E-02	-3.64E+00	9.71E+00
57	OPDX	0	1	0.00E+00	6.67E-01	3.54E-01	-6.12E-01	0.00E+00	6.65E-02	9.83E-01	1.13E+00
58	OPDX	0	1	0.00E+00	6.67E-01	4.71E-01	-8.16E-01	0.00E+00	4.16E-02	4.77E+00	1.67E+01

A.5 Projector Lens Test Configuration

- Non-sequential Mode

Object #	Object Type	Comment	Ref Object	Inside Of	X Position	Y Position	Z Position
1	Source Point	OBJECT	0	0	0	8	0
2	Source Point	REFERENCE	0	0	0	-8	0
3	Poly Object Standard	PRISM07-5.POB	0	0	0	0	60
4	Lens		0	0	0	0	70
5	Detector Rect	CCD	0	0	0	0	205

Object #	Tilt About X	Tilt About Y	Tilt About Z	Material	Param 1	Param 2
1	0	0	0	-	1000	100000
2	0	0	0	-	1000	100000
3	0	0	0	BK7	17.5	1
4	0	0	0	BK7	-200	0
5	0	0	0	ABSORB	28	28

Object #	Param 3	Param 4	Param 5	Param 6	Param 7	Param 8	Param 9
1	0.05	0	0	7			
2	0.05	0	0	7			
3							
4	25	25	1	0	0	25	25
5	500	500	1	2	0	0	0

A.6 Coatings

Append to Coatings\COATING.DAT:

! Sample of defining ideal coatings using IDEAL. Defines transmitted and reflected intensity, rest is assumed to be absorbed
! Format: IDEAL <name> <Transmitted intensity> <Reflected intensity>

IDEAL SPLIT 0.50 0.50
IDEAL PAR 1.00 0.00

! Sample of defining ideal coatings using IDEAL2. Defines reflected and transmitted complex amplitude for S and P, rest is assumed to be absorbed
! Format: IDEAL <name> s_rr s_ri s_tr s_ti p_rr p_ri p_tr p_ti no_pi_flag

IDEAL2 PASS_P 1.0 0.0 0.0 0.0 0.0 0.0 1.0 0.0 0
IDEAL2 PASS_S 0.0 0.0 1.0 0.0 1.0 0.0 0.0 0.0 0

A.7 Poly Objects

Beamsplitter Cube

(in Objects/beamsplitcube.pob):

```
! A 45 ^ prism suitable for constructing a beamsplitter
! R. McLeod October 17, 2004
! Vertices
V 1 -0.5 -0.5 -0.5
V 2 -0.5 -0.5 0.5
V 3 -0.5 0.5 -0.5
V 4 -0.5 0.5 0.5
V 5 0.5 -0.5 -0.5
V 6 0.5 -0.5 0.5
! front square face
R 1 2 6 5 0 1
! left side square face
R 1 2 4 3 0 1
! diagonal face
R 3 4 6 5 0 2
! top triangular face
T 2 4 6 0 3
! bottom triangular face
T 1 3 5 0 3
!coatings
C 1 "Side faces"
C 2 "Splitter surface"
C 3 "Triangular tops"
```

Fresnel Biprism (17.5°)

in Objects/prism17-5.pob:

```
! 17.5 deg rectangular prism
! R. McLeod October 8, 2003
! side 1 vertices
V 1  -2 -2   0
V 2  -2  0  -0.63059757775796703535412986345174
V 3  -2  2   0
! side 2 vertices
V 4   2  -2  0
V 5   2   0 -0.63059757775796703535412986345174
V 6   2   2  0
! Coating groups
C 0 "Left (split) side"
C 1 "Right (large) side"
C 2 "Triangular tops"
```

```
! top left
R 2 5 6 3 0 0
! bottom left
R 1 4 5 2 0 0
! right
R 1 3 6 4 0 1
! side 1
T 1 2 3 0 2
! side 2
T 4 5 6 0 2
```

Appendix B – Vibration Analysis Experimental Procedure

B.1 Apparatus

This experiment was conducted to take simultaneous accelerometer measurements of the Newport RS4000 optical table located in ELW B118 and the floor. B118 was the original location of the optical table before the contamination accident. This experiment was performed on a Saturday so that the machine shop and construction of the adjacent building would not influence the floor vibration measurements. Fortunately the new laboratory location is not collocated with the machine shop and construction on the adjacent building is nearly completed so such issues should not appear in the future.

The system used a pair of Vibrametrics M1030 accelerometers. These are seismic grade accelerometers with a sensitivity of approximately 7.0 V/g. For this experiment they were not calibrated since we are only interested in the relative measurement and statistical analysis of their output.

Accelerometer #1 was unit S/N 1508. It was positioned on the table surface in hole BF50. Accelerometer #2 was unit S/N 1553, placed on the floor directly underneath unit #1. Both accelerometers were powered by a dual M8348 op-amp system with a gain of 2500 +/- 5 %. Assistance in the design of the electronics was provided by fellow graduate student Peter Jacquemin. The circuit has a low-pass filter in it to filter out signals below 0.17 Hz. Since the power supply consists of two Duracell batteries the circuit noise should have been very low at the frequencies of interest, 0.1 – 500 Hz.

The amp output to a Digital Translation 9802 DAQ board, with accelerometer #1 using channel 0 and accelerometer #2 using channel 1, both in differential mode. The board acquired at a rate of 2 kHz, which is well above the maximum frequency response of the accelerometers (about 500 Hz). Data was acquired for 10 s to insure consistence when the power spectrum estimates were made. The data was then processed digitally in MATLAB Release 14.

B.2 MATLAB Code

```
load corr1.txt –ascii
t = corr1(:,1:1);
```

```
V0 = corr1(:,2:2);
V1 = corr1(:,3:3);
```

First the data is loaded into MATLAB from an ASCII text file produced by the Data Translation Scope software.

```
V0 = V0 – mean(V0);
V1 = V1 – mean(V1);
```

Then the data is made into a zero mean process to facilitate data analysis.

```
gamma_V0 = xcov(V0);
gamma_V0 = gamma_V0(20000:39999);
gamma_V1 = xcov(V1);
gamma_V1 = gamma_V1(20000:39999);
```

This code computes the autocorrelation for V_0 and V_1. Since the autocorrelation is two-sided and we are only really interested in positive time values (since it is symmetric).

```
gamma_V0V1 = xcov(V0,V1);
gamma_V0V1 = gamma_V0V1(20000:39999);
```

The cross-correlation between V_0 and V_1 is similar to above.

```
[P_V0, F] = periodogram(V0,[],[], 2000);
P_V1 = periodogram(V1);
```

This code computes the power spectrum densities for V_0 and V_1, using the periodogram. Since the data set is quite long (10 seconds) compared to the sample period, the consistency of the periodogram should be very good.

```
P_V0V1 = cpsd(V0,V1,[],[],[],2000);
```

And finally we compute the cross power spectrum density between V_0 and V_1.

Appendix C – Descriptive Statistical Maps

C.1 Normal (Gaussian) Distribution

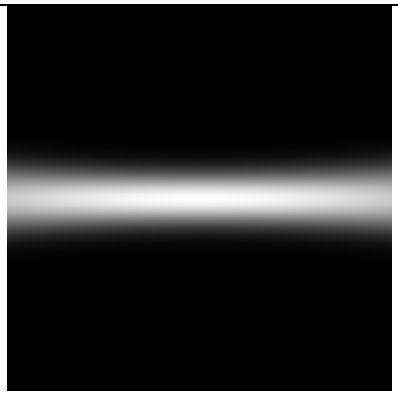
Mean

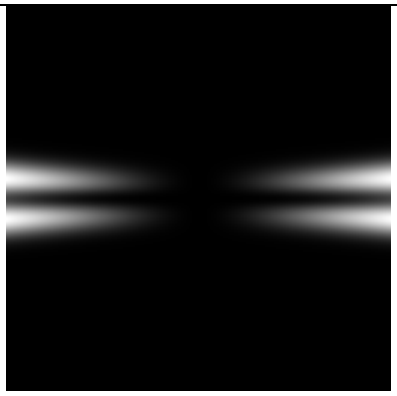
Variance

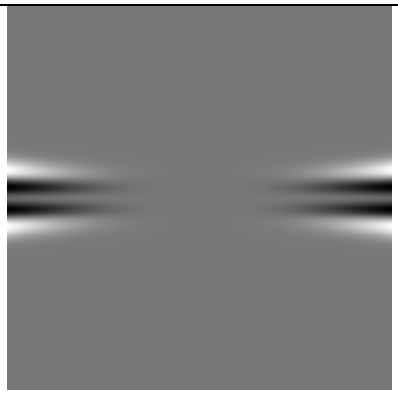
Skewness

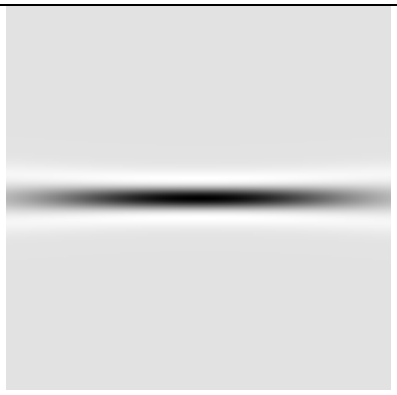
Kurtosis

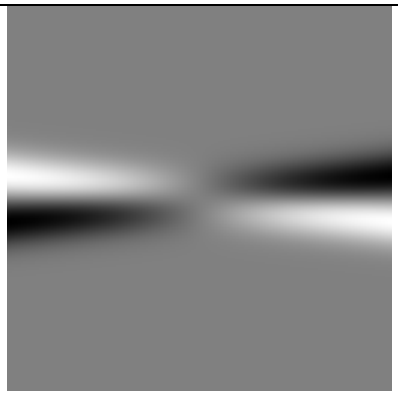
1st Derivative Mean

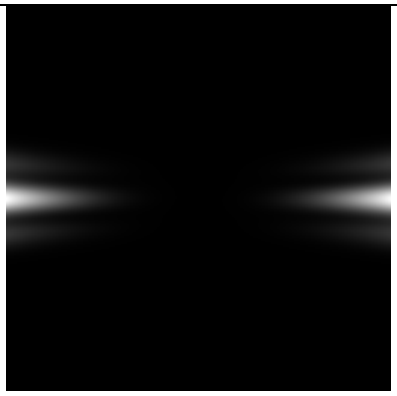
1st Derivative Variance

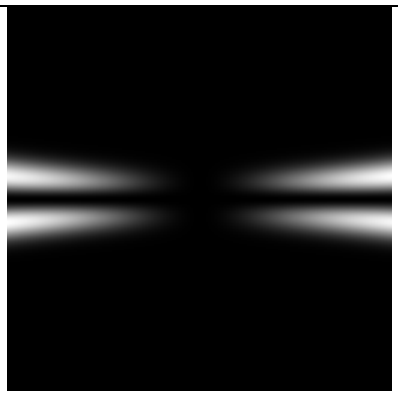

1st Derivative Skewness

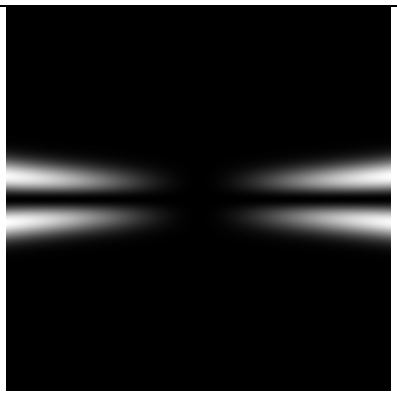

1st Derivative Kurtosis

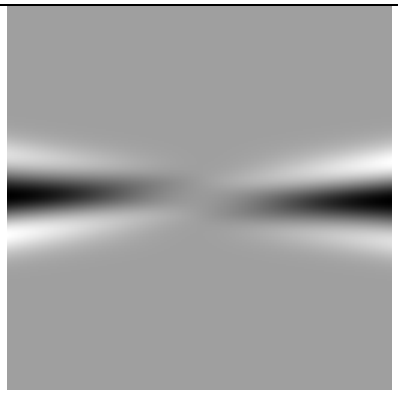

2nd Derivative Mean

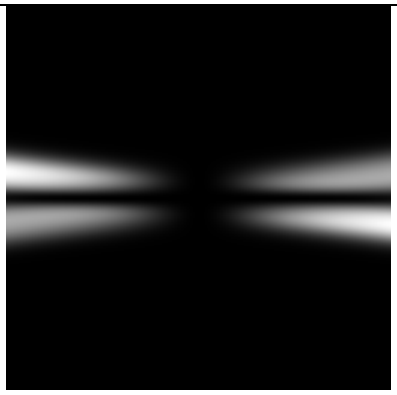

2nd Derivative Variance

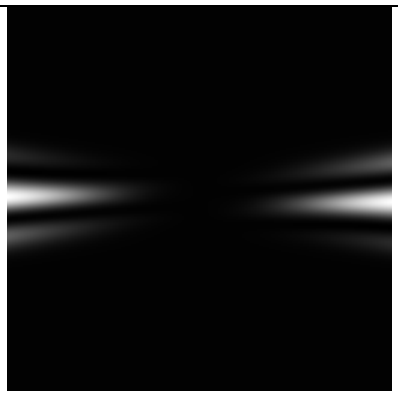

2nd Derivative Skewness

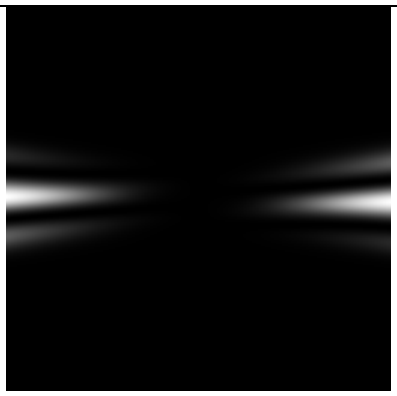

2nd Derivative Kurtosis

Mean Normalized by Variance

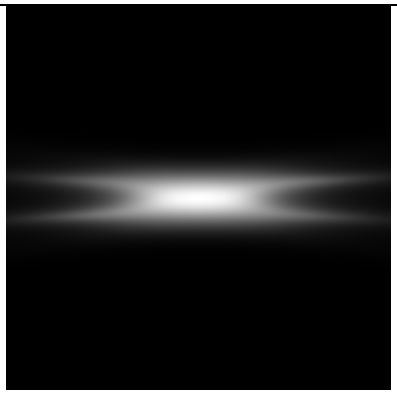

Mean Normalized by 1st Derivative Variance

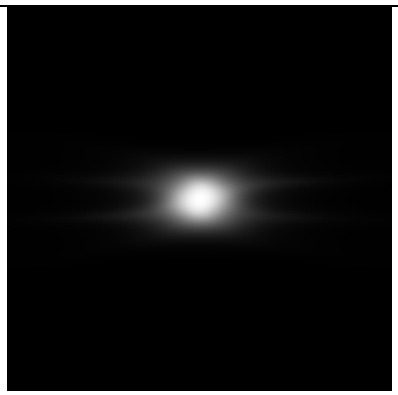

Mean Normalized by Variance Sum

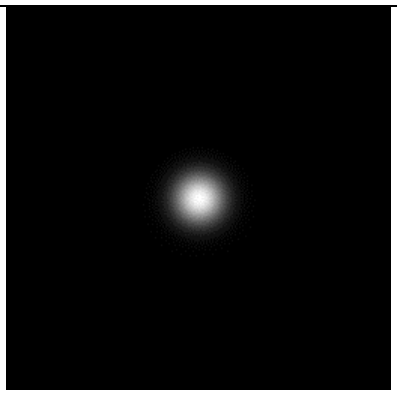

Original Index Map

For a normal (i.e. Gaussian) distribution the most interesting statistics appear to be the variance, the 1st derivative variance, and the kurtosis. The morphology of the absolute value of the skewness is similar to that of the variance. It is possible that the negative value regions of the skewness may hold some useful information. Most of the upper derivative statistical moments do not appear to contain any additional information.

C.2 *Peaks* Distribution

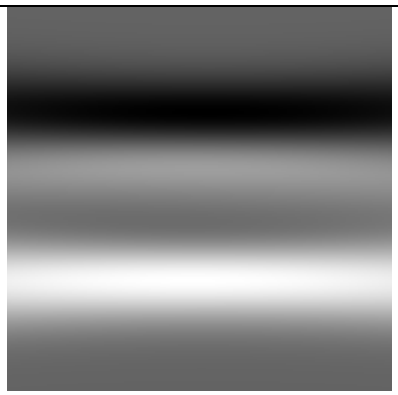

Mean

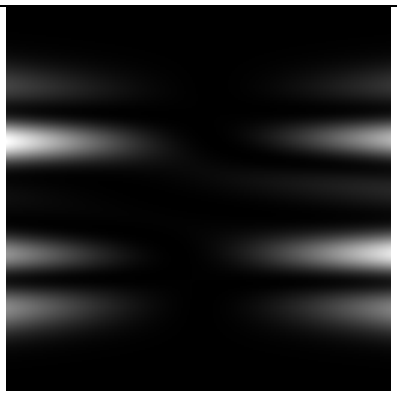

Variance

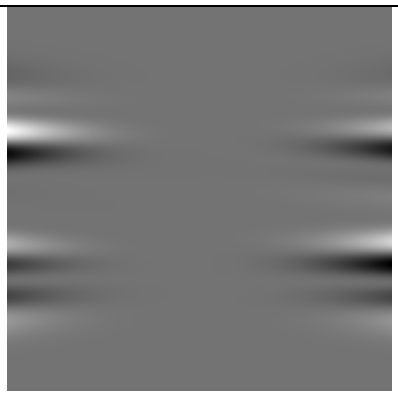

Skewness

Kurtosis

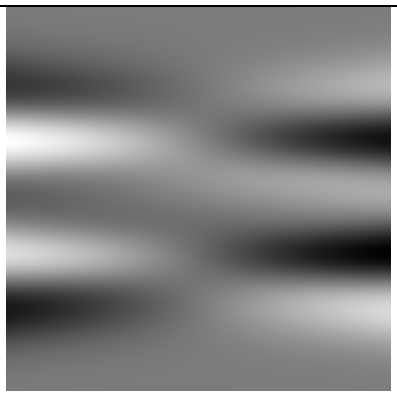

1st Derivative Mean

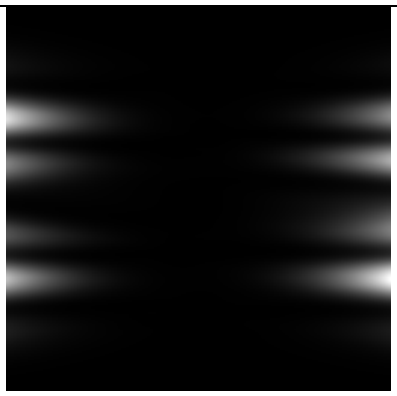

1st Derivative Variance

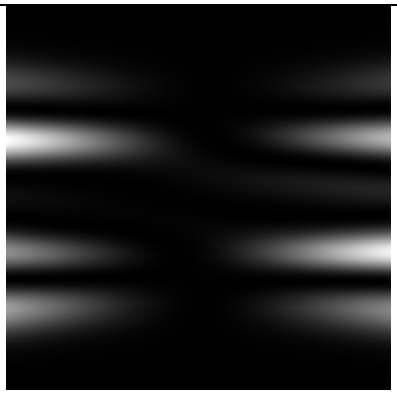

1st Derivative Skewness

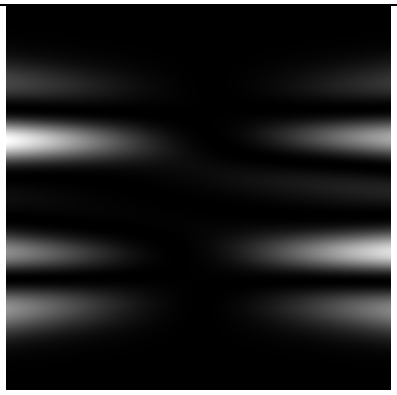

1st Derivative Kurtosis

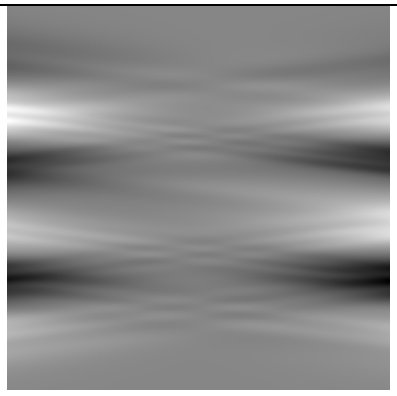

2nd Derivative Mean

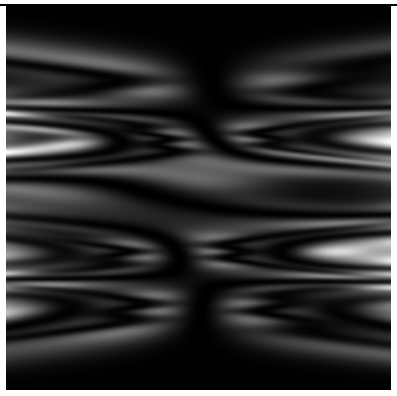

2nd Derivative Variance

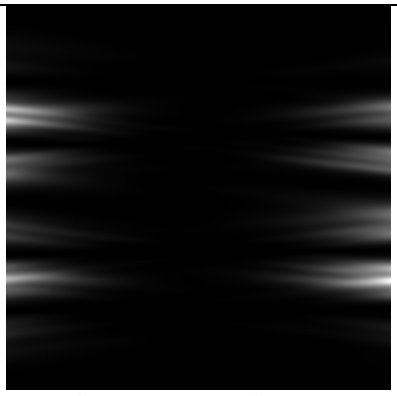

2nd Derivative Skewness

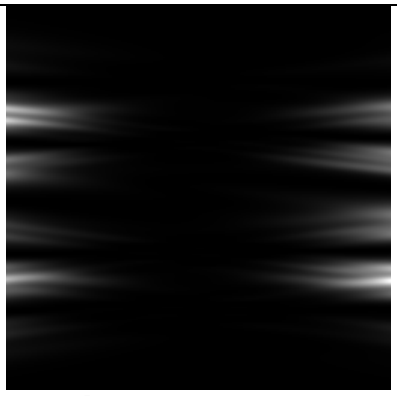

2nd Derivative Kurtosis

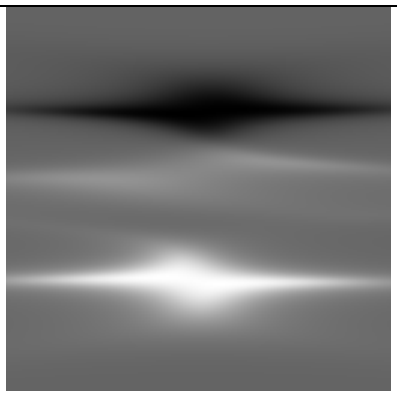

Mean Normalized by Variance

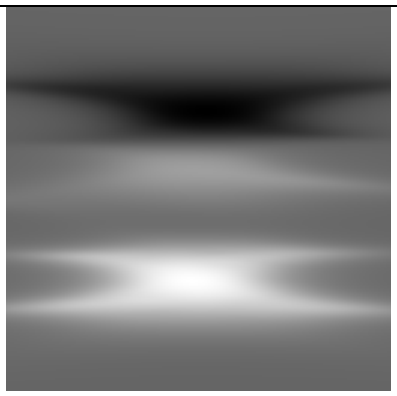

Mean Normalized by 1st Derivative Variance

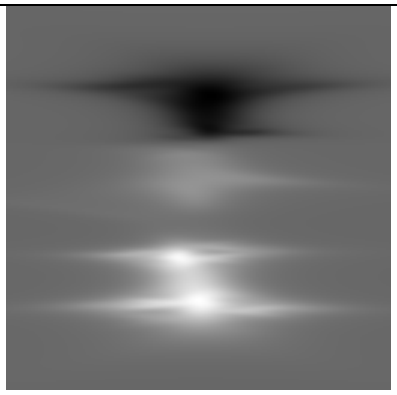

Mean Normalized by Variance Sum

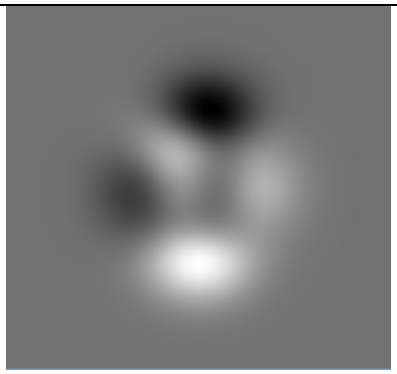

Original Index Map

Peaks is a much more complex object since it is composed of a superposition of multiple Gaussian functions and additional simple functions. As such additional information manifests itself in the higher derivative moments. The difference between the 2nd derivative variance for *Peaks* and a vanilla normal distribution is striking.

C.3 Cylindrical (Disk) Distribution

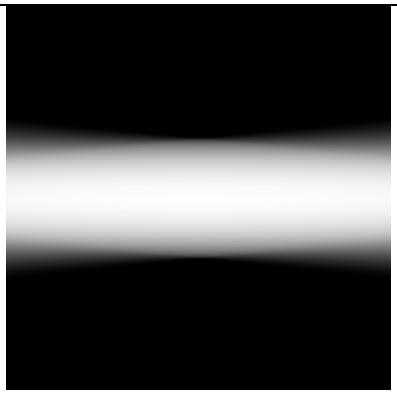

Mean

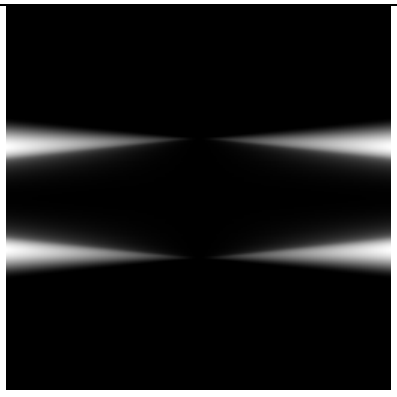

Variance

Skewness

Kurtosis

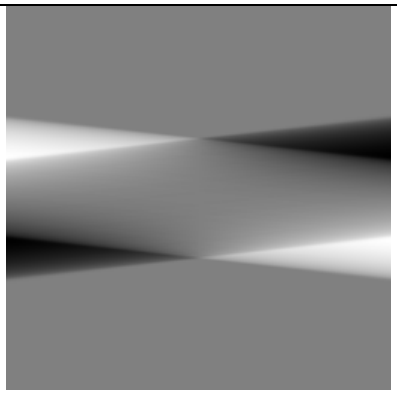

1st Derivative Mean

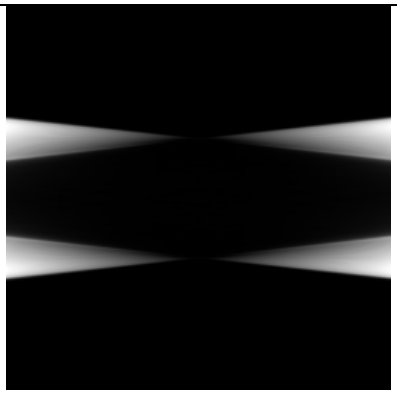

1st Derivative Variance

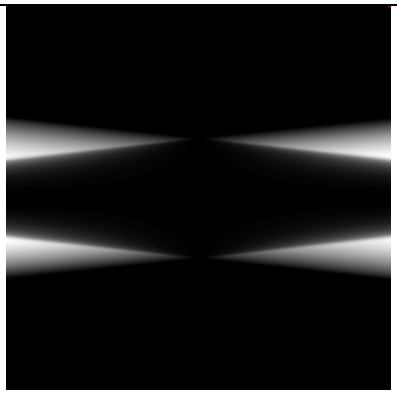

1st Derivative Skewness

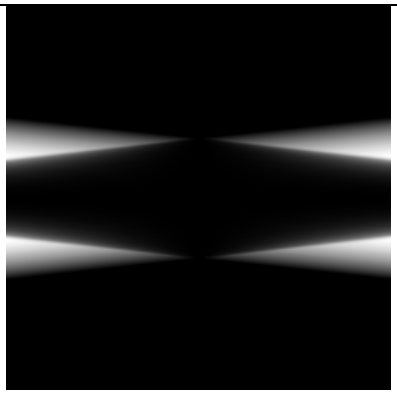

1st Derivative Kurtosis

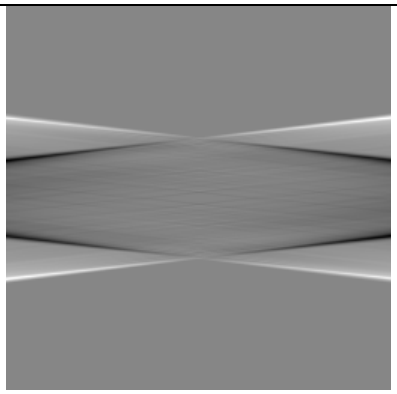

2nd Derivative Mean

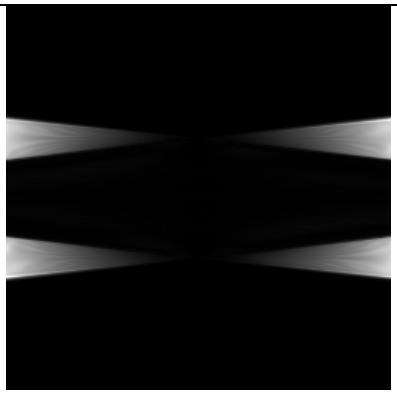

2nd Derivative Variance

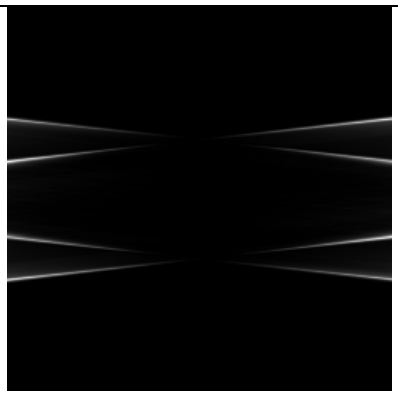

2nd Derivative Skewness

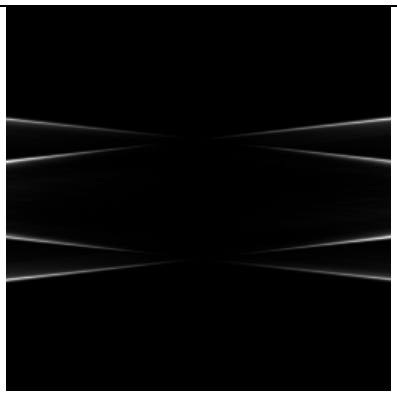

2nd Derivative Kurtosis

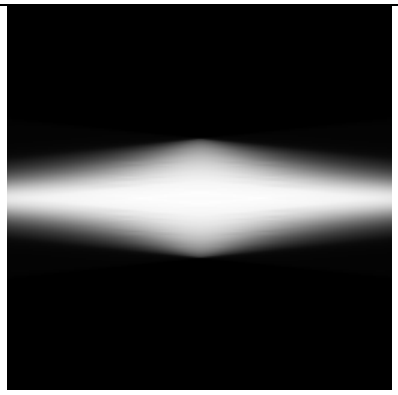

Mean Normalized by Variance

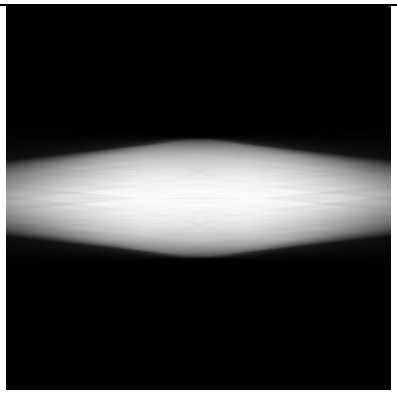

Mean Normalized by 1st Derivative Variance

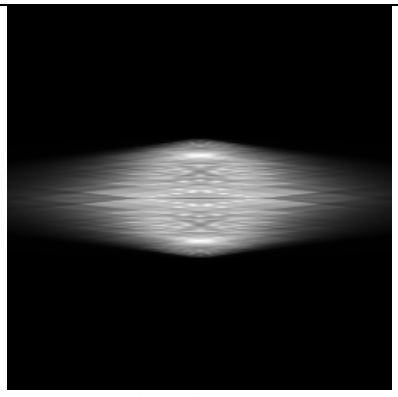

Mean Normalized by Variance Sum

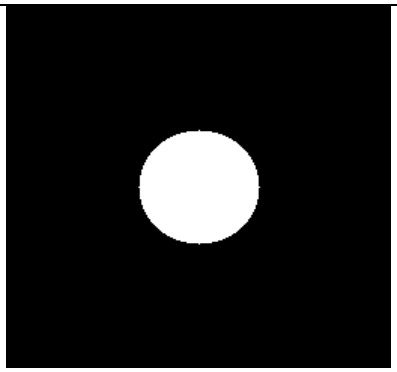

Original Index Map

The cylindrical (or disk) distribution is representative of a discontinuity such as a bubble. The limitations of the marginal rays to isolate this cylindrical object are quite obvious by observation of the variance. It is important to note that the index map contains a much larger object than was the case for the normal distribution. However the method of descriptive statistics seems less suitable than the incremental correction method.

C.4 Gradient X-Z Distribution

 Mean	 Variance
 Skewness	 Kurtosis
 1st Derivative Mean	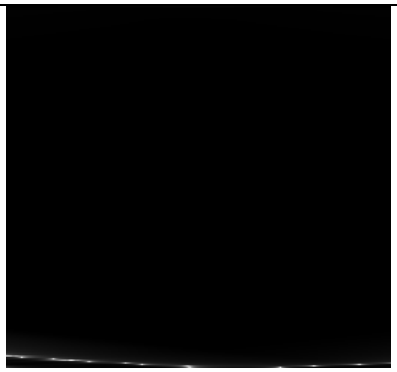 1st Derivative Variance
 1st Derivative Skewness	 1st Derivative Kurtosis

2nd Derivative Mean

2nd Derivative Variance

2nd Derivative Skewness

2nd Derivative Kurtosis

Mean Normalized by Variance

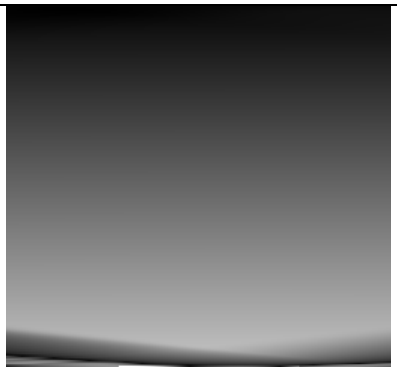

Mean Normalized by 1st Derivative Variance

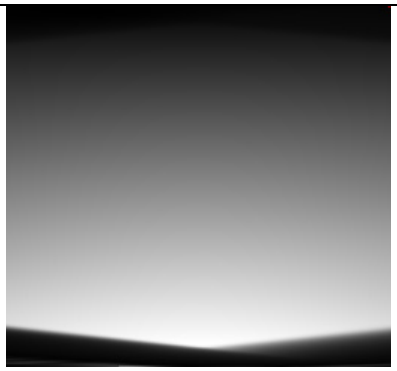

Mean Normalized by Variance Sum

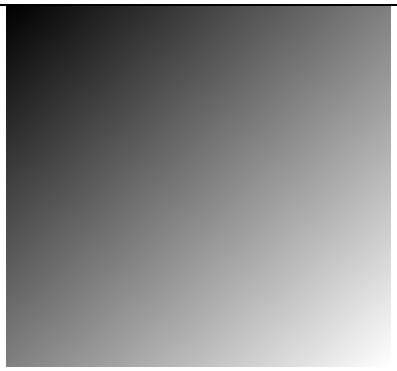

Original Index Map

As a general method, the use of descriptive statistics is a failure for the two-dimensional gradient. While it is capable of detecting the x-component of the gradient it fails completely to show the presence of a gradient along the optical axis. This is expected given the ill-conditioning of this specimen. There are artifacts visible on the bottom edges of the statistical moment maps; this is due to the approximation of index of refraction outside the sample as being constant.

C.5 Triple Normal (Gaussian) Distribution

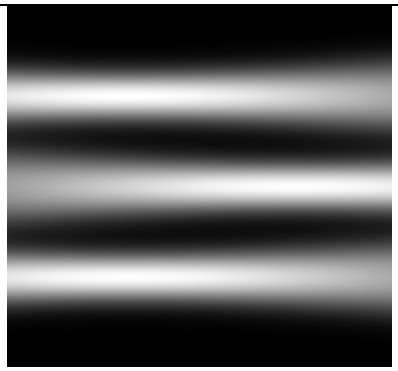
Mean

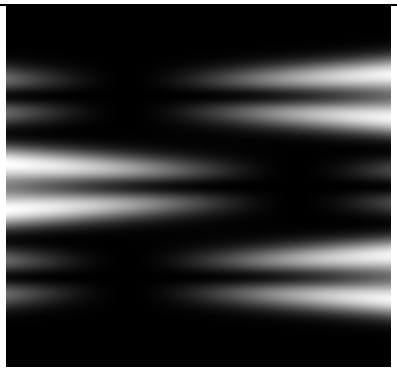
Variance

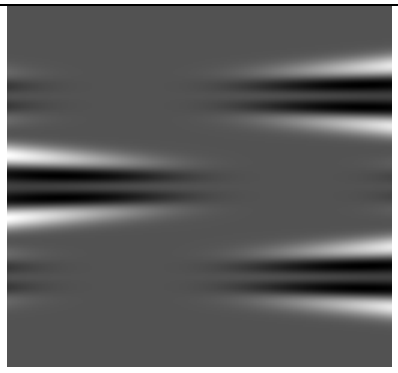
Skewness

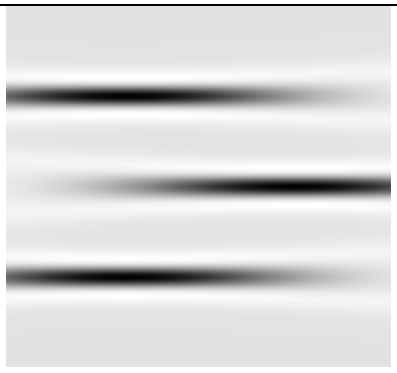
Kurtosis

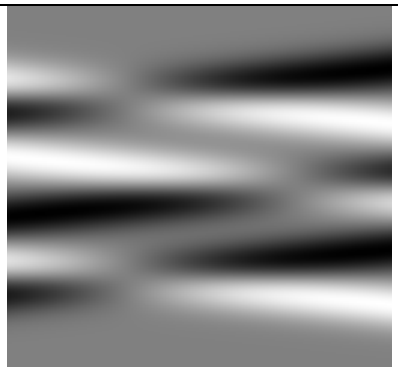
1st Derivative Mean

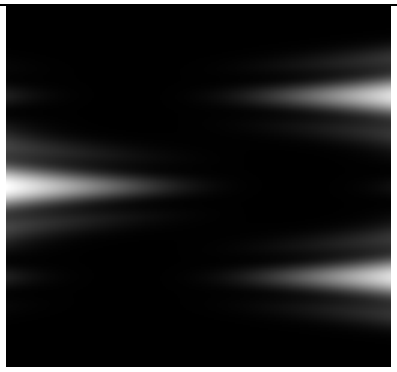
1st Derivative Variance

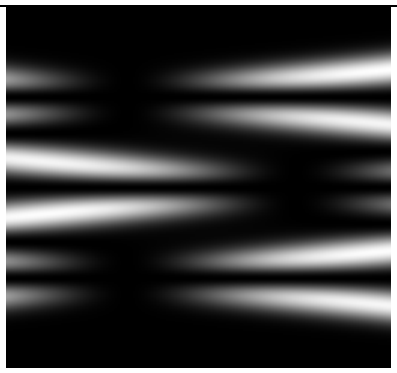

1st Derivative Skewness

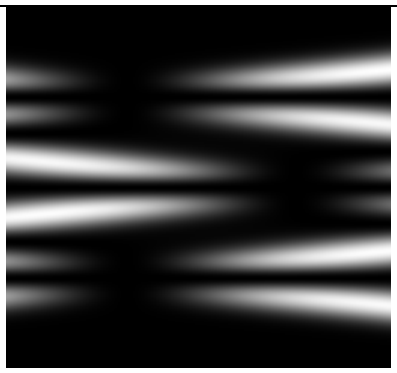

1st Derivative Kurtosis

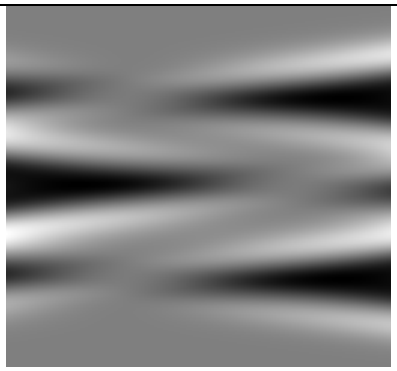

2nd Derivative Mean

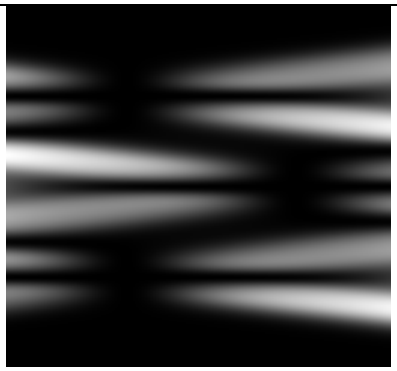

2nd Derivative Variance

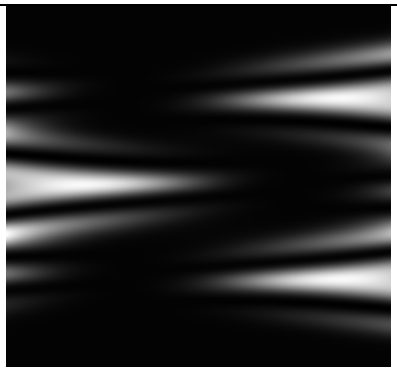

2nd Derivative Skewness

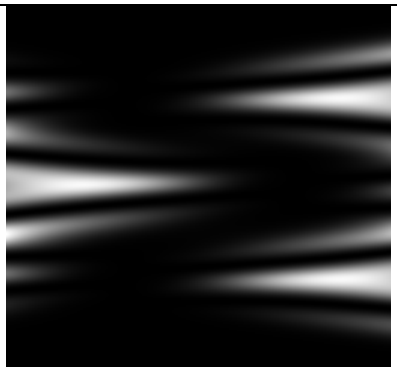

2nd Derivative Kurtosis

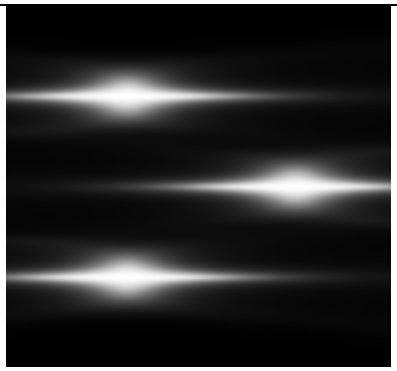

Mean Normalized by Variance

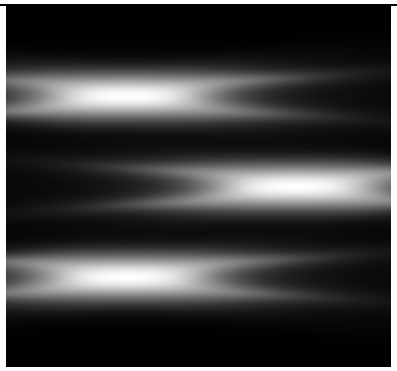

Mean Normalized by 1st Derivative Variance

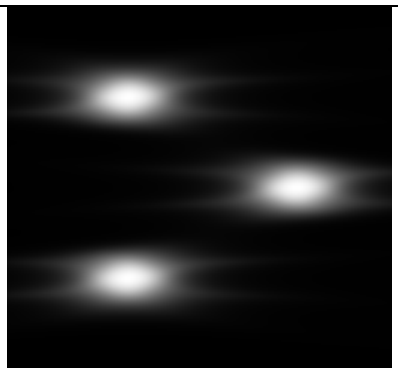

Mean Normalized by Variance Sum

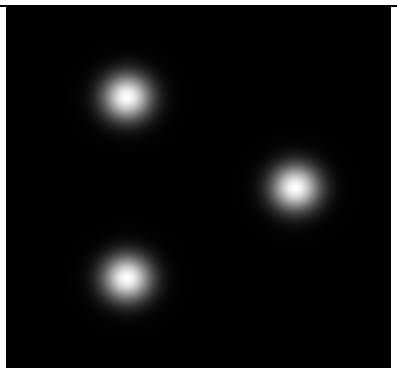

Original Index Map

The triple Gaussian was designed as a test to see if there would be any significant interference between widely spaced normal distributions. It does not appear to have a significant impact but there is clearly some influence on the 1st derivative skewness and kurtosis that was not present in the single normal distribution.